Vat photopolymerization additive manufacturing of functional materials: from batteries to metals and alloys

Thesis by
Max A. Saccone

In Partial Fulfillment of the Requirements for the
Degree of
Doctor of Philosophy

CALIFORNIA INSTITUTE OF TECHNOLOGY
Pasadena, California

2022
Defended June 1, 2022

Max A. Saccone
ORCID: 0000-0003-3846-2908

Dedicated to the memories of my grandparents,
who started it all, with unconditional love:
Elaine Dickstein, Bob Dickstein, Doris Saccone, and Cy Saccone.

ACKNOWLEDGEMENTS

In the sunset of dissolution,
everything is illuminated...

Milan Kundera, *The Unbearable Lightness of Being*

First, I would like to thank my energetic and insightful advisor, Professor Julia R. Greer, for her guidance and support throughout my PhD studies. Thank you for trusting me to be independent, for encouraging me to dream big, and for caring about me as a scientist and as a person. In ways I couldn't have imagined when I arrived at Caltech, I've grown as a problem solver, a storyteller, and a communicator thanks to the example you set.

Thank you also to my committee members for your insight and support: Prof. Karthish Manthiram, Prof. Kim See, and Prof. Julie Kornfield. Kim, thank you for welcoming me into your lab and journal clubs as a young grad student, where I learned to consume and critique science. Karthish, thank you for helping me think through the next steps in my scientific journey, and for being a role model for how kindness and positivity can flourish in academia. Julie, thank you for your attention to detail, scientific rigor, and constructive feedback.

The Greer group has been an amazing and inspiring group of scientists to share this journey with. I have been constantly amazed by this group's extraordinary curiosity, resilience, and kindness. Thanks to those that inspired me early on: Prof. Daryl Yee, Dr. Andrey Vyatskikh, Dr. Xiaoxing Xia, Prof. Carlos Portela, and Prof. Ottman Tertuliano. Daryl, I am in awe of your enthusiasm for science, your curiosity, and the care you show for those around you. I'm honored to call you a mentor, a collaborator, and a friend. Andrey, Xiaoxing, Carlos, and Ottman, thanks for being role models during my early days in the group. Thanks also to the members of battery subgroup: Dylan Tozier, Mike Citrin, Kai Narita, Fernando Villafuerte, and Yuchun Sun, and members of the metal microlattice sub-subgroup: Rebecca Gallivan, Thomas Tran, and Wenxin Zhang. To my cohort in the Greer group: Amy, Fernando, Rebecca, and Widi, it's been a pleasure to share this journey from uncertainty and fear to uncertainty and excitement with you. Finally, thank you to the undergrads I've had the privelege to mentor through senior theses: Becca Mikovsky and Chan Gi Kim.

I am grateful to the Resnick Sustainability Institute for their fellowship support and for focusing on bringing people together to tackle one of the world's most existential threats. To the people who comprise this Institute: Neil Fromer, Stephanie Yanchinski, and Prof. Jonas Peters, thank you for your commitment to the task at hand. I'm also grateful to other Caltech staff who made my life better in big and small ways: Allison Kinard, Angie Riley, Christy Jenstad, Jennifer Blankenship, Carolina Oseguera, Tess Legapsi, the Caltech facilities staff, Dr. Chi Ma, Dr. Michael Takase, and countless others.

Thank you to the people I've had the pleasure of sharing living spaces with: Andy Ylitalo, Widi Moestopo, Chelsea Edwards, Harsha Narravula, Sylvain Collet, Elliott Mueller, and Matt Levine. You've all made the places I've lived in feel like homes these last five years.

Thank you to friends from the Caltech Alpine Club, trail running Breakfast Club, and the Los Feliz Flyers for your enthusiasm and stoke for the outdoors. Mike O'Connell, Shae Silverman, Aadrian Schiphorst, Michael Marshall, Andy Boyle, Noel Csomay-Shanklin, Dave Bonan, Andreas Butler, Rob Webber, Aubrey Schonhoff, Ryoto Sekine, Ellen Kenney, Mikey Kerkman, Blake Owens, and many others.

Thank you to the long-time friends who have supported me through the years and across the miles: Alex Graff, Peter Satterthwaite, and Isaac Green. And thank you to my partner, Mary Fischer, for your unyielding positivity and kindness.

Most of all, thank you to my incredible family. Grandma E, thank you for encouraging my intellectual development, for taking pride in everything I do, and for always believing in me. Grandma Dor, thank you for your humble practicality and for instilling a sense of finding wonder and beauty in the plants and animals of everyday life. Moreover, thank you to both of you for your vision for and dedication to our family. Truly, I owe everything to the strength and love with which you imbued our family.

Thank you to my parents, Susan Dickstein and Tony Saccone. Mom, I never really knew what you were doing when you were 'writing grants and papers' when I was a child. Now I really know and am incredibly impressed by your ability to do research, to care for others, and to care for our family, all at the highest level. Dad, thank you for valuing hard work, ethics, and entrepreneurship while always putting people first.

Finally, thank you to my brothers, Alex Saccone and Ben Saccone. Ben, you continually impress me with your idealism, artistry, and enthusiasm. Alex, you are a role model for kindness, hard work, and integrity. Who I am today is inseparable from who you both are, and I love you very much.

ABSTRACT

In recent years, additive manufacturing (AM), also known as 3D printing, has emerged as a uniquely powerful tool for rapid prototyping and for creating complex, high value structures. Vat polymerization (VP) is an AM technique which forms parts through light-initiated polymerization, capable of achieving both high resolution and high throughput. While VP has been utilized to fabricate a wide variety of polymeric materials, fabricating functional materials such as ceramics, metals, and inorganic composites has remained a challenge. This thesis focuses on developing fabrication methods for a range of functional materials, from battery active materials to metals and ceramics, via vat polymerization additive manufacturing, taking advantage of chemical reactions within an AM part after fabrication to form target materials in situ.

We demonstrate the use of emulsions to introduce aqueous active material precursors into organic photopolymer resins to create architected lithium sulfide/carbon composites for use as lithium-sulfur battery cathodes. Such architected cathode materials are promising for mitigating mechanical degradation in high volume-change battery materials such as the sulfur cathode. We additionally performed nanomechanical experiments on lithium sulfide powders to determine how lithium sulfide yields, deforms, and fails in the context of volume-change-induced stress during battery cycling. Because lithium sulfide is present as a discharge product in all lithium sulfur batteries, these nanomechanical particle compressions have bearing on the entire field, beyond the realm of 3D architected cathodes.

We additionally demonstrate the use of organogel templates to streamline the AM process by enabling the fabrication of many materials starting with a single resin composition, followed by infiltration of appropriate metal precursors and post-processing heat treatment to convert the polymer/precursor matrix to the target metal via calcination and reduction reactions. We fabricate and characterize copper, nickel, silver, cobalt, cupronickel alloys, tungsten, and more to highlight the wide-ranging versatility of achievable materials and microstructures.

PUBLISHED CONTENT AND CONTRIBUTIONS

Chapter 1 has been adapted from:

1. Narita, K.[*]; Saccone, M. A.[*†]; Sun, Y.; Greer, J. R. Additive manufacturing of 3D batteries: A perspective. *Journal of Materials Research* **2022**, DOI: 10.1557/s43578-022-00562-w.
   Contributions: M.A.S. helped conceive the paper structure and wrote the manuscript.

Chapter 2 has been adapted from:

2. Saccone, M. A.[†]; Greer, J. R. Understanding and mitigating mechanical degradation in lithium–sulfur batteries: Additive manufacturing of Li_2S composites and nanomechanical particle compressions. *Journal of Materials Research* **2021**, 36, 3656–3666, DOI: 10.1557/s43578-021-00182-w.
   Contributions: M.A.S. conceived, designed, and performed the experiments, and wrote the manuscript.

Chapters 3 and 4 have been adapted from:

3. Saccone, M. A.[*†]; Gallivan, R. A.[*]; Narita, K.; Yee, D. W.[†]; Greer, J. R.[†] Microscale fabrication of 3D multicomponent metals via hydrogel infusion. *In review* **2022**. Preprint DOI: 10.21203/rs.3.rs-1108933/v1.
   Contributions: M.A.S. conceived and designed the experiments, designed photoresins, fabricated samples, performed material characterization, wrote the manuscript, and is a corresponding author.

Not directly adapted in this thesis:

4. Yee, D. W.[†]; Citrin, M. A.; Taylor, Z. W.; Saccone, M. A.; Tovmasyan, V. L.; Greer, J. R. Hydrogel-based additive manufacturing of lithium cobalt oxide. *Advanced Materials Technologies* **2021**, 6, 2000791, DOI: 10.1002/admt.202000791.
   Contributions: M.A.S. assembled coin cells and performed electrochemical experiments.

[*]equal contribution
[†]corresponding author

TABLE OF CONTENTS

LIST OF FIGURES

LIST OF TABLES

ABBREVIATIONS

AM Additive manufacturing

BD Beam diameter

BJ Binder jetting

CAD Computer aided design

DED Directed energy deposition

DIW Direct ink writing

DLP Digital light processing

DMD Digital micromirror device

DSC Differential scanning calorimetry

EDS Energy-dispersive X-ray spectroscopy

FDM Fused deposition modeling

FIB Focused ion beam

HEA High entropy alloy

HIAM Hydrogel infusion additive manufacturing

IR Infrared

LCD Liquid crystal display

LED Light emitting diode

MJ Material jetting

PBF Powder bed fusion

PμSL Projection micro-stereolithography

SEM Scanning electron microscope

SLA Stereolithography

TEM Transmission electron microscopy

TGA Thermogravimetric analysis

TPL Two-photon lithography

UV Ultraviolet

VP Vat photopolymerization

XRD X-ray diffraction

Chapter 1

INTRODUCTION

1.1 Materials and society

Creating physical objects is a fundamental human endeavor. From tools, to toys, to sculptures, acts of creation allow us to shape our surroundings, to improve our quality of life, and to find meaning. Throughout history, the common materials that people have used to build have been used as a proxy for technological development; we have named entire eras after commonly used materials, from the stone age to the bronze age to the iron age, and beyond.

Today, we find ourselves on the dizzying crest of rapid technological development. While the epochalism that led to the definition of the 'ages' cannot fully understand the complexity of human development and history, especially across diverse geographical regions[1], it can give us a sense of the rapidity of progress in materials development; generally, the stone age lasted for many thousands of years, while the bronze age lasted only a few thousand, and the iron age a fleeting few hundreds of years [1]. The distinction of clear ages has begun to break down, with several world-changing discoveries occurring within the last century: nuclear materials and the discovery and development of quantum physics [2], the discovery of polymers [3], and the development of classical computing *in silico* [4].

What will be the next defining material discoveries to shape the world? The nascent technologies of renewable energy, quantum computing, and atomically precise manufacturing promise to fundamentally change the way we power our lives, solve problems, and build things. However, we face unprecedented and existential challenges; globalization forces us to seek ways to co-exist peacefully with each other, to share and distribute resources, yet inequality looms and grows larger than ever before. Anthropogenic climate change co-evolved with human technological advances, many of which have increased our quality of life. Now, we need to learn how to live in harmony with the earth and take a more holistic and sustainable approach to industrial processes. With more tools and materials than ever before at our disposal, we need to not just focus on progress, but *sustainable* progress.

[1] I refer the reader to the front matter of Rolf Hummel's *Understanding Materials Science [1]* for a more nuanced timeline of materials development throughout the world.

1.2 Additive manufacturing

A recent advance in our ability to engineer materials is the process of additive manufacturing (AM), also known as 3D printing, which allows us to fabricate intricate computer-designed objects one layer at a time. 3D models, made via computer aided design or advanced structure algorithms are sliced into layers, which are then deposited sequentially. This process allows customized parts to be rapidly fabricated on often inexpensive equipment.

Unlike subtractive methods, which define part shape by removing material from an initially monolithic form, or formative methods, which define part shape through injection into a reusable cavity, AM is well-suited to producing materials with complex geometries or for rapid prototyping. Often, AM enables fabrication of complex objects more quickly and with less waste, or with fewer parts, without the need for fasteners [5].

Another advantage of additive manufacturing is the ability to make custom parts on demand. For example, in 2020 I lost a black pawn from my chess set, and replaced it with an additively manufactured replica. I created a computer-aided design (CAD) structure in SolidWorks based on the design of the chess set, and then printed the piece on our lab's Autodesk Ember printer (thanks, Julia!) using CPS PR57 resin. The resulting piece (Figure 1.1) is currently in use, and made my chess set whole.

Figure 1.1: **Additively manufactured pawn.** I designed a pawn (left) to match the style of my chess set (right), and printed it using PR57 black resin.

1.2.1 AM techniques overview

An overview of common classes of AM techniques is given here, largely following the nomenclature outlined by Ligon et al.[2][6], with citations to review articles that discuss each technique in more detail. An in-depth discussion of vat photopolymerization, the focus of this thesis, follows in Section 1.3.

- **Material extrusion** extrudes material from a nozzle to define part shape (Figure 1.2a,b). Common techniques include fused deposition modeling (FDM) [7], which uses heat to soften thermoplastic polymers during extrusion, and direct ink writing (DIW) [8], which uses shear thinning inks.
- **Material jetting (MJ)** expels droplets of material from a nozzle to define part shape (Figure 1.2c) [9].
- **Binder jetting (BJ)** defines part shape by the applying a liquid binder to fuse a powder precursor of the target material (Figure 1.2c) [10].
- **Vat photopolymerization (VP)** selectively solidifies a liquid photoresin via light-initiated polymerization to define part shape (Figure 1.2d) [11].
- **Powder bed fusion (PBF)** defines part shape by thermally driven melting or sintering of a powder precursor of the target material (Figure 1.2e). PBF is an established method to form many types of materials, from polymers [12] to metals [13].
- **Directed energy deposition (DED)** produces 3D parts through simultaneous material deposition through a blown-powder feedstock and localized heating (Figure 1.2f) [14].

1.3 Vat photopolymerization

1.3.1 History of vat photopolymerization

In 1981, Hideo Kodama reported the development of systems for forming 3D polymeric parts using a liquid photocurable resin [15]. Kodama demonstrated that 2D images of light could be projected to cure an entire layer of photoresin simultaneously (Figure 1.3a,b), or alternatively a laser or point light source could be raster scanned over the photoresin vat to form a layer (Figure 1.3c). These techniques are

[2] I refer the interested reader to this excellent and thorough review of polymer AM techniques.

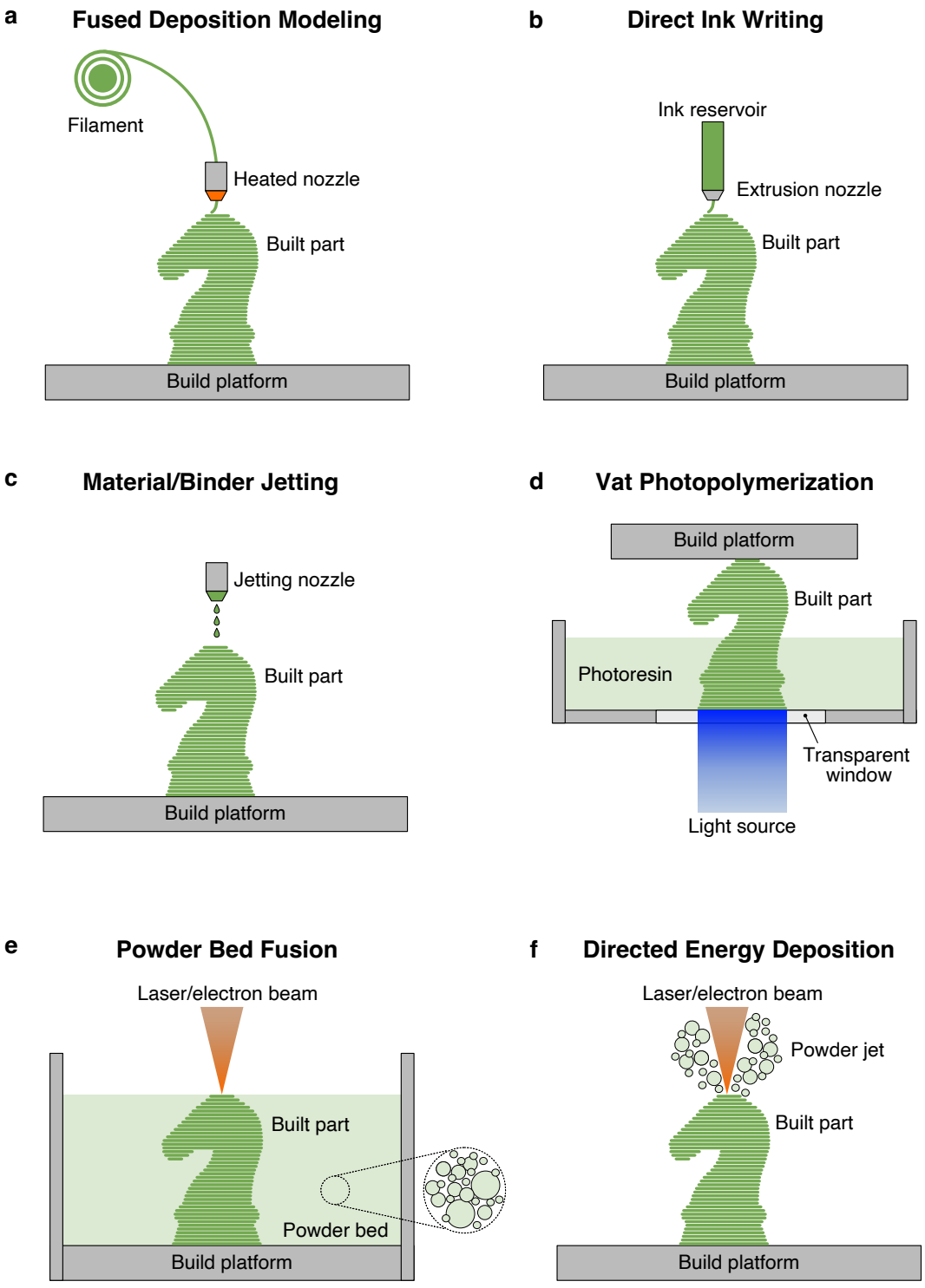

Figure 1.2: **Schematics of common additive manufacturing methods. a,** Fused deposition modeling, **b,** direct ink writing, **c,** material/binder jetting, **d,** vat photopolymerization (DLP pictured), **e,** powder bed fusion, and **f,** directed energy deposition. In all AM methods, supports (not pictured) may be needed to achieve certain geometries such as overhangs.

now known as digital light processing (DLP), and stereolithography (SLA) respectively, although the term stereolithography sometimes subsumes other definitions and is used to refer to a broader range of VP techniques.

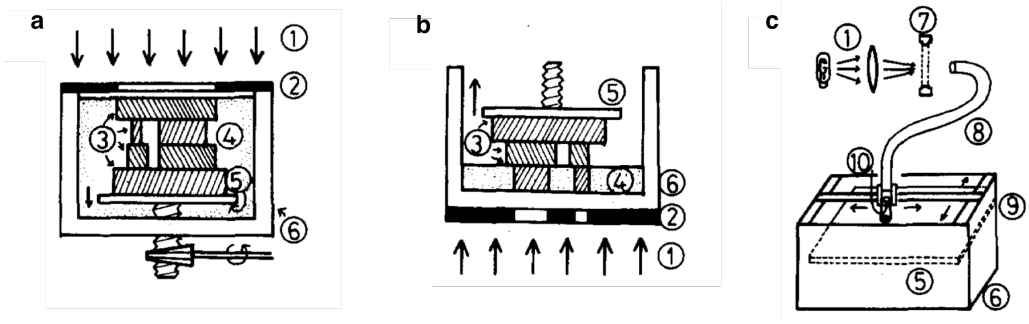

Figure 1.3: **Schematic of Kodama's stereolithography apparatuses.** Photopatterning is controlled by **a,** a mask with light projected from the top, **b,** a mask with light projected from the bottom, or **c,** a scanning fiber transmitter mounted on an XY plotter. Following the numbering from the figure: ① UV light, ② mask, ③ solidified polymer layers, ④ liquid photoresin, ⑤ build plate, ⑥ vat, ⑦ shutter, ⑧ optical fiber, ⑨ XY plotter, ⑩ optical lens. Adapted with permission from [15]. Copyright 1981 American Institute of Physics.

While Kodama's innovation represents the first iteration of what is presently called stereolithography, this verbiage was not defined until Charles Hull coined the term stereolithography in a 1984 patent application[3] for an "apparatus for production of three-dimensional objects by stereolithography" (Figure 1.4) [16]. Hull's patent was significant, as it underpinned the founding of the first commercial AM company, 3D Systems [17].

Since then, the field of vat photopolymerization has broadened into a vibrant academic field, with a rapidly increasing number of publications since the development of the technology, and especially since about 2015 (Figure 1.5). This marked increase in academic activity is likely due to the increased availability of commercial, low-cost SLA systems.

1.3.2 Vat photopolymerization methods

Vat photopolymerization represents a varied class of technques that use light to define part shape through polymerization of a photoresin bath. The three main modes of carrying out vat photopolymerization (Figure 1.6) are further categorized by 1) the type of photoinitiator, which can respond to single photon (often UV) absorption, or two/multi-photon (often IR) absorption and 2) the geometry/topology of the light/resin interaction volume.

[3] Assigned to UVP, Inc. in San Gabriel, CA.

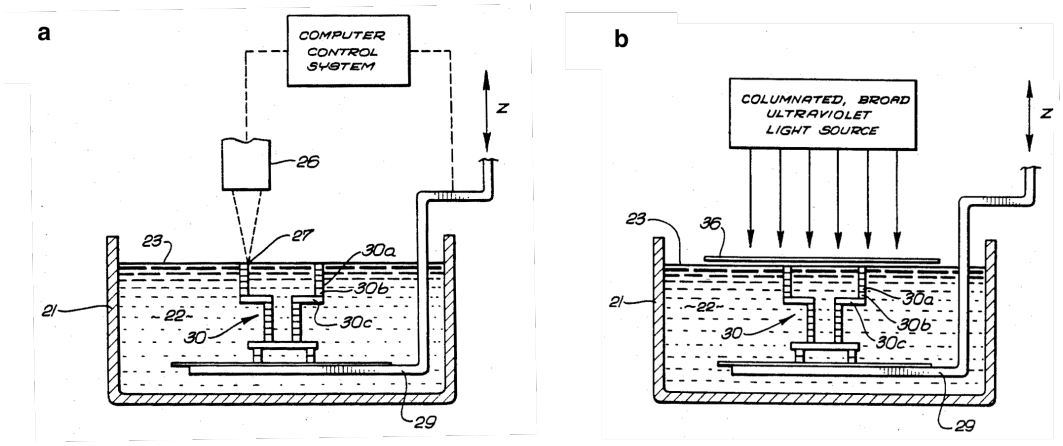

Figure 1.4: **Schematic of Hull's 1984 stereolithography patent.** Photopatterning is controlled by **a**, a raster scanned spot source or **b**, a masked collimated light source. Following the numbering in the figure: 21, resin container; 22, UV-curable liquid resin; 23, surface of the liquid resin; 26, programmable source of UV light; 27, spot source of UV light; 29, elevator platform; 30, printed three dimensional object composed of layers such as 30a/b/c; 36, mask for collimated UV source. Adapted from reference [16].

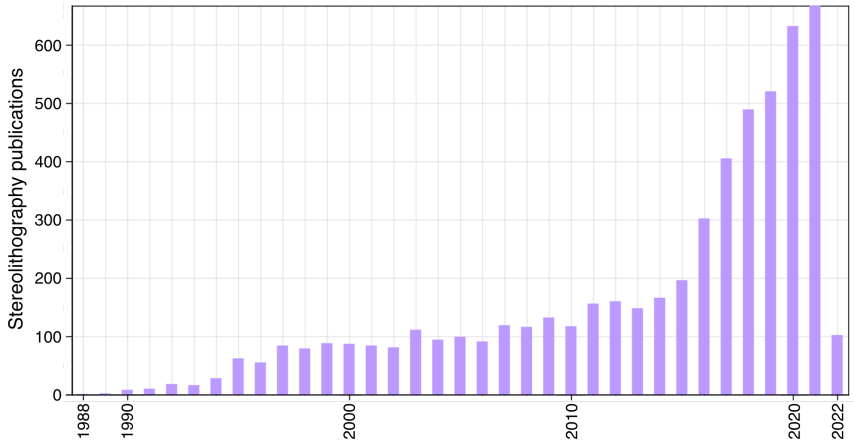

Figure 1.5: **Stereolithography publication report.** Publications on the topic of "stereolithography" since 1988. Retrieved from Clarivate Web of Science Citation Report on 3/17/2022.

Common techniques that rely on one-photon absorption to initiate cross-linking include digital light processing (DLP), in which a ultraviolet (UV) light source is used to project a 2-dimensional image into the photoresin vat, curing an entire layer simultaneously (Figure 1.6a), and stereolithography (SLA), in which a UV laser is raster scanned across the photoresin (Figure 1.6b). In contrast, two-photon lithography (TPL) techniques rely on the simultaneous absorption of two or more photons from a raster scanned infrared (IR) laser to initiate and localize cross-linking in a spatially confined volumetric pixel, or 'voxel,' (Figure 1.6c) which enables higher resolution patterning than systems which rely on single-photon absorbtion to initiate polymerization.

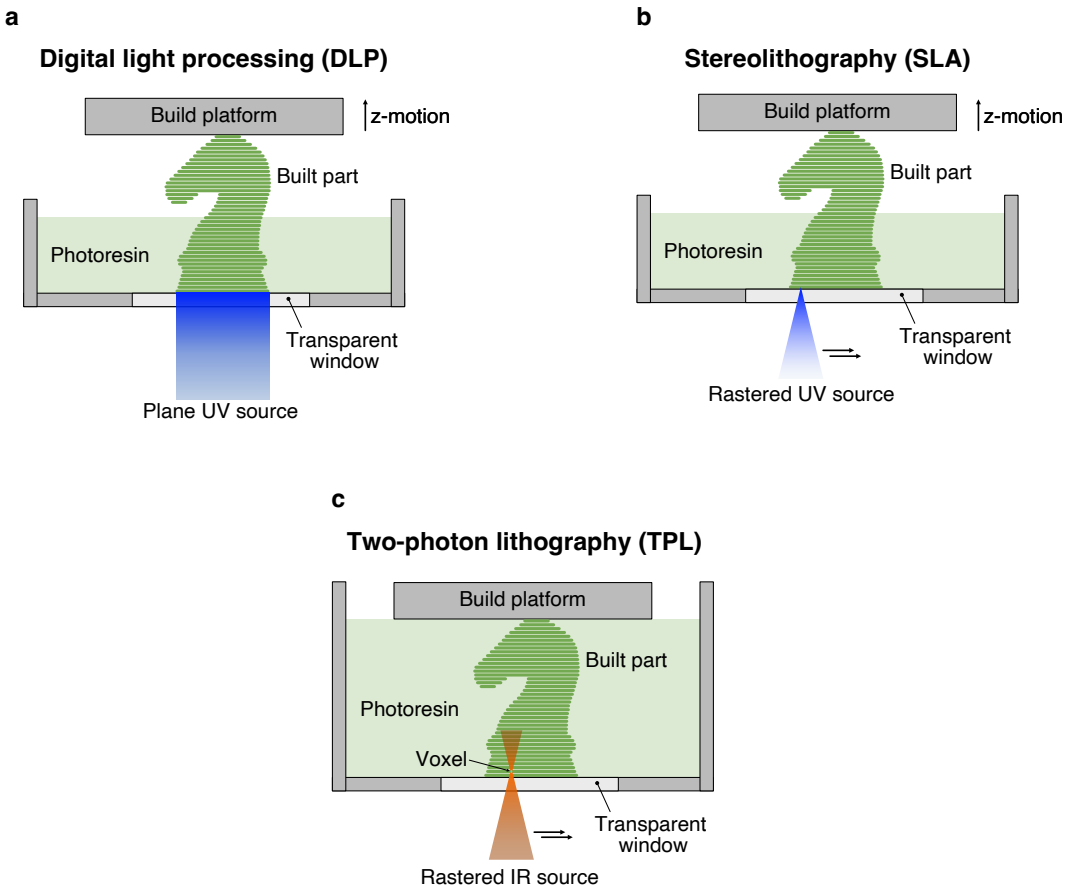

Figure 1.6: **Schematic of VP techniques.** Vat photopolymerization techniques including **a,** digital light processing, **b,** stereolithography, and **c,** two-photon lithography.

1.3.2.1 Digital light processing (DLP)

Digital light processing is a class of techniques, also known as mask projection, in which 2D patterns of light are used to cure the desired areas of entire layers of resin simultaneously [17]. In practice, this is achieved either by using a liquid crystal display (LCD) screen to act as a photomask for a light emitting diode (LED) light source, a technique colloquially termed LCD printing, or by using a digital micromirror device, where the movement of individual mirrors (pixels) controls the delivery of light from a UV lamp to the resin bath.

In 2005, Sun et al. reported the use of such a digital micromirror device (DMD, Texas Instruments) to control the patterning of light in digital light processing in a technique coined projection micro-stereolithography (PμSL)[4] [18]. This method, in which a digital micromirror device was used to control the delivery of patterned

[4]Dr. Nick Fang, a co-author on this paper, went on to found the company Boston Micro Fabrication, Inc. to commercialize PμSL technology.

light to a photoresin (Figure 1.7), enabled a high modulation efficiency of almost 90%, smaller pixel sizes of ~ 15 µm, and a faster switching rate of 20 µs compared to previously used LCD technology.

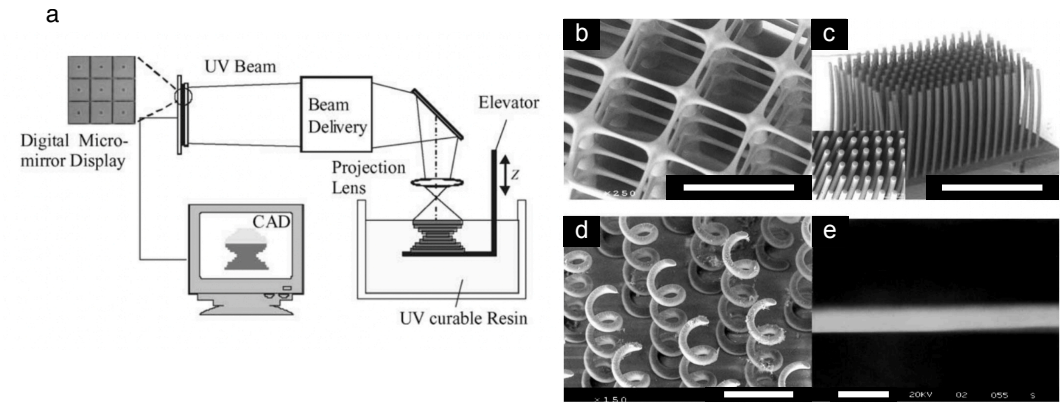

Figure 1.7: **Projection microstereolithography (PµSL). a,** Schematic of PµSL system, showing light patterning via a digital micromirror device. PµSL enables the fabrication of complex, high resolution structures such as **b,** suspended beams with 5 µm diameter, **c,** high aspect ratio micro-rods, **d,** coils with filament diameter of 25 µm, and **e,** suspended line with 600 nm diameter. Scale bars: **b,** 200 µm; **c,** 1mm; **d,** 200 µm; **e,** 1 µm. Adapted with permission from reference [18]. Copyright Elsevier Science & Technology Journals.

DLP technology has since been advanced to reach both higher resolution and higher throughput. In 2015, DeSimone and coworkers reported continuous liquid interface production (CLIP) of 3D objects, in which the traditional layer-by-layer approach of DLP technology was replaced with a continuous approach, allowing parts to be fabricated at a rate of tens of centimeters per hour [19]. CLIP printers project UV light into the resin bath through an oxygen-permeable window to create an oxygen-rich interface region in which polymerization is inhibited by the low reactivity of peroxy radicals. This approach enabled higher print speeds by obviating the need to re-coat resin in between layers and for complex layer separation movements. Later, in 2019, Mirkin and coworkers reported a technique for high-area rapid printing (HARP) that mitigated problems associated with exothermic polymerization reactions leading to heat build-up at the printing interface [20]. The HARP approach used a flowing bed of fluorinated oil instead of an oxygen-permeable window to minimize interfacial adhesion and to aid with heat transport away from the printing interface, and enabled volumetric throughputs of 100 L/hr, or ~40 cm/hr.

In principle, DLP AM techniques are scalable, and the critical factor determining print speed is the linear rate of printing of an object in the z-direction (perpendicular to the plane of light exposure). With additional DMD projectors, the area of light irradiation can be increased arbitrarily, while the volumetric throughput is directly

proportional to both the area of irradiation and the linear z-direction print rate. Many companies (such as Carbon 3D, Inc. and Azul 3D, Inc., based on the technologies described above) have developed around the promise of commercialization of such high-throughput DLP printing.

1.3.2.2 Volumetric additive manufacturing

As we have seen in previously discussed VP AM techniques, light can be introduced as a 1D point source, and rastered to form a layer (SLA), or introduced as a 2D plane source (LCD or DLP) to form a layer in one exposure. A natural next step in light-based AM is to consider 3D exposure to form entire 3D parts simultaneously. The concept of interference lithography has been established as a way to create 3-dimensionally periodic structures from a single exposure, based on a 3D light intensity distribution resulting from interference of coherent laser beams [21]. However, interference lithography is only able to create periodic structures, and not arbitrarily designed 3D structures.

In recent years, volumetric additive manufacturing has emerged as a powerful tool to create 3D objects in a single exposure [22–24]. The principle behind volumetric additive manufacturing, and some examples of objects fabricated via volumetric AM, including polymers and transparent silica ceramics, are shown in Figure 1.8. Increasing the dimensionality of the light-patterning has inherent advantages for print speed. These seminal works demonstrated the fabrication of 3D designed cm-scale objects in tens of seconds, and also enable the use of viscous resins, since it is advantageous to have minimal resin movement during the printing process. Another interesting feature of volumetric additive manufacturing is its ability to overprint 3D structures around existing features formed from a different material.

1.3.3 Vat photopolymerization chemistry

Photoinitiation for vat photopolymerization is classified according to a taxonomy attributed to Norrish, who along with Bamford, reported the photo-decomposition of aldehydes and ketones [25] in 1937. Norrish Type I initiators are molecules, which decompose into radical fragments under illumination from appropriately energetic photons. This reaction is shown for Darocur 1173 in Figure 1.9a. Other common Type I initiators, such as Irgacure 184, Irgacure 651, Irgacure 369, diphenyl(2,4,6-trimethylbenzoyl)phosphine oxide (TPO), phenylbis(2,4,6-trimethylbenzoyl)phosphine oxide (BAPO), and Ivocerin are shown in Figure 1.9b. Phosphine oxide initiators

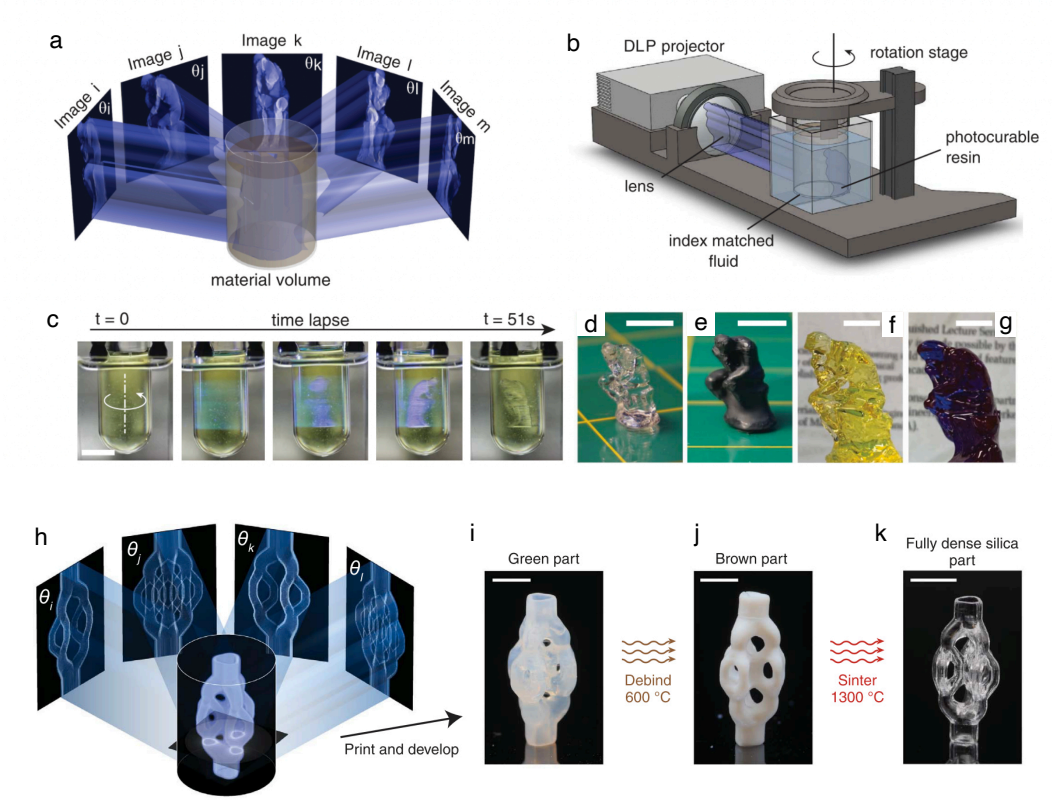

Figure 1.8: **Volumetric additive manufacturing. a,** Patterned light from many angles is projected to form a computer-designed dose intensity within a liquid photoresist using **b,** an setup making use of a DLP projector and a rotation stage. **c,** Time lapse of volumetric resin exposure showing curing of a part shown in **d,e,** as well as larger versions shown in **f,g**. This technique can also be adapted to form fully dense and transparent silica ceramics, shown in **h-k**. Panels **a-g** adapted with permission from reference [22]. Copyright 2019 American Association for the Advancement of Science. Panels **h-k** adapted with permission from reference [24]. Copyright 2022 American Association for the Advancement of Science.

such as TPO and BAPO are commonly used in commercial stereolithography and digital light processing resins (such as PR48, see Table A.1) because they tend to absorb well in the near-UV range.

In contrast to Type I initiators, Norrish Type II initiators rely on a system composed of two molecules: a sensitizer, and a co-initiator. After excitation by appropriately energetic light, the sensitizer abstracts a hydrogen atom from the co-initiator, which becomes a radical initiator. This process is shown in Figure 1.10, in which benzophenone acts as the sensitizer and a tertiary amine acts as the co-initiator. An example of a Type II initiation pair is the sensitizer bis[4-(dimethylamino)phenyl]methanone (Michler's ketone) and the co-initiator 2-dimethylamino-2-(4-methyl-benzyl)-1-(4-morpholin-4-yl-phenyl)-butan-1-one (Irgacure 379).

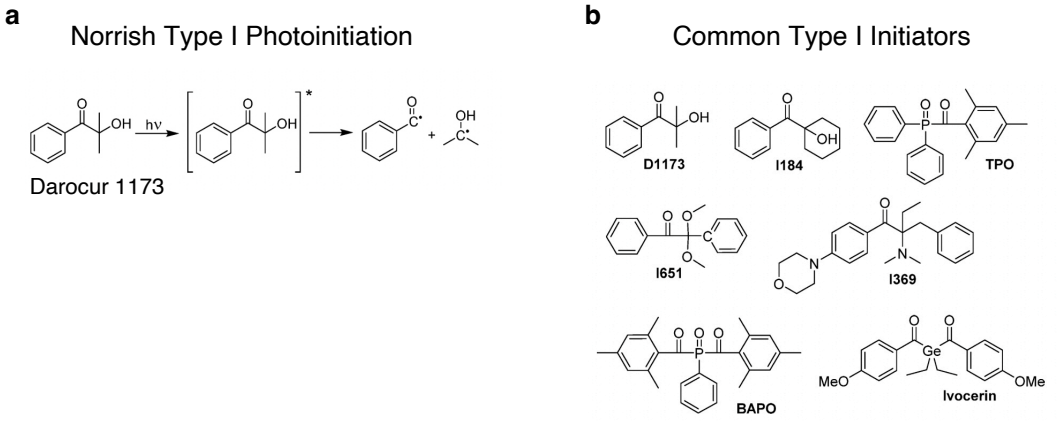

Figure 1.9: **Norrish Type I photoinitiation. a,** A typical reaction showing the photocleavage of the Norrish Type I photoinitiator Darocur 1173. **b,** Several other common Norrish Type I photoinitiators. Adapted from reference [6] under open-access CC-BY license.

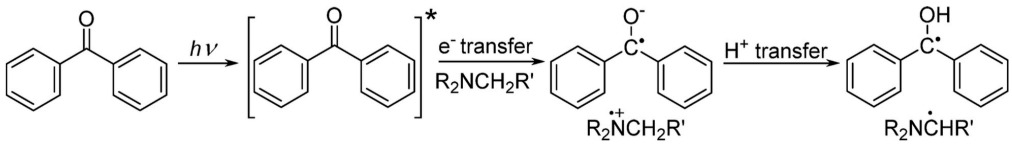

Figure 1.10: **Norrish Type II photoinitiation.** Benzophenone is the sensitizer, abstracting a hydrogen after excitation from the tertiary amine which acts as the co-initiator. Adapted from reference [6] under open-access CC-BY license.

1.3.4 Vat photopolymerization of functional materials

Although VP was developed predominantly for use with polymers [6], it has also been demonstrated for organogels [26], hydrogels [27], glasses [28] and ceramics [29, 30]. However, material selection is still limited due to challenges with resin stability, processability, and synthetic accessibility associated with incorporating the necessary precursors into photoresins either as a slurry [31, 32] or as an inorganic-organic mixture [33]. In particular, creating metals via VP has remained a challenge in the field. Oran et al. demonstrated AM of nanoscale silver by using hydrogels as "nanomanufacturing reactors" [34, 35] in which two-photon activation guides the infiltration of precursors to volumetrically deposit 3D materials, and Vyatskikh et al. demonstrated AM of nanoscale nickel by using two-photon lithography to pattern inorganic-organic resins containing nickel acrylates, followed by pyrolysis and reduction by H_2 [33]. However, these pioneering works are limited in scope for fabricating a wide variety of metals, requiring complex resin design and optimization, or tuning of conjugation chemistry for each new material.

1.4 Additive manufacturing of 3D batteries

Additive manufacturing (AM) enables the fabrication of battery materials with complex geometries. When battery components can take arbitrary form factors, opportunities emerge for creating electrode configurations with improved power density, reduced weight, and excellent mechanical stability. This section provides a summary of recent progress in AM of 3D batteries, discussing relevant techniques, materials, designs, and applications. We highlight advantages and limitations associated with battery electrodes fabricated by direct ink writing, fused deposition modeling, vat photopolymerization, and selective laser sintering. Additionally, we discuss optimal geometries and compatible materials for anode, cathode, and electrolyte of fully 3D batteries. To increase transparency and utility in the field, we suggest a standardized set of reporting metrics for 3D batteries. Finally, we identify key opportunities for implementation of 3D batteries due to critical advantages such as shape conformability and the ability to serve as multifunctional or structural components.

1.4.1 Overview of AM methods for 3D batteries

Many AM methods are used to create 3D battery electrodes. Of the available strategies, extrusion of battery active materials through motion-controlled nozzles is the most common. A variety of review articles focus on other methodologies such as material jetting, binder jetting, powder bed fusion, directed energy deposition, template-assisted deposition, and laminated object manufacturing [36–38]. Here, discussion is limited to the several most common 3D printing techniques for the fabrication of battery electrodes: direct ink writing, fused deposition modeling, vat photopolymerization, and selective laser sintering.

The basics of these methods were discussed in Section 1.2. Table 1.1 provides an overview and compares several examples of batteries fabricated using each method. Advantages, limitations, and opportunities for each technique are discussed in the following sections.

1.4.1.1 Direct ink writing for batteries

Direct ink writing (DIW) extrusion through motion-controlled nozzles is the most common strategy for 3D printing electrochemical devices. DIW allows the facile fabrication of many different materials by mixing active material particles with solvent and binders to form shear-thinning inks that can then be extruded at high shear, but then remain stable after extrusion. The organic solvents and binders are often removed in a post-processing thermal treatment. Extrusion methodologies have been used to 3D print electrodes consisting of $LiFePO_4$ and $Li_4Ti_5O_{12}$ as Li-ion electrodes [39, 40], sulfur composites as Li-S cathodes [45, 46, 60], holey graphene oxide as a Li-O_2 cathode, and $Na_3V_3(PO_4)_3$ composites for Na-ion electrodes [41]. The minimum feature size of extruded electrodes is related to the size of the nozzle through which the active material ink is extruded, but can be altered by postprocessing such as thermal treatment which can remove solvents, organics, or sinter inorganic materials. In optimized systems where polyelectrolyte inks are deposited into an alcohol and water reservoir, DIW with nozzles 0.5-1 μm in diameter has been shown to be able to fabricate beams as small as 600 nm in diameter with beam spacing approximately equal to the beam diameter [61]. Notably, these optimized polyelectrolyte inks did not contain any solid material loading and were optimized to minimize the viscosity of the ink when flowed through the smallest diameter nozzles. Despite not being directly relevant to battery materials, this work shows the potential for DIW to access small length scales.

DIW has many attractive characteristics for 3D printing electrodes such as low cost, experimental simplicity, and a wide range of available materials. However, challenges arise when active material particles are added to DIW inks. Adding battery active materials to a slurry tends to increase the viscosity of the ink, necessitating larger nozzles and commensurately larger feature sizes. For example, Sun et al. extruded LFP and LTO inks through a 30 μm nozzle, resulting in feature sizes of approximately 30 μm, with mass loadings of 57-60 wt.% [39]. However, many other DIW approaches for 3D printed electrodes with high solid mass loadings do not reach feature sizes below 150 μm. These innate limitations of DIW restrict the available feature sizes and emphasize the need to balance rheological properties of the DIW ink with electrochemical properties of the printed electrode [62]. Additionally, the types of 3D architectures achievable via DIW are limited, with most works reporting either woodpile geometries or '2.5D' architecture where each layer of the printed structure is the same, and therefore sits directly on top of the previous

Table 1.1: Summary of reported batteries fabricated using common 3D printing methods.

AM Method	Feature size[1]	Anode	Cathode	Electrolyte[2]	Capacity[3]	Ref.
DIW	22 µm	LTO	LFP	1M $LiClO_4$ in EC/DMC	1.5 mAh/cm^2 at 1C	[39]
	180 µm	LTO/GO	LFP/GO	PVDF-co-HFP/Al_2O_3	91 mAh/g at 50 mA/g	[40]
	200 µm	Na	NVP/GO	1M $NaClO_4$ in EC/PC + 5% FEC	1.26 mAh/cm^2 at C/5	[41]
	200 µm	Li	LMO	1M $LiPF_6$ in EC/DMC	3.5 mAh/cm^2 at C/10	[42]
	37 µm	Li	LFP	Not reported	82 mAh/g at 10C	[43]
	200 µm	Li	Sulfur copolymer/ graphene	1M LiTFSI in DMC/DOL + 1 wt% $LiNO_3$	812.8 mAh/g at 50 mA/g	[44]
	150 µm	Li	Sulfur/carbon	1M LiTFSI in DOL/DME + 1 wt% $LiNO_3$	1188 mAh/g at C/10	[45]
	150 µm	Li	Sulfur/graphene/ phenol formaldehyde	1M LiTFSI in DOL/DME + 1 wt% $LiNO_3$	953 mAh/g at C/10	[46]
	50 µm	LTO	LFP	1M LiTFSI in PC	133 mAh/g at 0.2 mA/cm^2	[47]
	350 µm	LiF-Li-Mg	LFP	1M $LiPF_6$ in EC/DMC/EMC + 1% VC	145.2 mAh/g at C/2	[48]
	150 µm	Li	Si	1M $LiPF_6$, solvent not reported	2990 mAh/g at 0.5 mA	[49]
FDM	200 µm	Li	LTO/PLA	1 M $LiPF_6$ in EC/DEC + 2% VC	80 mAh/g at 6 µA/cm^2	[50]
	200 µm	Li	LFP/PLA	1 M LiPF6 in EC/DEC + 2% VC	60 mAh/g at 9 µA/cm^2	[50]
	200 µm	Graphite/PLA	LFP/PLA	1 M $LiPF_6$ in EC/DEC	30 mAh/g at C/40	[51]
	200 µm	LTO/PLA/ graphite/ MWNT	LFP/PLA/ graphite/MWNT	PLA:PEO:LiTFSI	Not reported	[52]
	200 µm	LTO/graphene/ PLA	LMO/MWNT/PLA	1M $LiClO_4$ in PC/EMC	22.96 mAh/cm^{3}at 20 mA/g	[53]
	200 µm	Li	LCO	1 M $LiPF_6$ in EC/DMC	130 mAh/g at C/10	[54]
	200 µm	Li	LTO	1 M $LiPF_6$ in EC/DMC	170 mAh/g at C/2	[54]
VP	100 µm	Li	LCO	1 M $LiPF_6$ in EC/DEC	115 mAh/g at C/20	[30]
	50 µm	Li	Li_2S-C	1M LiTFSI in DOL/DME + 1 wt% $LiNO_3$	310.1 mAh/g_{Li_2S}at C/20	[55]
	28 µm	Li	Pyrolytic carbon	1 M $LiPF_6$ in EC/DEC	379 mAh/g at 2 mA/g	[56]
	200 µm	LTO/PEGDA	LFP/PEGDA	1M $LiClO_4$ in EC/PC + 20% PEGDA resin	0.001 mAh/cm^{2}at 2 µA	[57]
SLS	100 µm	Not reported	NCA	Not reported	17 mAh/g	[58]
	250 µm	Li	PP/LFP	1 M $LiPF_6$ in EC/DEC	35 mAh/g at C/80	[59]

Electrode materials: LTO = $Li_4Ti_5O_{12}$, LFP = $LiFePO_4$, LMO = $LiMn_2O_4$, NVP = $Na_3V_2(PO_4)_3$, GO = graphene oxide, CNT = carbon nanotube, MWNT = multi- walled carbon nanotube, NCA = $LiNi_{0.80}Co_{0.15}Al_{0.05}O2$, PP = polypropylene.
Electrolyte components: EC = ethylene carbonate, DMC = dimethyl carbonate, PVDF = poly(vinylidenefluoride), HFP = hexafluoropropylene, DOL = 1,3- dioxolane, DME = 1,2-dimethoxyethane, PLA = poly(lactic acid), DEC = diethyl carbonate, VC = vinylene carbonate, PC = propylene carbonate, FEC = fluoroethylene carbonate, PEO = poly(ethylene oxide), EMC = ethyl methyl carbonate, PEGDA = poly(ethylene glycol) diacrylate.
[1]Feature size for FDM and SLS techniques is the reported layer thickness. Note that the lateral feature size may be much larger.
[2]Electrolyte mixtures are 1:1 (v:v) and additions are wt % unless otherwise noted.
[3]Gravimetric discharge capacities for the first cycle normalized by active material mass are reported, where available. Full cell capacity is reported, where available.

layer. Such structures fabricated via DIW are also usually limited in height, due to the structural limitations of stacking multiple layers, especially when inks do not solidify quickly or fully. This drawback can be partially mitigated by changing the printing environment to promote faster solidification of ink, e.g., by using a hot plate to evaporate solvent after printing [42], to aid with printing fidelity and structural integrity.

1.4.1.2 Fused deposition modeling for batteries

One very common approach for personal 3D printers is fused deposition modeling (FDM), a filament-extrusion 3D printing method. FDM processes use heat to soften a filament, often thermoplastic, before extruding it through a nozzle. The material then solidifies upon cooling after printing. For battery applications, composite filaments containing active materials such as graphite, LTO, and LFP have been developed with active material fractions up to 70% [50]. Practical use of FDM will require higher active material fractions while maintaining printability and mechanical integrity. Another drawback of FDM for electrochemical applications is the achievable resolution. Typically FDM can achieve layer thicknesses of 150 µm, but often suffers from comparatively poorer lateral resolution. In-depth overview and discussions of FDM for battery applications are found elsewhere [59].

1.4.1.3 Selective laser sintering for batteries

Selective laser sintering (SLS) is another emerging AM method for battery applications. SLS selectively scans a high-energy laser on powder beds to sinter powdered materials to create 3D structures in a layer-by-layer manner. This process does not typically require binders or solvents, enabling high fractions of active materials in the printed parts and less post-processing time to remove binders or solvents, compared with slurry-based 3D printing, including DIW. SLS has been used for metals and alloys for structural materials and recently is applied for energy storage materials. Acord et al. have consolidated lithium nickel cobalt aluminum oxide (NCA) cathodes by SLS with the electrochemically active layered structure retained, and explored processing parameters to mitigate crack formation and discontinuity caused by heterogeneous thermal volume change during printing [58]. Sha et al. have demonstrated 3D graphene foams by selectively pyrolyzing a mixture of nickel and sucrose by a CO_2 laser [63]. Significant challenges remain in the fabrication of 3D architected battery materials by SLS, including controlling defects such as

cracks and voids, as well as detrimental phases, which can form due to the high temperatures and the rapid heating rates inherent in SLS.

1.4.1.4 Vat photopolymerization for batteries

An attractive and underutilized alternative to DIW for fabrication of 3D battery electrodes is vat photopolymerization (VP) [64]. The main challenge with VP 3D printing of battery materials is the lack of available materials compatible with this technique [36–38]. VP offers a low cost, easily processable, and high resolution way to print battery materials, but requires photoresins with low viscosity to minimize suction pressure and adhesion [30]. When fabricating electrochemically active materials using VP, standard methodologies for introducing active materials or precursors into the resin include using slurries or suspensions of active materials dispersed in a photoresin, which increase the photoresin viscosity. Novel strategies to reduce the need for creating resin slurries include directly converting photoresin to an active material such as pyrolytic carbon [56] and using homogenous aqueous photoresins in which active material precursors are dissolved, which has been used to fabricate 3D LCO cathodes [65]. Alternatively, heterogeneous emulsion resins where active materials/precursors exist as an aqueous phase dispersed in a photoresin can be used to create 3D composite Li_2S-C structures (see Chapter 2) [55]. Thermal post-processing such as pyrolysis in an inert atmosphere or calcination in a low-pressure air atmosphere converts solidified photoresins to active materials and enables fully densified active material structure with small feature size (~30 μm). Other VP approaches include depositing battery active materials onto 3D printed polymer substrates [66].

A significant advantage of these VP methods is that fabricated electrodes can have smaller feature sizes and more complex geometries than those fabricated via other methods. This has potential to reduce diffusion lengths both in the electrode and electrolyte. However, challenges relating to battery assembly and incorporation with electrolyte and counter electrodes arise as electrodes become smaller and more geometrically complex. Additionally, VP has some of the most stringent material requirements on resin design of all the AM techniques discussed. The photoresin also contains photoactive molecules such as photoinitiators which generate radicals under exposure to UV light, and UV blockers to prevent UV light from being transmitted beyond the build layer during printing. The addition of these extra components can lead to the presence of unwanted contamination after thermal

treatment. As relatively few examples of batteries fabricated using VP have been reported, there is significant opportunity to explore new VP material systems, with the goals of increasing structure relative density, material purity, and resolution.

1.4.2 3D batteries: Challenges and opportunities

3D printing technologies for battery applications face challenges of balancing printability, resolution, and active material mass loading. Reported techniques do not yet satisfy these factors at the levels that would be needed to provide superior energy and power density compared to existing commercial batteries. In addition, evaluations of 3D printed batteries are necessary for the cost, manufacturing rate, and safety of practical battery applications. Unmet needs for 3D printed batteries are electrochemically inactive materials such as current collectors, separators, and packaging. These materials must be incorporated or printed at a small scale similar to that of commercial batteries (i.e., 1-10 μm scale).

1.4.3 3D batteries: Applications and outlook

The potential applications of 3D printed batteries, which offer precise control of form factors with low throughput, compared with current battery manufacturing technology, are the ones that require unusual form factors and a good combination of energy and power density with high value. The target markets include the Internet of Things (IoT), micro-robotics, unmanned aerial vehicles (UAVs), and electric vertical takeoff and landing (eVTOL). These applications have restrictions in form factors of battery cells, which are not easily achievable by conventional roll-to-roll manufacturing. In particular, mechanically resilient 3D batteries such as 3D carbon electrodes manufactured via VP could be useful as multifunctional batteries, with promise in aerospace applications that require lighter battery and structural components. Toward fully 3D batteries at a package level, the most difficult challenges exist in the compatibility of manufacturing processes for all the components, including the battery pack. The direct 3D printing of all the components is preferable in terms of both cost and rate compared to current commercial manufacturing methods, since all components on the 3D complex structure need to be precisely matched. Manufacturing processes that enable coating on complex structures such as a UV-curable polymer electrolytes are key for fully 3D batteries. Additionally, technologies that enable merging inactive materials with minimized volumes into the 3D complex structure are critical to obtain comparable energy density to commercial batteries at a package level.

Other potential applications of 3D printed batteries include battery diagnostics and electrochemically reconfigurable materials. 3D printed batteries offer deterministic, controllable, and prescribed form factors, enabling easy battery diagnostics for their rate performance and battery cycling. This approach has been used to create 3D reconfigurable and programmable architecture induced by electrochemical lithium alloying [67]. Overall, the flexible form factors offered by 3D printing enable optimization of ion and electron transport trajectories with or without interdigitated electrode structures for overcoming the classical tradeoff relationship between energy density and power density. 3D printing also provides promising paths to mechanically robust architectural design for materials with significant volume change, and other applications including battery diagnostics and reconfigurable devices. Several challenges remain: manufacturing full cells without compromising active material loading fraction, improving resolution to match the submicron scale at which volume-change materials are tolerant to mechanical forces, enhancing cycle life, and achieving high throughput. Addressing these challenges will lay the foundation for the design and fabrication of practical additively manufactured, high-performance, fully 3D batteries.

1.5 Thesis summary

This thesis focuses on the development of two new techniques for additively manufacturing functional materials via vat photopolymerization.

Chapter 2 focuses on using emulsions to introduce aqueous precursors into a photopolymer resin. We show how this technique can be used to create lithium sulfide composites for use as cathodes in lithium-sulfur batteries, and investigate the electrochemical performance of these composites. We also investigate via nanomechanical compression experiments the mechanical properties and deformation mechanisms of lithium sulfide, a constituent material in lithium-sulfur batteries.

Chapter 3 focuses on the development and optimization of hydrogel infusion additive manufacturing (HIAM) for fabricating copper metal. HIAM enables the fabrication of metals through a process of infusing metal precursors into a hydrogel scaffold, followed by calcination and reduction to convert the precursor to metal. Copper is a notoriously challenging material to fabricate using conventional additive manufacturing technique due to its high thermal conductivity; we demonstrate the fabrication of copper microlattices with beam diameters of ~40 μm, as well as the chemical and structural characterization of these materials.

Chapter 4 extends the HIAM technique to fabricate and characterize a wide variety of new materials, including pure metals (Cu, Ni, Ag), homogenous alloys (CuNi), heterogenous alloys (CuAg), high entropy alloys (CuNiCoFe), and refractory alloys (W-Ni). We show that the high annealing twin densities typical of HIAM metals have interesting implications for the mechanical behavior of these materials as measured by nanoindentation.

Finally, Chapter 5 offers a concise summary of the investigations of this thesis, as well as an outlook on additive manufacturing of functional materials, and remaining research directions.

Chapter 2

UNDERSTANDING AND MITIGATING MECHANICAL DEGRADATION IN LITHIUM-SULFUR BATTERIES

Chapter abstract

Lithium–sulfur batteries are poised to outcompete lithium-ion batteries in key sectors such as transportation and grid storage due to the low cost and high theoretical energy density of sulfur as a cathode material. Widespread implementation of this technology is hindered by significant degradation during cycling, including mechanical failure via cracking or detachment of insulating lithium sulfide (Li_2S) from the conductive matrix in the cathode, causing irreversible capacity fade. We developed a technique to additively manufacture Li_2S composites to fabricate rationally designed cathodes and demonstrate the utility of a three dimensionally architected Li_2S composite cathode in a battery. We additionally measured material properties and deformation mechanisms of Li_2S powders via in situ scanning electron microscope (SEM) nanomechanical particle compression experiments. Measuring these mechanical properties is a first step towards understanding the process of mechanical degradation and is necessary to enable the rational design of high energy density, long-cycling, and mechanically robust sulfur cathodes.

This chapter has been adapted from:

1. Saccone, M. A.; Greer, J. R. Understanding and mitigating mechanical degradation in lithium–sulfur batteries: Additive manufacturing of Li_2S composites and nanomechanical particle compressions. *Journal of Materials Research* **2021**, 36, 3656–3666, DOI: 10.1557/s43578-021-00182-w.

Contributions: M.A.S. conceived, designed, and performed the experiments, and wrote the manuscript.

2.1 Introduction: Lithium-sulfur batteries

2.1.1 Battery background

An electrochemical cell converts between chemical energy and useful electrical energy. The fundamental driving force in an electrochemical cell is a chemical reaction between neutral species that yields an electrically neutral and thermodynamically favored product. An electrically insulating and ion conducting separator and an ion conducting electrolyte allow ions to cross from one side of the cell to the other; to maintain charge neutrality, electrons must flow in an external circuit, where they are used to do work. Cells can be arranged in series or in parallel as batteries to meet the voltage and current requirements for a wide range of applications which require convenient access to electricity or energy storage. Batteries have become ubiquitous in modern life due to their use in a wide variety of technologies such as micro-robotics, smartphones, electric vehicles, and grid-scale energy storage. Despite the fact that each of these applications can have very different requirements (for example, micro-robotics requires high gravimetric power density, while the most important factor in grid-scale energy storage is system cost), these technologies are predominantly served by lithium-ion (Li-ion) batteries.

2.1.2 Li-S overview

The overall driving chemical reaction of the Li-S battery is

$$16\,\mathrm{Li\,(s)} + \mathrm{S_8\,(s)} \longrightarrow 8\,\mathrm{Li_2S\,(s)} \tag{2.1}$$

where lithium is the anode material, sulfur is the cathode material, and Li^+ is the working ion. This mechanism is an example of a reconstitution/formation reaction because chemical bonds are broken and formed (as opposed to an intercalation reaction, where a guest species is inserted into unoccupied interstitial sites of a stable host material) and a new phase, lithium sulfide (Li_2S), is formed at the cathode [68].

The mechanism of sulfur reduction in Li-S batteries has been the subject of many studies, and has been found to depend strongly on the type and amount of electrolyte present in the system. In conventional liquid electrolytes which exhibit high solubility for polysulfide species (Li_2S_x, 2<x<8), sulfur reduction proceeds through a solution-mediated pathway where complex equilibrium exists between the various polysulfide species [69]. The discharge curves of these systems typically exhibit plateaus at approximately 2.4 V and 2.1 V (vs. Li/Li^+), which are often ascribed to the formation of long chain and shorter chain polysulfides, respectively [70]. Con-

versely, in all-solid-state Li-S batteries, which employ a solid electrolyte, a direct solid state conversion between S_8 and Li_2S is observed, yielding a discharge curve with a single plateau [71]. It has recently been demonstrated that by using sparingly solvating liquid electrolytes with high salt loading, the sulfur reduction mechanism in liquid electrolyte batteries can be a quasi-solid state mechanism [72, 73] which approximates the single plateau behavior of solid state Li-S batteries.

The theoretical capacity of the Li-S battery based on sulfur is calculated to be 1672 mAh/g_s using the equation

$$Capacity = \frac{x}{W_t}F \tag{2.2}$$

where x is the number moles of electrons transfered per mole of reaction, 2 for this reaction, W_t is the molar mass of sulfur, 32.066 g/mol, and F is Faraday's constant, 96485.33 C/mol. Equation 2.2 calculates the capacity in C/g, and must be converted to the more common units of mAh/g by an additional factor of mAh/3.6C.

If Li-S batteries were able to effectively harness their massive theoretical energy density of ~2600 Wh kg^{-1}, 10x that of Li-ion batteries [74], they would revolutionize the electrification of transportation and grid-scale energy storage. The unprecedented lightness of Li-S batteries and the 86% projected cost savings ($36 vs. 250 \$ kWh^{-1}_{system}) over Li-ion batteries could spur the proliferation of economical electric vehicles [75, 76]. The low-cost sulfur cathode renders Li-S batteries an ideal candidate for grid-scale energy storage, which is necessary to smooth intermittent energy generation from renewables, such as wind and solar, and facilitate a 100% renewable energy economy.

2.1.3 Li-S challenges and state of the art

Several significant challenges prevent realization and insertion of Li-S batteries into energy systems, which include the numerous chemical and physical degradation mechanisms of electrolyte decomposition [77], polysulfide shuttling [78, 79], lithium dendrite growth [80], and formation of "dead" sulfur or lithium sulfide (Li_2S) caused by their loss of contact with the conductive matrix [81]. Mitigating such degradation is necessary for widespread implementation of Li-S batteries. A significant amount of work has been dedicated to furthering mechanistic understanding of the Li-S system [82], and many mitigation strategies have been developed; for example Pang et al. demonstrated the ability of solvate electrolytes to mitigate electrolyte reactivity, polysulfide shuttling, and lithium dendrite growth [73]. This is accomplished by modifying the Li-S reaction pathway from a dissolution-precipitation

mechanism to a quasi-solid-state or solid-state conversion. Such advances in electrolyte design provide a convincing path towards solving many of the overall Li-S battery problems, but mechanical degradation of solid constituents remains poorly understood.

Mechanical degradation in Li-S batteries is thought to be caused by fracture or detachment of Li_2S from the conductive matrix in the cathode, driven by the lithiation-induced 80% volumetric expansion of sulfur as it is converted to Li_2S [83]. While mechanical properties, degradation, and stress evolution have been explored in other systems with large volume changes during cycling [84], a dearth of studies exists on the Li-S system. The only experiments measuring stress evolution in Li-S batteries come from in situ multibeam optical stress sensing experiments in liquid electrolyte cells, which provide some insight but cannot measure spatially resolved stress [85, 86]. Measuring stress at site-specific locations where detachment or fracture is likely to occur, such as within grains of Li_2S or at the Li_2S-matrix interface, would enable the rational design of cathode structures and matrix materials that can accommodate these stresses. The experimental challenges associated with measuring Young's modulus and other mechanical properties of Li_2S, which rapidly hydrolyzes in air via the reaction $Li_2S + 2\,H_2O \longrightarrow 2\,LiOH + H_2S$, have yet to be overcome, and its mechanical deformation mechanisms are yet unknown.

The problem of mechanical failure in Li-S batteries has been partially addressed by fabricating cathode materials with built-in void space [87] or by assembling batteries in the discharged, pre-expanded state with Li_2S composite cathodes [88]. An increased focus has been given to expansion-tolerant architectures with optimized binder compositions, which enable stable cycling of high-loading sulfur cathodes, but do not offer a route towards full tunability and optimization of the structures [89]. A nascent set of strategies to increase the robustness, mass loading, and power density of battery electrodes utilizes additive manufacturing (AM), whereby structures are formed in a layer-by-layer process, allowing for full control over the form factor and the dimensions of the fabricated material. AM processes for battery materials have enabled the fabrication of interdigitated electrodes, [36] which have higher power density than planar electrodes due to increased interfacial area, as well as electrodes with low tortuosity [56], high active material loadings, and geometries that facilitate ionic and electronic transport [37]. Extrusion methods have proven to be capable of 3D printing interdigitated $Li_4Ti_5O_{12}$ anodes and $LiFePO_4$ cathodes for Li-ion batteries [39, 90], as well as sulfur copolymer-graphene cathodes,

sulfur/carbon slurries for Li-S batteries [45, 60], and conductive templates for sulfur infiltration [46]. These extrusion-based AM methods suffer from low resolution; no AM techniques capable of fabricating sulfur composites with features below 150 µm or Li_2S composites with any dimensions have been reported, partially because of the difficulty of working with this air sensitive material. This informs our choice to explore vat polymerization AM methods, which enable higher resolution than extrusion methods and allow fabrication of more complex features such as overhangs [30]. Additionally, we chose to explore emulsification as a way to combine photocurable resin with the water-soluble Li_2S precursor lithium sulfate hydrate ($Li_2SO_4 \cdot H_2O$). Emulsification of resins containing an oil phase (monomers or oligomers) and an aqueous phase has previously been reported as a way to additively manufacture porous structures [91, 92]. To our knowledge, emulsification has never been reported as a way to deliver an active material or precursor into an additively manufactured structure.

2.2 Emulsion stereolithography for fabrication of 3D Li_2S-C cathodes

We developed an additive manufacturing process, coined as emulsion stereolithography, that is capable of fabricating 3D architected Li_2S-C cathodes with 50 µm features, a threefold improvement in resolution over existing architected Li-S cathode materials.

2.2.1 Emulsion stereolithography process

Figure 2.1 shows the fabrication steps of the AM process for architected Li_2S-C cathodes. It consists of 1) synthesis and preparation of the emulsion resin, 2) digital light processing (DLP) stereolithography to produce the designed 3D architecture, and 3) pyrolysis in an inert atmosphere. The emulsion resin was prepared by dispersing an aqueous solution of lithium sulfate hydrate ($Li_2SO_4 \cdot H_2O$) in a commercial UV-curable photopolymer resin (Autodesk PR-48; see Table A.1 for resin composition) with the aid of surfactants (Fig. 2.1(a)). This emulsion resin is a metastable water-in-oil (w/o) emulsion of lithium sulfate hydrate solution dispersed within a continuous phase of photopolymer resin (Fig. 2.1(b)). Our choice of $Li_2SO_4 \cdot H_2O$ stems from its stability in air, commercial practicality, and ease of conversion of Li_2SO_4 to Li_2S via the carbothermal reduction reaction $Li_2SO_4 + 2\,C \longrightarrow Li_2S + 2\,CO_2$ [93, 94]. The main challenge with $Li_2SO_4 \cdot H_2O$ is the lack of resin system stability caused by its low solubility in the polar PR-48 resin.

The addition of polyvinylpyrrolidone and Polysorbate 20 amphiphilic surfactants serves to suppress Ostwald ripening of the dispersed aqueous droplets by reducing the total interfacial energy between water and oil and to prevent phase separation [95]. The presence of these surfactants significantly increased the stability of the w/o resin emulsions, as evidenced by the time-lapse photographs of the emulsion (Fig. 2.1(c)), which demonstrate that the aqueous phase remains emulsified even after several days. Without the addition of surfactants, the oil and water components of the resin phase separated almost immediately (see Fig. A.3). We then used a DLP 3D printer (Autodesk Ember) to sculpt the photopolymer resin into a target architecture (Fig. 2.1(d)) designed to be disc-like, with a diameter of 25 mm and a height of 2 mm, comprised of a periodic array of 1 mm-wide octet unit cells, with 120 μm diameter beams (Fig. 2.1(e)). These samples were then pyrolyzed at 800 °C for 4 hours in an inert atmosphere, producing self-similar Li_2S-C composite replicas with diameters of 10 mm and heights of 800 μm, caused by 60% linear dimensional shrinkage (Fig. 2.1(f)).

2.2.1.1 Emulsion resin preparation and printing

First, a 3.13 M solution of $Li_2SO_4 \cdot H_2O$ (99.0%, Alfa Aesar), and a 600 mg/mL solution of polyvinylpyrrolidone M_w = 40000 (PVP; Sigma-Aldrich) were prepared by vortex mixing the solids in deionized water until fully dissolved. In each of 3 50mL centrifuge tubes, 4.55 mL $Li_2SO_4 \cdot H_2O$ solution was added to 0.7 mL PVP solution and 1.75 mL Polysorbate 20 (Alfa Aesar). These solutions were vortex mixed for 15 minutes, yielding a soapy, white mixture. To this mixture, 35 g of PR-48 (Colorado Photopolymer Solutions) was added, followed by 75 minutes of vortex mixing to yield a milky white emulsion resin. Immediately after mixing, this resin was used with a commercial 405 nm wavelength DLP 3D printer (Autodesk Ember) to fabricate $Li_2SO_4 \cdot H_2O$–polymer composite structures. Octet microtruss lattice unit cells were designed with 120 μm beam diameter and 1mm unit cell size. Unit cells were tessellated to form freestanding circular cathodes with outer diameter of 25mm and thickness of 2mm. The first layer was exposed to UV light for 9 sec to ensure adherence between the structure and the build head, and subsequent layers were exposed for 5 sec.

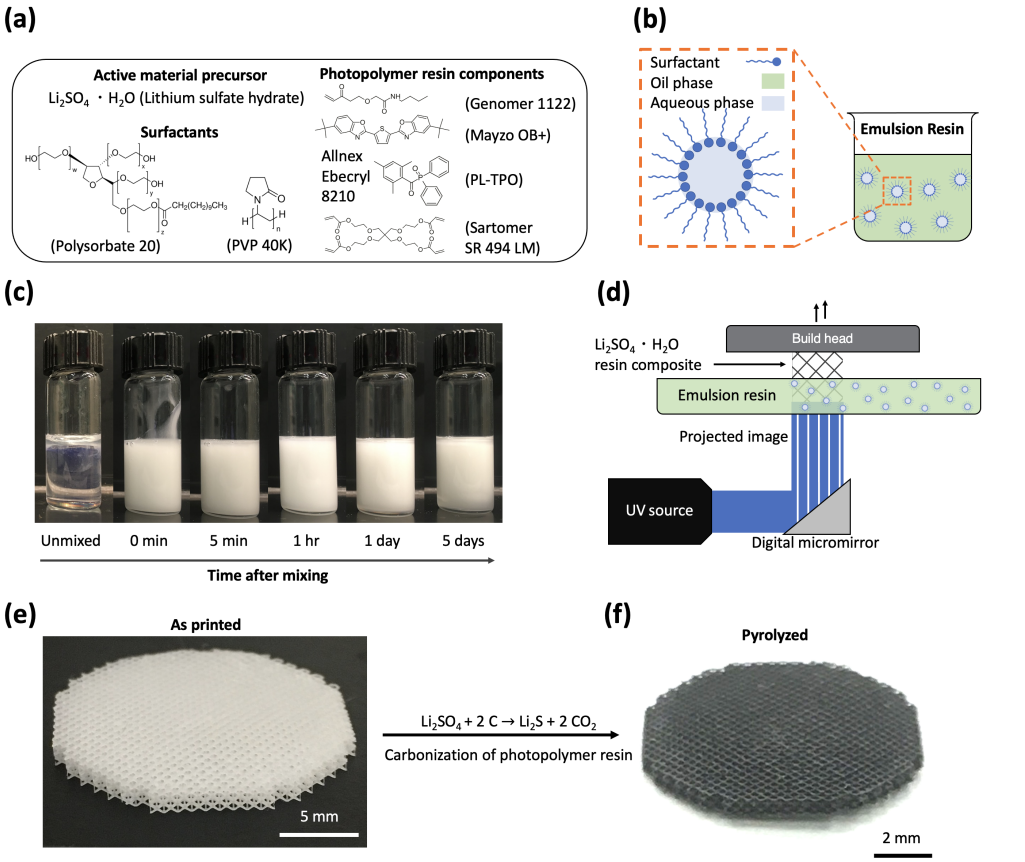

Figure 2.1: **Emulstion stereolithography of Li_2S-C composite electrodes.** (a) Chemical components of emulsion resin formulation. (b) Schematic of water-in-oil emulsion of aqueous active material precursors dispersed in an organic photopolymer resin and stabilized by surfactants. (c) Time lapse photographs of emulsion resin up to five days after mixing that demonstrates its stability; the emulsion remains opaque due to dispersed water droplets. (d) Schematic of DLP printing of a $Li_2SO_4 \cdot H_2O$ resin composite. The sample is printed directly on the build head and then detached. Optical images of (e) a representative as-fabricated $Li_2SO_4 \cdot H_2O$ resin composite structure and (f) its pyrolyzed Li_2S-C composite replica.

2.2.1.2 Pyrolysis of $Li_2SO_4 \cdot H_2O$-polymer composites

The $Li_2SO_4 \cdot H_2O$-polymer composites were pyrolyzed in a vacuum furnace (MTI OTF-1500X) in a quartz tube (MTI, 1 m length, 92 mm inner diameter). The tube was first evacuated, then refilled to atmospheric pressure with argon, which was flowed through a bubbler downstream to prevent air exposure. The samples were heated at a ramping and cooling rate of 5 °C/min, with 2-hour isothermal holds during ramping at 300 °C and 400 °C, and a 4-hour isothermal hold at the maximum temperature of 800 °C. The pyrolyzed Li_2S-C composite samples were unloaded from the furnace into an argon-purged jar from inside a nitrogen filled glove bag (see fig. 2.2(a)) to prevent air exposure. The sealed jar containing the Li_2S-C samples was then brought into an argon-filled glovebox for coin cell assembly.

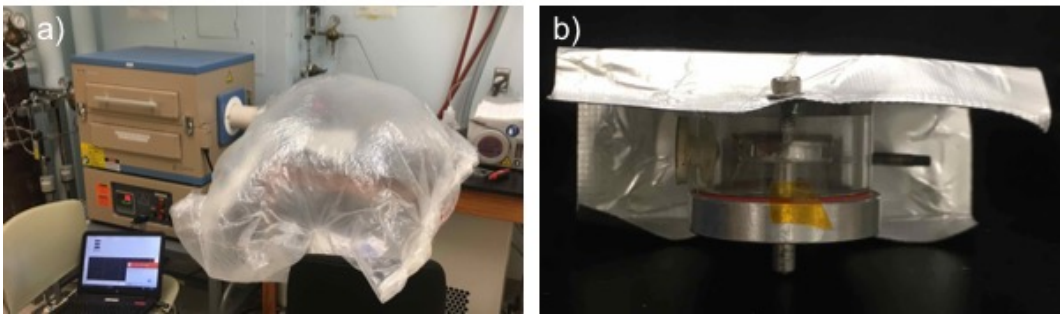

Figure 2.2: **Airtight transfer devices.** (a) Glove bag filled with N_2 for removing samples from furnace and (b) Vacushut transfer device enables SEM imaging of air sensitive samples.

2.2.2 Li_2S-C electrode morphology

Figure 2.3 contains structural characterization of a representative Li_2S-C microtruss lattice with a designed relative density, defined as the volumetric fraction of filled space within the structure, of 16%. The specific octet microtruss architecture was chosen to demonstrate the capability of emulsion stereolithography to produce complex geometries with overhangs and slender beams, inaccessible to extrusion-based AM processes. Fig. 2.3(a) shows a computer-aided design (CAD) model of a single octet unit cell. Figures 2.3(b, c) contain scanning electron microscope (SEM) images of the designed architecture of the Li_2S-C lattices, and Fig. 2.3(d) provides an SEM image of a representative 50 µm-diameter beam. The beams in the as-printed $Li_2SO_4 \cdot H_2O$ composite structure were designed to have 120 µm diameters, which implies pyrolysis-induced linear shrinkage of 58%. The presence of non-polymerizable aqueous domains and surfactants in the resin emulsion generates porosity at a range of length scales, which was analyzed using image analysis software. Micropores were observed with an average diameter of 10.06 µm ± 0.26 µm (avg. ± std. err.) with a standard deviation of 4.15 µm. Additionally, mesopores with an average diameter of 42 ± 1.0 nm with a standard deviation of 15.3 nm were observed on the surface (Fig. 2.3(e, f)). The surfactant loading played a key role in the pore size distribution, with lower surfactant loadings leading to larger, scarcer pores (see Fig. A.4).

2.2.3 Chemical characterization of Li_2S-C composites

During pyrolysis, the lithium sulfate hydrate is first dehydrated and then carbothermally reduced to lithium sulfide, and the polymer composite is converted to carbon via the carbothermal reduction reaction $Li_2SO_4 + 2\,C \longrightarrow Li_2S + 2\,CO_2$. Figure 2.5 contains chemical characterization of the $Li_2SO_4 \cdot H_2O$ composite before and after pyrolysis at 400 °C and 800 °C to elucidate the different stages of the pyrolysis

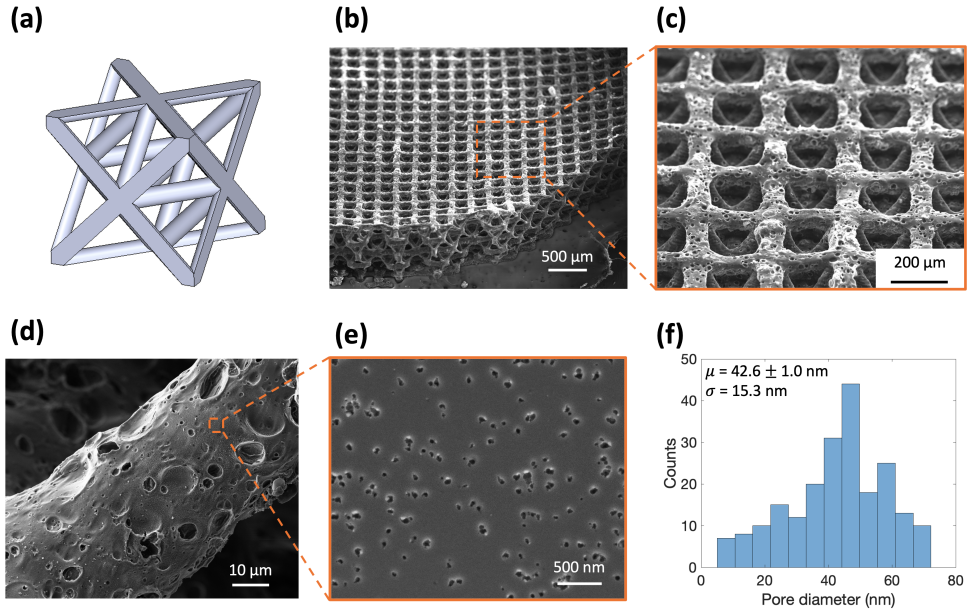

Figure 2.3: **Morphology and surface properties of pyrolyzed Li_2S-C electrodes.** (a) 3D model of an octet unit cell. SEM images of (b) a pyrolyzed Li_2S-C octet microtruss lattice (tilt 40°), (c) several beams on the top surface of the lattice, (d) a single 50 µm diameter beam, and (e) surface morphology that contains nm-scale porosity introduced by the non-polymerizable components in the emulsion resin. (f) Histogram of the nm-scale pore size distribution on the surface of the Li_2S-C lattice.

process. We conducted thermogravimetric analysis (TGA) on a resin sample that consisted of 74.5 wt% PR-48, 18 wt% H_2O, and 7.5 wt% $Li_2SO_4 \cdot H_2O$, which reveals three distinct regions that correspond to different chemical processes (Fig. 2.5(a)). Below 300 °C, the $Li_2SO_4 \cdot H_2O$ is dehydrated, and any water remaining in the composite from the printing process is evaporated. The region between 300 °C and 450 °C corresponds to the carbonization of the organic elements of the photopolymer. The final region above ~675 °C corresponds to the carbothermal reduction of lithium sulfate and likely some further carbonization of the organic photopolymer. X-ray diffraction (XRD) analysis was conducted on a $Li_2SO_4 \cdot H_2O$ composite at various stages of pyrolysis corresponding to the labeled locations on the TGA curve of 1) as printed, 2) 400 °C pyrolysis, and 3) 800 °C pyrolysis. In the as-printed sample, XRD analysis reveals the presence of crystalline lithium sulfate hydrate in the polymer composite (Fig. 2.5(b)), deposited into the residual pores within the 3D-sculpted structures after polymerization, created by dispersed water droplets in the photopolymer resin. XRD analysis of the $Li_2SO_4 \cdot H_2O$ composite pyrolyzed at 400 °C confirms that the $Li_2SO_4 \cdot H_2O$ was fully dehydrated to anhydrous Li_2SO_4 (Fig. 2.5(c)).

XRD analysis of a composite printed from a $Li_2SO_4 \cdot H_2O$ emulsion resin and pyrolyzed in an inert atmosphere at 800 °C shows complete conversion of Li_2SO_4 to Li_2S (Fig. 2.5(d)). The broad peak around $2\theta = 20°$ is background from Kapton tape used to shield the sample from air (Figure A.2). Energy-dispersive X-ray spectroscopy (EDS) indicates a homogeneous distribution of sulfur in the beams (Fig. 2.5(e), bottom left panel), which is consistent with the presence of Li_2S; EDS is not capable of detecting Li because of its low atomic number. The 0.3 wt% of phosphorous (Fig. 2.5(e), bottom right panel) likely represents a degradation product of the phosphorous-containing PL-TPO photoinitiator molecule. The observed octahedral morphology of the crystals (Fig. 2.5(f)) is consistent with the equilibrium Wulff construction shape for Li_2S which minimizes the surface energy of the crystal by faceting along (111) planes [96].

2.2.3.1 Material characterization experimental details

Samples were imaged via scanning electron microscopy (SEM; FEI Versa 3D DualBeam) at an accelerating voltage of 5-20 kV. Elemental analysis was performed using energy-dispersive X-ray spectroscopy (EDS; Zeiss 1550 VP FESEM with Oxford X-Max SDD EDS detector), with an applied voltage of 20 kV. A Vacushut transfer device (see Fig. 2.2b) was used to minimize air exposure during the transfer of air sensitive samples from the glovebox to the SEM or SEM/EDS. Powder X-ray Diffraction (XRD; PANalytical X'Pert Pro) data was collected using a Cu K_α source at 45 kV and 40 mA. Samples were either ground into powders with a mortar and pestle, or if the sample had a flat edge, attached to a sample holder using clay prior to XRD analysis. Air-sensitive samples were sealed between 2 layers of Kapton tape to prevent air exposure during XRD measurements. Thermal gravimetric analysis (TGA; Perkin Elmer Pyris) was performed by heating samples to 900 °C at a rate of 5 °C/min in a N_2 atmosphere while the mass of the sample was continuously measured.

2.2.4 Na_2S-C composites

Emulsion stereolithography is not limited to producing composites with Li_2S; this technique can be used to fabricate carbon composites with any material that has water soluble precursors. To demonstrate this, Na_2S-C composites were fabricated using the same methodology described previously in Section 2.2.1 but with aqueous Na_2SO_4 solutions instead of aqueous $Li_2SO_4 \cdot H_2O$ solutions. The resulting Na_2SO_4 polymer composites were converted to Na_2S-C composites via pyrolysis by

the carbothermal reduction reaction $Na_2SO_4 + 2\,C \longrightarrow Na_2S + 2\,CO_2$. Since Li and Na are both Group 1 alkali metals, it is not surprising that they undergo similar carbothermal reduction reactions. The Na_2SO_4/Na_2S system provides further evidence for the mechanism of salt deposition in the printed parts because Na, unlike Li, can be observed in the EDS results.

Salt crystals (in this case Na_2SO_4) are deposited in cavities formed by water droplets during polymerization, and are unambiguously identified by electron energy dispersive x-ray spectroscopy (EDS) and XRD (Figs. 2.4a/c). The presence of crystalline Na_2S after pyrolysis is confirmed by EDS and XRD as well (Figs. 2.4b/d). Oxygen is likely present in the EDS mapping of the pyrolyzed sample due to exposure to air causing hydrolysis during a transfer step.

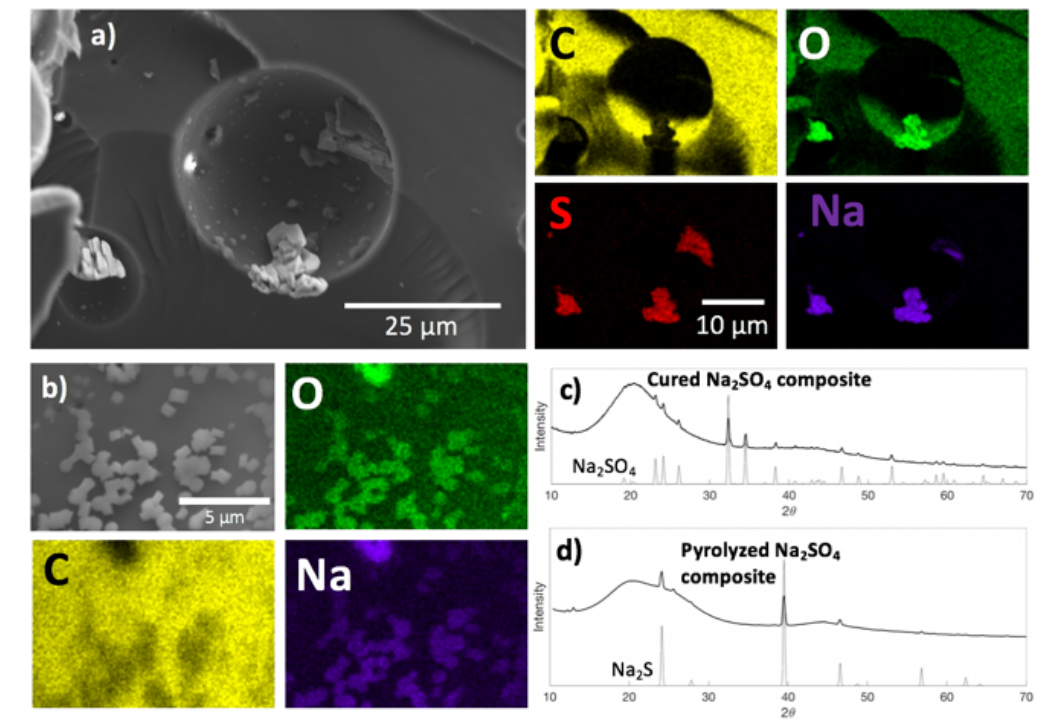

Figure 2.4: **Characterization of Na_2SO_4 and Na_2S composites.** (a) SEM/EDS images of Na_2SO_4-containing polymer composite showing deposition of Na_2SO_4 crystals inside of pores created by emulsified water droplets. (b) SEM/EDS images of pyrolyzed samples after exposure to air which caused formation of NaOH. (c) XRD patterns of Na_2SO_4 composites before pyrolysis and (d) Na_2S composites after pyrolysis without air exposure.

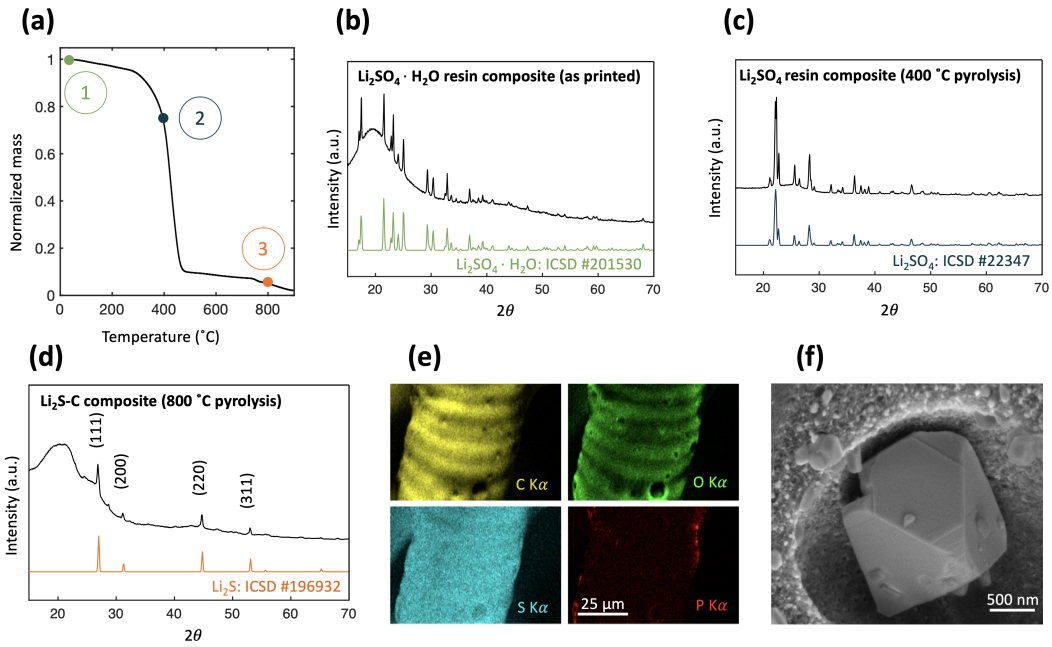

Figure 2.5: **Chemical and morphological characterization of architected Li2S-C.**(a) Thermal gravimetric analysis (TGA) of a $Li_2SO_4 \cdot H_2O$/polymer composite showing substantial mass loss during pyrolysis. Numbers correspond to the maximum pyrolysis temperatures for three different samples where XRD data was collected: 1) as printed (before pyrolysis), 2) after 400 °C pyrolysis, and 3) after 800 °C pyrolysis. X-ray diffraction (XRD) spectra of (b) as-fabricated $Li_2SO_4 \cdot H_2O$ resin composite, which contains crystalline $Li_2SO_4 \cdot H_2O$ (location 1 in TGA data), (c) composite pyrolyzed at 400 °C, which reveals crystalline Li_2SO_4 (location 2 in TGA data), and (d) fully pyrolyzed at 800°C Li_2S-C composite that reveals crystalline Li_2S (location 3 in TGA data) (e) EDS elemental maps of a beam, which indicate homogeneous distribution of sulfur at the spatial resolution of EDS (~1 μm). (f) SEM image of a faceted octahedral lithium sulfide crystal present in the Li_2S-C sample.

2.3 Electrochemical performance of 3D Li_2S-C cathodes

2.3.1 Experimental details

2.3.1.1 Coin cell assembly

1,3-dioxolane (DOL, VWR) and dimethoxyethane (DME, VWR) were dried on a solvent purification system, brought into the glovebox without air exposure and stored over 3Å molecular sieves. Lithium bis(triflouromethanesulfonyl)imide salt (LiTFSI; 99.95%, Sigma-Aldrich) was dried at 120 °C under vacuum and brought into the glovebox without air exposure.

Electrochemical cells were prepared in 2032 coin cell cases (MTI). The cells consisted of a Li-foil anode (99.9%, 0.75mm, Sigma Aldrich), which was mechanically cleaned directly preceding cell assembly, polypropylene separator (Celgard 2400), 15 drops of electrolyte, and an architected Li_2S-C free-standing cathode. The electrolyte was prepared in the glovebox as a 1M solution of LiTFSI in a 1:1 (vol/vol)

mixture of DOL and DME, by adding the solvents to the salt, followed by 1 wt% $LiNO_3$, and magnetically stirring at 550 rpm overnight.

2.3.1.2 Electrochemical characterization

Coin cell performance was evaluated using a battery cycler (Neware BTS4000), via galvanostatic cycling between 1.6-2.8 V at a rate of C/20 (58.25 mA/g_{Li_2S}), calculated based on a gravimetric capacity of 1165 mAh/g_{Li_2S}. Li_2S-C cathodes were activated by charging to a cutoff voltage of 3.9 V on the first cycle, consistent with oxidative electrochemical activation of Li_2S. Cyclic voltammetry was performed using a potentiostat (Biologic BCS-805), scanning from 1.5-4 V at a rate of 10 µV/s.

2.3.2 Electrochemical performance of 3D architected Li_2S-C cathodes

To demonstrate the feasibility of the emulsion stereolithography additive manufacturing technique to create functional batteries, we fabricated coin cells consisting of a free-standing 3D Li_2S-C composite cathode, a 0.75 mm thick lithium metal foil anode, and an electrolyte consisting of 1M lithium bis(triflouromethanesulfonyl)imide (LiTFSI) salt in a 1:1 (vol/vol) mixture of 1,3-dioxolane and dimethoxyethane (DOL/DME). We also added 1 wt% of $LiNO_3$ salt to the electrolyte to stabilize the solid electrolyte interphase on Li metal to reduce its reactivity and inhibit polysulfide shuttling [97]. Cells containing $LiNO_3$-free electrolyte charged significantly beyond their theoretical capacity (see Fig. 2.6) before reaching a voltage cutoff, a signature of the polysulfide shuttle effect [79].

Figure 2.7 contains the electrochemical performance and characterization of 3D Li_2S-C composites. Cyclic voltammetry experiments show the expected electrochemical signature of the two oxidative peaks at 2.37 V and 2.40 V and reductive peaks at 2.33 V and 2.07 V (Fig. 2.7(a)) [98]. We found that a slow scan rate of 10 µV/s was necessary to produce sharp peaks. The characteristic strong peak at 3.41 V in the first cycle corresponds to the initial oxidative activation of Li_2S and disappears in subsequent cycles [99]. The reductive peaks match well with the voltages of the plateaus observed in the discharging profiles. Galvanostatic cycling of two nominally identical cells at a rate of C/20 showed a cycling lifetime of >100 cycles and a characteristic two-plateau discharge profile, with plateaus at 2.4 V and 2.1 V (Fig. 2.7(b)). The cells were first galvanostatically charged to a cutoff voltage of 3.9 V to oxidatively activate Li_2S in the composite electrode [99]; all subsequent cycling was performed between upper and lower voltage cutoffs of 2.8 V and 1.6

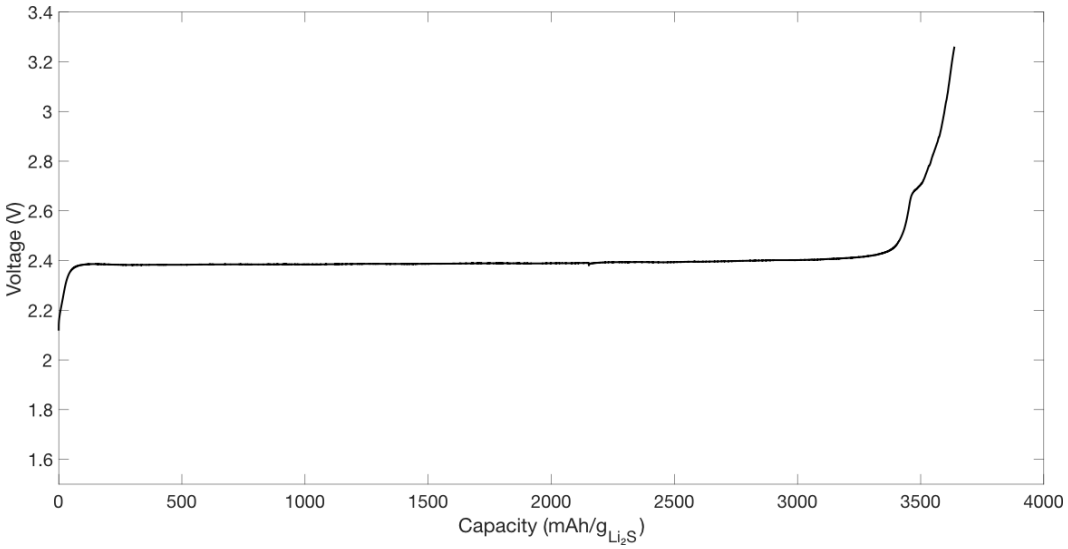

Figure 2.6: **Charging profile for a cell with polysulfide shuttling.** First charge profile of an architected Li_2S-C cathode vs. Li at C/20 rate with 1M LiTFSI in DOL/DME electrolyte without the addition of $LiNO_3$. The cell demonstrates an excessively large charging plateau at ~2.4 V, several times larger than the theoretical capacity of Li_2S (1165 mAh/g), a feature characteristic of the polysulfide shuttle effect.

V, respectively. The replicate cells demonstrated a first cycle discharge capacity of 310.1 mAh/g_{Li_2S}. The average coulombic efficiency of the cells was 95.8%, with 86.6% of the first discharge capacity retained after 50 cycles and 79.8% of the first discharge capacity retained after 100 cycles (Fig. 2.7(c)). Compared to other 3D architected cathodes for Li-S batteries, this cycling performance represents a 19.4% increase in capacity retention after 50 cycles, as well as a 3-fold improvement in minimum electrode feature size (Fig. 2.7(d)). The benchmark of 50th cycle capacity retention was chosen because 100th cycle data was not always available.

2.3.3 3D Li_2S-C electrode discussion

We report the first 3D architected Li_2S-C composite and demonstrate its use as a cathode material. We chose to work with an octet lattice geometry to demonstrate the strengths of the emulsion stereolithography AM process. The Li_2S loading within the pyrolyzed structure was 19%, contributing to an overall Li_2S loading of 1.3 mg cm^{-2}. The Li_2S loading was calculated by assuming that all Li_2SO_4 in the emulsion resin was converted to Li_2S and that none was lost during thermal treatment. The observed first cycle discharge capacity of 310.1 mAh/g_{Li_2S} is lower than the theoretical capacity of 1165 mAh/g_{Li_2S}, which is typical for Li_2S cathode/carbon composite materials due to the low ionic and electronic conductivity of Li_2S, as well as the difficulty of electrochemical activation for this material [100].

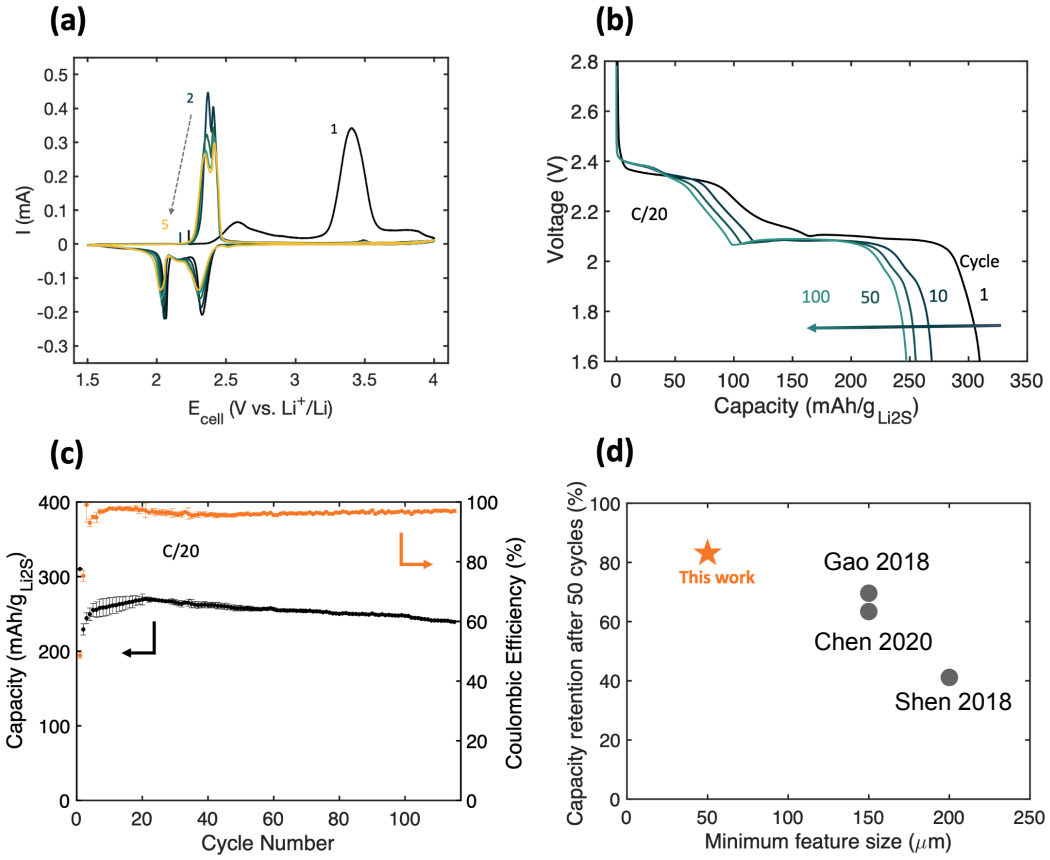

Figure 2.7: **Electrochemical characterization of Li_2S-C composite.** (a) The first five cycles of cyclic voltammograms of an architected Li_2S-C cathode vs. Li metal, at a scan rate of 10 μV/s. (b) Discharge profiles of an architected Li_2S-C cathode vs. Li at C/20 rate for the 1st, 10th, 50th, and 100th cycles. (c) Capacity and coulombic efficiency vs. cycle number for architected Li_2S-C cathodes, with error bars representing the standard error of the mean for two replicate cells. (d) Capacity of architected Li_2S-C vs. other architected cathodes at slow scan rates (C/5 to C/20) [45, 46, 60] for Li-S batteries as a function of minimum critical dimensions.

Interestingly, the observed capacity of our Li_2S-C cathode drops significantly after the first cycle, but then increases from cycle 2 to 20. This may be the result of the sluggish activation process of Li_2S, causing some active material to remain unused after the first cycle, but be accessed on subsequent cycles. Further optimization of 3D architected electrodes will require approaches such as moving towards higher relative density structures in order to achieve loadings of >6 mg cm^{-2} as practically required by industry and incorporating counter electrodes and separators that are conformal to the 3D architected structure. In particular, reducing void space and electrolyte loading while maintaining mechanical integrity will be important for further optimization.

2.4 Nanomechanical particle compression of Li_2S powders

We additionally conducted compression-to-failure experiments on individual micron-sized Li_2S particles in a custom-built nanomechanical instrument inside of an SEM chamber, which revealed elastic deformation up to a contact pressure (i.e., axial compressive stress) of 293 MPa, followed by plasticity over 5% of axial strain, and ultimate failure via catastrophic crack propagation at 389 MPa. We analyzed these experiments using the Hertzian elastic contact model between a sphere (Li_2S sample) and a half-space (indenter tip) to provide estimates for an effective Young's modulus of Li_2S agglomerates, and to calculate contact pressure at the onset of yielding and at ultimate failure.

2.4.1 Particle compression methodology

Future optimization of 3D architected Li_2S composite cathode materials will require a deeper understanding of the mechanical properties and deformation mechanisms of Li_2S. To probe these properties, we performed *in-situ* compression experiments using a nanomechanical probe (InSEM, Nanomechanics, Inc.) inside an SEM chamber (FEI Quanta 200F) (Fig. 2.8a).

Li_2S powder particles (Alfa Aesar) were dispersed on an Si substrate and transferred from an argon filled glovebox into the SEM chamber using a Vacushut transfer device. Samples were compressed with a 15 μm diamond flat punch indenter (Fig. 2.8b) at an axial strain rate, defined as rate of indenter displacement divided by sample height, of 0.01 s^{-1} until failure. A prescribed cyclical dynamic displacement was superimposed over the loading profile, with a target displacement of 2 nm and a frequency of 45 Hz in order to perform continuous stiffness measurements.

During the experiment, load vs. displacement data and deformation video were simultaneously collected. The initial loading segment, up to a displacement of ~100 nm, represents the elastic portion of the data, which can be analyzed using a classical Hertzian elastic contact problem between a sphere and a half-space [101, 102]. Despite the fact that the particle is not a true sphere, over the small initial loading segment, the rounded top surface of the particle can be approximated as the surface of a sphere. The 15 μm-diameter diamond flat punch indenter tip can be approximated as a half space, and the particle as a sphere (Fig. 2.8c). In this formulation, the applied load, F, is related to indenter displacement, δ, as:

$$F_{Hertz} = 4/3 E_R R^{1/2} \delta^{3/2} \tag{2.3}$$

where E_R is the reduced modulus, $1/E_R = (1-\nu_i^2)/E_i + (1-\nu_s^2)/E_s$, in which E_i and ν_i are the Young's modulus and Poisson's ratio of the diamond indenter, respectively, and E_s and ν_s are the Young's modulus and Poisson's ratio of the Li_2S sample. R is the radius of curvature of the top surface of the sample, and δ is the vertical displacement of the indenter past the initial contact with the sample. The radii of curvature of the particle surfaces were approximated to be 1296 ± 128 nm (avg. ± std. dev.) as measured from SEM images.

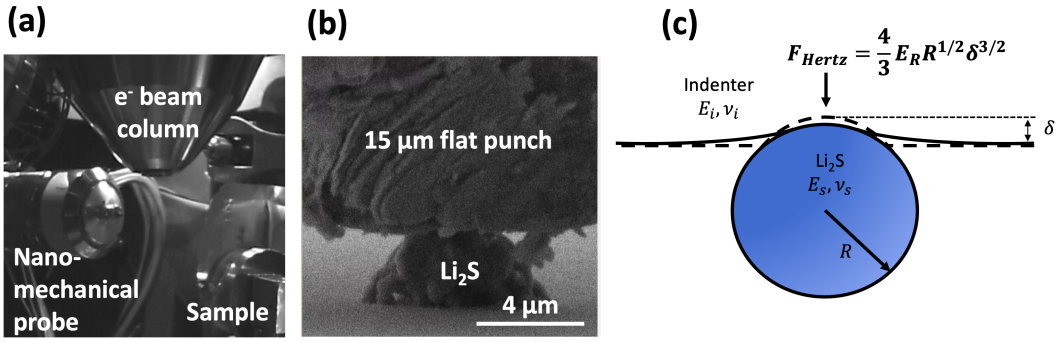

Figure 2.8: **Nanomechanical particle compression methodology.** (a) Image of the interior of the SEM chamber showing the in-situ nanomechanical instrumentation. (b) SEM image of an agglomerated Li_2S particle directly under the diamond flat punch indenter. (c) Schematic of the Hertzian elastic contact model between a sphere and a half space.

2.4.2 Particle compression results

Figure 2.9a contains load vs. displacement data for a representative particle compression, as well as the Hertzian model least squares fit calculated using Eq. 2.3 with the diamond indenter properties of E_i = 1220 GPa and ν_i = 0.2, and the Poisson's ratio of Li_2S of $\nu_s = 0.18$ [103]. The oscillation in the displacement data is a result of a prescribed cyclical dynamic displacement superimposed over the loading profile, with a target displacement of 2 nm and a frequency of 45 Hz. Fig. 2.9(b) contains contact pressure for the same experiment, calculated by dividing the applied load by the instantaneous projected circular contact area:

$$P = \frac{F_{Hertz}}{\pi\delta(2R-\delta)}. \tag{2.4}$$

The post-elastic plateau in contact pressure at a displacement of ~100 nm corresponds to plasticity initiation after yielding that causes deviation from linear elasticity. Due to geometric irregularities, not all particles compressed were suitable for analysis using the Hertzian contact model. Load vs. displacement data was analyzed for 2 samples whose elastic deformation was well described using the

Hertzian contact model. We found that the average Young's modulus of the Li_2S particle agglomerates was 4.81 ± 2.19 GPa (average ± std. err.), with an average contact pressure of 293 ± 153 MPa at yielding and of 389 ± 129 MPa at failure.

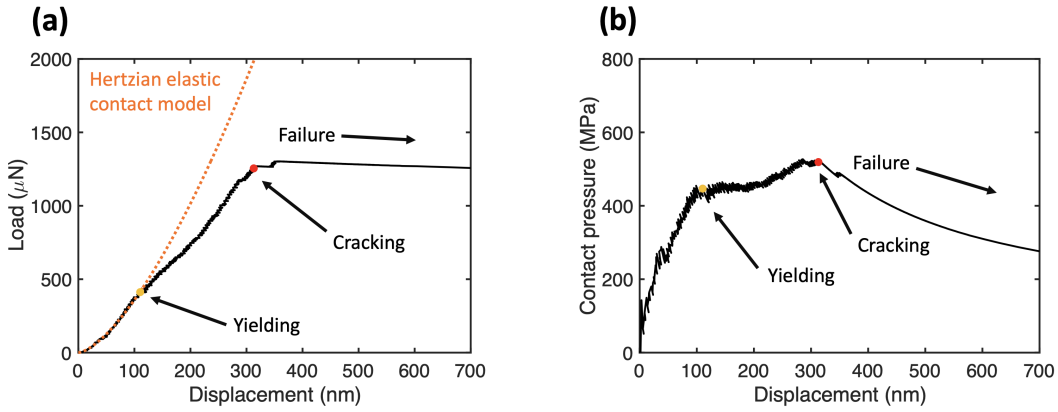

Figure 2.9: **Compression-to-failure experiments on Li_2S.** (a) Load vs. displacement data for a representative particle compression that contains a typical initial elastic loading region, yield point, post-elastic deformation, crack initiation, and ultimate failure. (b) Contact pressure vs. displacement calculated using Eqn. 2.4 with the same regions denoted in (a).

2.4.3 Li_2S particle compression discussion

We focused on investigating the mechanical properties of Li_2S because without a detailed and spatially resolved understanding of the cathode material properties and the mechanical stresses that arise due to cycling, advances in fabrication techniques will not be able to be utilized to the fullest extent. The agglomerated morphology of the powders we tested is similar to common composite electrode morphology, as well as to the observed morphology of electrochemically deposited Li_2S [104]. In order to confirm the validity of the Hertzian contact model as a way to approximate the elastic contact between the indenter and the particle, the scaling exponent of the for the force vs. displacement data of a characteristic compression was analyzed. In the elastic region, the scaling exponent was found to be 1.56, a deviation of only 4% from the 1.5 predicted by the Hertzian contact model (see Fig. 2.10).

Pure Li_2S powder was chosen for this experiment because it enabled more streamlined testing of the pure material with fewer opportunities for contamination or air exposure. Our reported compression-to-failure experiments on Li_2S provide insights towards understanding failure in Li-S cathode materials in a spatially resolved way. The measured Young's modulus of ~5 GPa is lower than expected given the report of Sakuda et al., who measured the Young's modulus of $xLi_2S \cdot (100\text{-}x)P_2S_5$ (x = 50-80) glassy solid electrolytes via ultrasonic sound velocity measurements and found

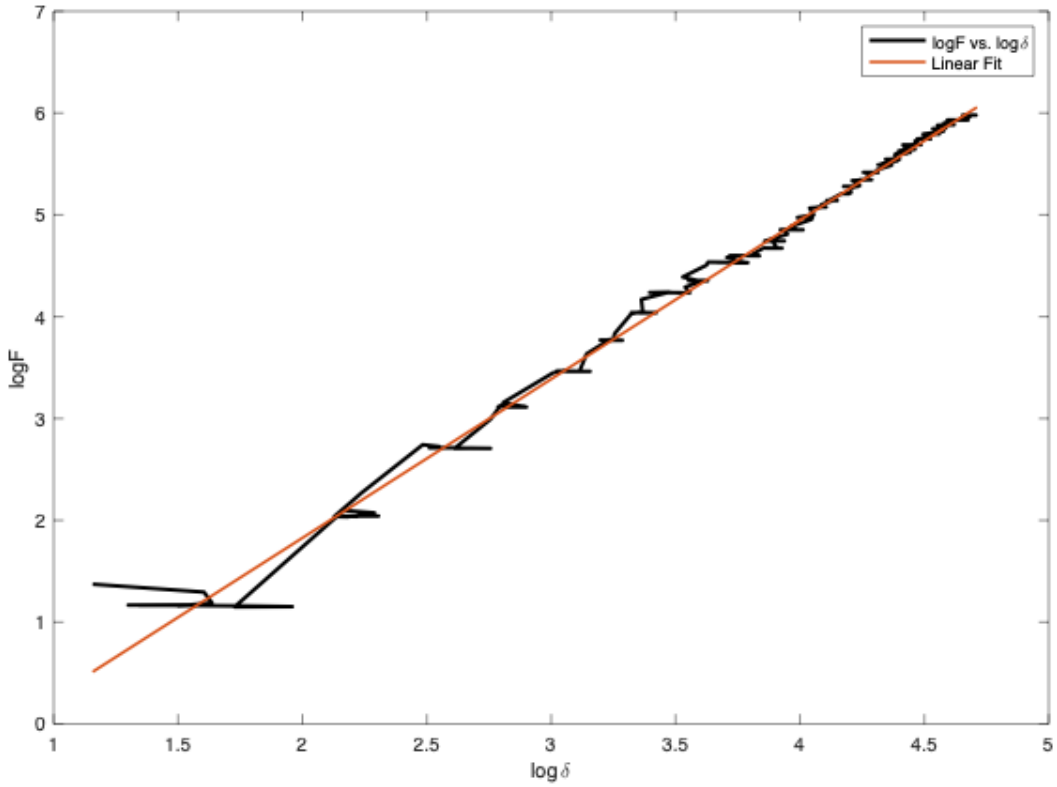

Figure 2.10: **Power law analysis of particle compression.** Analysis of the power law scaling exponent for load F vs. displacement δ of a characteristic particle compression. The slope of the log(F) vs log(δ) for the elastic region is 1.56, a deviation of only 4% from the scaling exponent of 1.5 predicted by the Hertzian contact model.

that these composites had Young's moduli of 18-25 GPa, with Young's modulus increasing with higher Li_2S content [105]. However, the compression results are not entirely surprising given the agglomerated morphology of the powders tested. As such, our reported Young's modulus should be understood as a characteristic of the elastic response of the agglomerated Li_2S, rather than an intrinsic material property. Interpreting the compression-to-failure results in the context of existing research on stress induced during cycling in Li-S helps to shed some light on the mechanical degradation that causes capacity fade. In the compression-to-failure experiments in this work, Li_2S agglomerate cracking occurred at an average contact pressure of ~300 MPa, more than an order of magnitude larger than the measured nominal stresses during battery cycling in the work of Zhang et al., who conducted multi-beam optical stress sensing measurements on 70 µm-thick film composite sulfur electrodes and measured nominal in-plane film stresses of approximately ±10MPa during cycling [79]. This suggests that particle cracking is a negligible degradation mechanism during Li-S cycling and highlights the need for spatially resolved in-situ

stress measurements, particularly to understand the local stress states experienced by Li_2S particles and interfaces between active materials and conductive host materials.

2.5 Li-S battery summary and outlook

We developed emulsion stereolithography-based additive manufacturing process to fabricate air sensitive Li-S cathode materials with feature resolution of 50 μm, which represents a threefold improvement in resolution over existing AM methods. This technique is enabled by a unique combination of resin design to incorporate an aqueous precursor into an organic resin via emulsification with the aid of surfactants, DLP stereolithography, and post-lithography pyrolysis, and offers versatility in form factors and geometry of the electrodes. Future research into the deformation mechanisms of delamination and detachment of active materials from host materials is warranted, with particular need for spatially resolved measurements of stress evolution. This work paves a path forward for synergistically combining nanomechanical measurements for fundamental materials understanding with AM methods capable of fabricating rationally designed electrode architectures to understand and ultimately mitigate the problem of mechanical degradation in Li-S batteries.

Chapter 3

HYDROGEL INFUSION ADDITIVE MANUFACTURING

Chapter Abstract

Additive manufacturing (AM) of metals can enable rapid development of advanced parts with complex geometries, opening potential applications in the aerospace, automotive, and biomedical fields. We report an AM process, coined 'hydrogel infusion additive manufacturing' in which aqueous metal precursors are infused into gels formed via vat photopolymerization, which are subsequently calcined and reduced to form metal structures. Our technique enables the use of a single photoresin composition and varied post-processing conditions to fabricate a wide variety of metals and alloys with microscale resolution and highly twinned microstructures with annealing twin densities on the order of 10^6 m^{-1}. We demonstrate fabrication of microlattices with <50 μm beam diameters formed from copper, nickel, silver, and alloys thereof, as well as high entropy and refractory alloys. We found that during the calcination process, the rate of mass loss associated with the exothermic combustion of the gel scaffold must be controlled to form dense parts. Our simple and compositionally flexible hydrogel-based approach to metal AM provides a pathway to rapidly fabricate new classes of metals. In this chapter, we describe the development and optimization of hydrogel infusion additive manufacturing (HIAM), using copper as a model system.

This chapter has been adapted from:

1. Saccone, M. A.[*†]; Gallivan, R. A.[*]; Narita, K.; Yee, D. W.[†]; Greer, J. R.[†] Microscale fabrication of 3D multicomponent metals via hydrogel infusion. *In review* **2022**. Preprint DOI: 10.21203/rs.3.rs-1108933/v1.

Contributions: M.A.S conceived and designed the experiments, designed the photoresin, fabricated samples, performed material characterization, and wrote the manuscript.

3.1 Introduction: Metal AM

Metal additive manufacturing (AM) enables the production of high value and high performance components [107, 108] for aerospace [109, 110], automotive [111, 112], and biomedical applications [113, 114]. Layer-by-layer fabrication circumvents the geometric limitations of traditional metalworking techniques, allowing topologically optimized parts to be made rapidly and efficiently [115–117]. In particular, high resolution AM is needed in applications where weight savings are critical such as in flapping-wing microrobots [118] (Figure 3.1) and in applications that require very fine features, such as micro electromechanical systems [119] (MEMS, Figure 3.2)

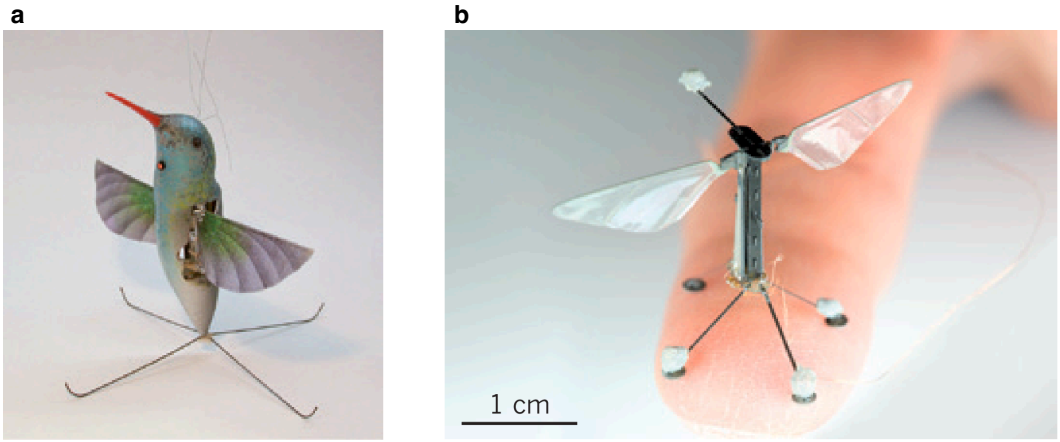

Figure 3.1: **Flapping-wing microrobots.** **a,** The 19 mg Nano hummingbird, and **b,** the 80 mg RoboBee. Adapted with permission from reference [118]. Copyright Nature Research.

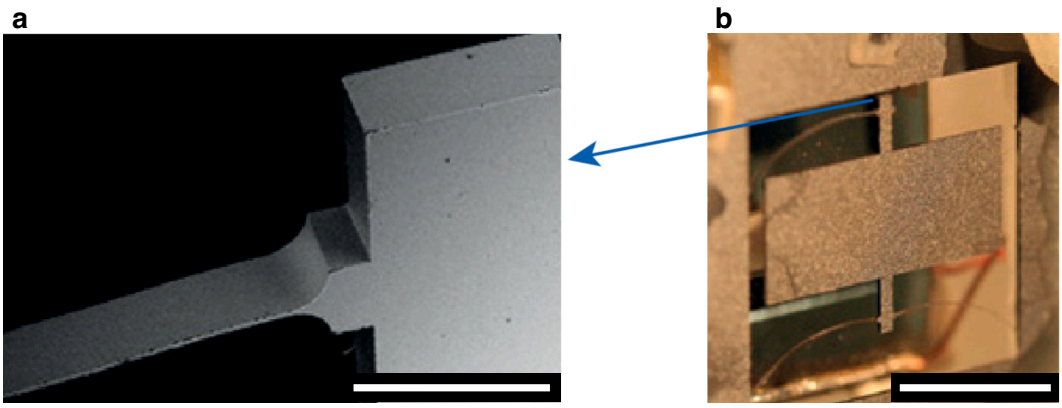

Figure 3.2: **MEMS gravimeter.** A MEMS device capable of measuring Earth's tides. **a,** SEM image showing the fine detail, and **b,** optical image showing overall device design. Scale bars: **a,** 500 µm; **b,** 5 mm. Adapted with permission from reference [119]. Copyright Nature Research.

3.1.1 State of the art metal AM

Existing techniques for metal AM rely on thermally initiated melting or sintering for part shaping, a costly and material-limited process. This is mostly achieved powder bed fusion (PBF) and directed energy deposition (DED) processes, which make use of equipment often costing more than $100,000. Aluminum, magnesium, and titanium can be reliably produced [108, 120–122] but often suffer from cracks and interfacial delamination due to repeated melting and solidification [123–126]. These processes also struggle to produce materials such as copper and silver; high thermal conductivity (>300 W/mK) and low laser absorptivity cause difficulties in thermal initiation and localization of melting or sintering [127, 128].

3.1.2 Alternative AM approaches

A promising alternative class of techniques is vat photopolymerization (VP), which uses light-initiated free radical polymerization to shape parts. Digital light processing (DLP) accomplishes this by projecting 2D images of UV light into a photoresin bath to cure an entire layer of the 3D structure simultaneously. DLP is capable of high volumetric throughputs of up to 100 L/hr with a resolution of ~50 μm, [17, 19] and has found varied commercial applications in the direct manufacturing of shoe soles [129], dental molds [130], and COVID-19 test swabs [131]. Strategies for forming functional materials via VP were discussed in Section 1.3.4; other less common techniques such as direct ink writing (DIW) and material jetting (MJ) use, respectively, extrusion from a nozzle, and controlled deposition of a binder to define part shape. These methods circumvent the challenges of using heat to define part shape but struggle in other ways. Copper materials have been fabricated via DIW [132] and MJ [133], but neither of these techniques have been able to fabricate copper parts with feature sizes under 100 μm. These methods, like prior VP methods, require re-optimization based on the desired precursor; DIW requires tuning ink compositions to achieve a shear-thinning character, and MJ is sensitive to initial powder characteristics.

3.2 Hydrogel infusion additive manufacturing overview

We developed a VP-based AM technique, coined hydrogel infusion additive manufacturing (HIAM), which enables fabrication of a wide range of previously inaccessible microscale metals and alloys from a single photoresin composition and simple post-processing treatments. We use 3D architected hydrogel scaffolds as platforms for subsequent in-situ material synthesis reactions, shown schematically in Figure

3.3a. 3D-sculpted hydrogels are infused with metal precursors, then calcined in air and reduced in forming gas (5 vol% H_2 in N_2) to convert the infused hydrogel scaffolds into miniaturized metal replicas. This approach represents a paradigm shift in VP; the material is selected only after the structure is fabricated. Unlike existing VP strategies, which incorporate target materials or precursors into the photoresin during printing [29, 30, 134], HIAM does not require re-optimization of resins and curing parameters for different materials, enabling quick iteration, compositional tuning, and the ability to fabricate multimaterials. We demonstrate AM of metals with critical dimensions of ~40 μm that are challenging to fabricate using conventional processes. Optical images of each stage in the HIAM process for Cu metal are shown in Figure 3.3b.

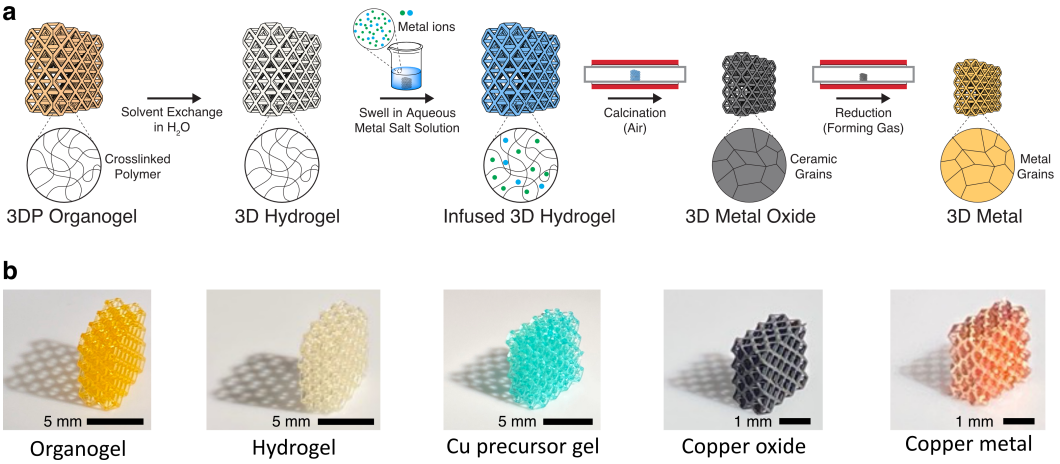

Figure 3.3: **Hydrogel infusion additive manufacturing schematic. a,** A 3D-printed organogel is converted to a hydrogel after solvent exchange in water, then infused with aqueous precursors. The infused 3D hydrogel is converted to an oxide after calcination at low pressure in air, and then converted to a metal after reduction in H_2 **b,** HIAM process applied to copper, in which the aqueous precursor is copper nitrate. To fabricate copper, hydrogel structures were soaked in a 2M copper nitrate solution at 70 °C for 24 hours, followed by calcination at 700 °C (50 sccm air flow) and reduction at 900 °C (150 sccm forming gas flow).

3.2.1 Resin design

We designed the photoresin to consist of equal volume fractions of PEGda binder and DMF solvent. We found this composition to be optimal in terms of the mechanical stability of the as-printed part and the amount of free volume within the structure to allow substantial infiltration of metal salts. See Section 3.3 for a discussion of how the resin was optimized. DMF was chosen as a diluent because it has a low vapor pressure, which minimizes solvent evaporation during printing, is miscible with water, which allows for fabrication of DMF-based organogels that undergo solvent exchange to form hydrogels. DMF is also compatible with numerous

photoinitiators and UV blockers. Omnirad 379, Michler's ketone and Sudan I were selected because of their photoactivity at the 405 nm wavelength of the DLP laser and because they are comprised of only carbon, nitrogen, and oxygen atoms. These molecules are converted to CO_2 and N_2 or NOx gases during calcination, in contrast to commonly used phosphine oxide photoinitiators which can form phosphorous oxide impurities during calcination, or water-soluble initiators such as lithium phenyl-2,4,6-trimethylbenzoylphosphinate that are needed in fully aqueous systems such as that of Yee et al. [65], which can retain impurities deriving from alkali metal ions after calcination and reduction. The resin composition used for this work is shown in Table 3.3.

3.2.2 DLP 3D printing of blank organogels

The DLP printing step defines the shape of the final part; the designed octet lattice shape used throughout this work is shown in Figure 3.4. The DLP printing parameters used are reported in Table A.2.

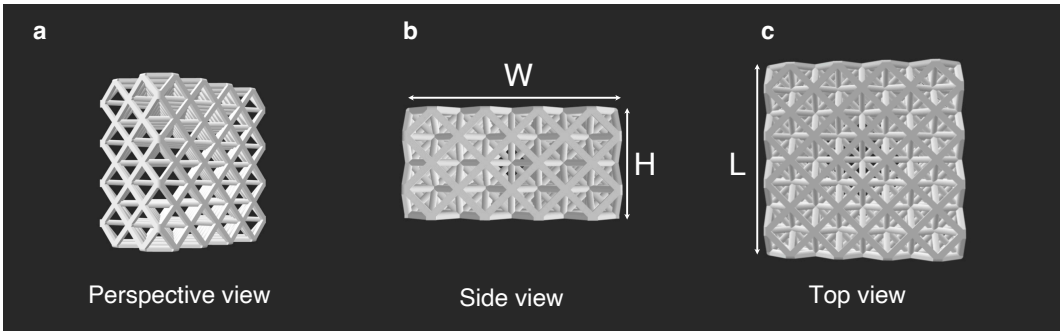

Figure 3.4: **Designed octet lattice structure.** The designed structure has beam of 200 µm, W = L = 6.2 mm, and H = 3.2 mm. Seen from **a**, perspective view, **b**, side view, and **c**, top view.

3.2.3 Hydrogel infusion

After printing, a solvent exchange replaces DMF with water, converting the organogels into hydrogels. The hydrogel structures are then soaked in a metal salt precursor solution to allow metal ions to swell the hydrogel scaffold. Typically, gels were infused for 24 hours on a hot plate at 70 °C.

3.2.4 Thermal treatment

Calcination in air converts the metal salt-swollen hydrogels to metal oxides, and subsequent reduction in forming gas (95% N_2, 5% H_2) yields metal or alloy replicas of the designed architecture. Throughout the process, the part shape, defined during DLP printing, is maintained, with each dimension undergoing ~60-70% linear

shrinkage, with a concomitant ~65-90% mass loss during calcination depending on the constituent materials (see Table A.6 for shrinkage and mass loss several materials).

3.2.5 Chapter summary

The conversion of metal salts within polymer scaffolds to metal oxides and their subsequent reduction to metals and alloys is a general process, requiring only that the target material has water-soluble precursors and that the intermediate oxide formed after calcination can be reduced by hydrogen gas. In this chapter, we restrict our focus to process optimization for copper metal, from which many of the general principles of HIAM can be understood; we delve into the wide array of materials able to be fabricated in Chapter 4.

3.3 Process optimization

An ideal photoresin for hydrogel infusion additive manufactuting is easily printable, mechanically stable, and able to be swollen with aqueous precursor solutions. We used polyethylene glycol diacrylate (PEGda) as a binder, inspired by previous work on aqueous photoresins with metal salts incorporated into the resin [30, 135]. Process development was conducted for both Norrish Type I and Norrish Type II photoinitiators, discussed below.

3.3.1 Early resins: Norrish type I initiation

Initially, we chose Mayzo OB+ as a UV blocker, and TPO-L as a photoinitiator, inspired by the workhorse PR-48 standard clear prototyping resin (see Appendix Table A.1 for PR-48 composition). Finally, we chose dimethylformamide (DMF) as a solvent because it has a low vapor pressure, which minimizes solvent evaporation during printing, is miscible with water, which allows for fabrication of DMF-based organogels that can undergo solvent exchange to form the hydrogels, and is compatible with numerous photoinitiators and UV blockers.

After several (9) iterations of this blank resin, the following formula, known as BL9, was reached, which had excellent printability and mechanical stability, but was kinetically limited during infusion. The components of BL9 are described in Table 3.1. To prepare blank resin (BL9), 359.8 mg OB+ was added to 35 mL DMF in a centrifuge tube, and then mixed on high (~1500 rpm). To get the remaining OB+ to dissolve, the centrifuge tube was placed on a 70 °C hot plate for 30 min, after which all the OB+ had dissolved without further stirring. Then 535.0 mg TPO-L

was added as a liquid to the centrifuge tube and vortex mixed for 5 min to combine. Finally, the contents of the centrifuge tube were poured into a glass jar containing 120g PEGDA 575. The low viscosity DMF solution was easily incorporated into the PEGDA 575 by swirling the glass jar.

Component	**Purpose**	**Amount**
N,N-dimethylformamide (DMF)	Diluent	35 mL
Poly(ethylene glycol) diacrylate $M_n \simeq 575$ (PEGda)	Binder	120 mL
TPO-L	Photoinitiator	535.0 mg
Mayzo OB+	UV blocker	359.8 mg

Table 3.1: Organogel blank resin BL9 components.

3.3.1.1 3D Printing

Architected blank organogel structured were fabricated via digital light processing (DLP) stereolithography in a commercial 3D printer (Autodesk Ember). Approximately 100 mL of blank resin was used per print. The structures as designed were octet lattices consisting of a 4 x 4 x 2 array of unit cells, with beam diameters ranging from 250 μm to 500 μm. The overall part dimensions of the 500 μm beam diameter parts were designed to be able to fit inside of a 20 mL scintillation vial during swelling. The exposure parameters varied slightly with resin composition and tray age (due to PDMS window clouding), but were ~4.25 sec per layer. For all prints, slow approach/separation slide rotation of 0.5 rpm on the first layer and 1 rpm on subsequent layers was used to minimize shear forces on the delicate organogel structures. After printing, organogel structures were rinsed with IPA while still adhered to the build head, then carefully detached using a razor blade inclined nearly parallel to the build head surface. Some organogel structures were further rinsed in IPA for a total of ~15 minutes. After rinsing, organogel structures were dried and massed.

3.3.1.2 Infusion

Organogel structures were added to aqueous salt solutions of varying concentrations. The structures were swelled at 25 °C, 40 °C, or 70 °C for varying durations. After swelling, excess water in the pores of the structures was removed by blowing nitrogen gas. The structures were then massed.

3.3.1.3 Thermal treatment

The swelled organogel structures were calcined in a tube furnace (MTI OTF-1500X) in a dedicated quartz tube. During calcination, compressed air was flowed through the tube at a flow rate of 50 sccm while a vacuum pump evacuated the tube. The equilibrium pressure of air in the tube was ~8 Torr. During reduction, forming gas (95% N_2, 5% H_2) was flowed at 100 sccm. Temperature profiles are provided in Table 3.2. The temperature profile for the 250 µm beam diameter (BD) samples was slightly modified to speed up the furnace run, but shares many of the same characteristics as the 400 µm BD profile.

Calcination (400 µm BD)	**Calcination (250 µm BD)**	**Reduction (both)**
.25 °C/min to 500 °C	.25 °C/min to 400 °C	3 °C/min to 900 °C
1 °C/min to 700 °C	1 °C/min to 700 °C	3 hour isothermal
5 hour isothermal	3 hour isothermal	3 °C/min to room temp.
1 °C/min to room temp.	2 °C/min to room temp.	

Table 3.2: Heating profiles for infused BL9 gels.

3.3.1.4 Characterization

Lattices were imaged using an SEM (FEI Versa 3D DualBeam). Cross sections of the lattices were milled using a gallium focused ion beam (FIB) at an accelerating voltage of 30 kV and 50 nA current, while cleaning of the cross sections was done via FIB at 16 kV and 25 nA current.

3.3.1.5 Kinetic study of infusion in BL9 gels

A swelling experiment was conducted to understand the effect of swelling solution concentration on final structure morphology in BL9 gels. Blank octet lattices with beam diameters of 250 µm or 400 µm were swelled with aqueous copper nitrate solutions of varying concentrations from 1M to 5M. All samples were swelled at 70 °C, and the 250 µm samples were swelled for 36 hours while the 400 µm samples were swelled for 24 hours. Swelling organogel structures in higher concentration salt solutions tended to produce swelled structures that were darker in color, as well as slightly larger. A representative series from 1M to 5M for 400 µm BD is shown in Fig 3.5.

The swelling ratios of the BL9 structures as a function of swelling concentration is reported in Fig 3.6. The consistently lower swelling ratios for the 400 µm lattices

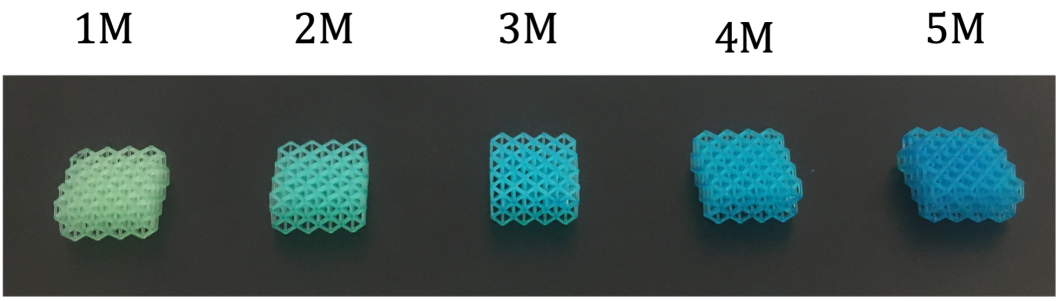

Figure 3.5: **Concentration series for BL9 gels infused with copper nitrate.** Post-swelling concentration series for 400 µm BD octet lattices, swelled at 70 °C for 24 hours.

indicate a diffusion limitation in the 400 µm lattices compared to the 250 µm lattices. This result is consistent with thinner beams in the 250 µm lattice, as well as the fact that the 250 µm lattices were swelled for a 50% longer duration. A characteristic swelling time τ is given by $\tau = L^2/D$ where L is a characteristic length and D is the diffusivity. With this understanding, $\tau_{400}/\tau_{250} = 2.56$, so we should expect that the swelling ratios would be equal if the 400 µm BD lattices were allowed to swell for 2.56x the amount of time as the 250 µm lattices. While this is not a particularly unusual finding, it does contradict an assumption we had made that 24hr would lead to equilibration of the swelled structures. Instead, this analysis implies that the systems may not have equilibrated even after 24+ hours. This finding also has implications on the morphological results which will be discussed in the next section.

3.3.1.6 Morphology of reduced BL9 gels

After swelled organogel lattices were calcined and reduced, they were imaged in the SEM. FIB/SEM was used to investigate the porosity of the nodes and beams by creating a notch in the center of a node. The results of FIB milling the nodes for several copper lattices that were printed with 400 µm BD are presented in Fig 3.7.

It is clear from these images that all of the nodes have a large pore in the center or could simply be considered as shell structures. The shell thickness ranges from a few microns to 10s of microns and seems to reach a maximum somewhere between 2M and 3M swelling concentration. These large voids are not likely the result of gas formation during the combustion process. In the previous section, it was shown that the 400 µm BD samples were likely diffusion-limited during swelling. If the copper nitrate precursor was unable to fully diffuse to the center of the nodes, voids would form there. This seems plausible given that at nodes there is much less access

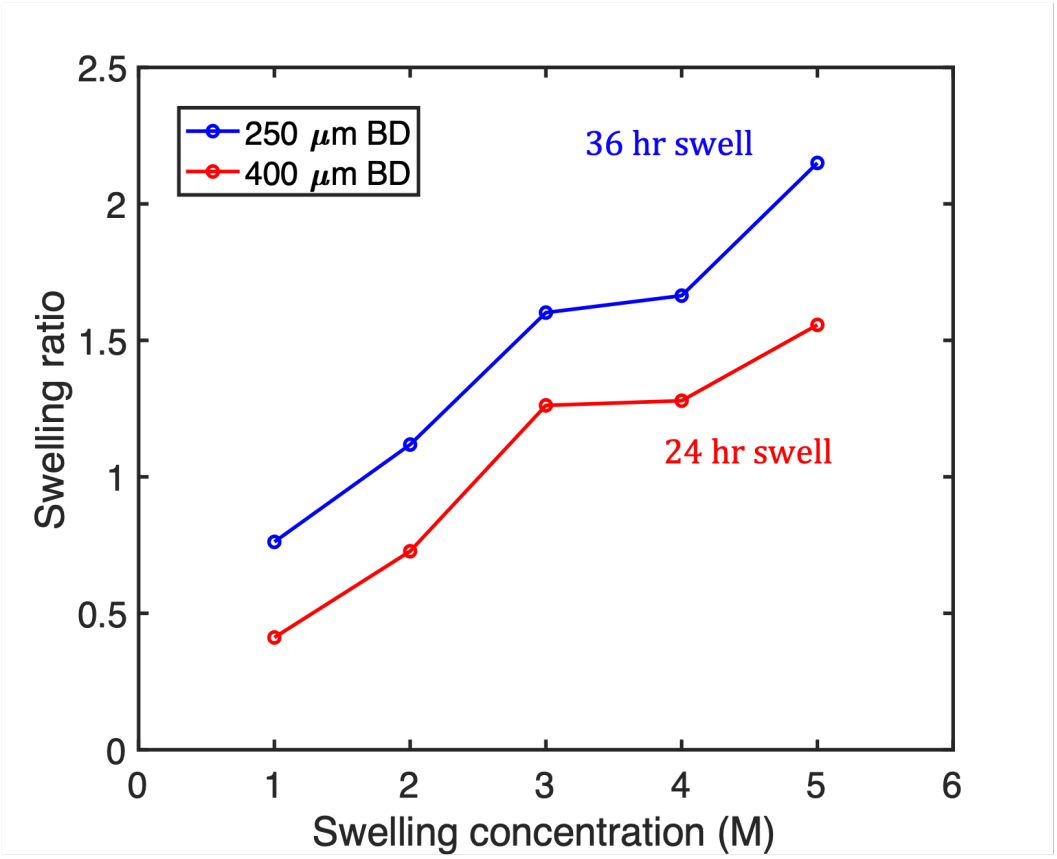

Figure 3.6: **Swelling ratios for BL9 gels infused with copper nitrate.** The 36 hr infusion into a structure with a smaller beam diameter has conisistently higher swelling ratios than the 24 hr infusion, suggesting a diffusion limitation in the 400 μm BD system.

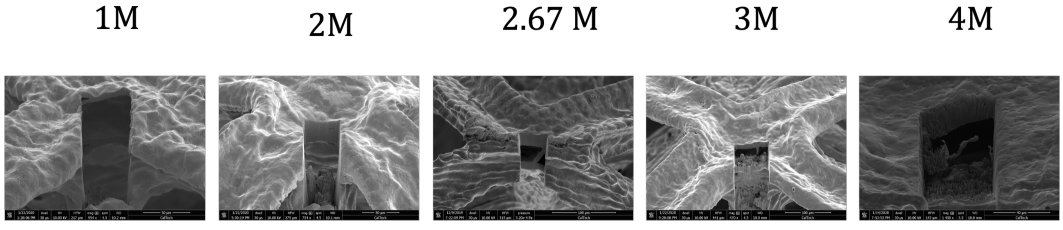

Figure 3.7: **FIB cross-sections of BL9 copper lattices.** Reduced copper lattices from concentration series for 400 μm BD octet lattices. All swelled at 70 °C for 24 hr.

to solution compared to at beams. Another factor that could contribute to the void formation is the degree of shrinkage of the organogel sample during calcination and reduction. It was observed that the samples swelled at lower concentrations (1M-2M) tended to shrink more, while samples swelled at higher concentrations (3M-5M) were roughly similarly sized. One hypothesis regarding the void formation is that during calcination the samples shrink until the resulting copper oxide forms a percolating network that is mechanically robust enough to support itself. Lower concentration samples may take longer to form this percolating network and therefore densify further. Further experiments would be needed to confirm this hypothesis.

In an attempt to reduce the size of the voids at nodes, new samples were printed with beam diameters of 250 µm and swelled with concentrations from 1M to 5M in copper nitrate solution. As discussed earlier, these samples were less diffusion-limited than the 400 µm samples, although it was not confirmed whether they were fully equilibrated during swelling. The morphology of the 2M sample is presented in Figure 3.8.

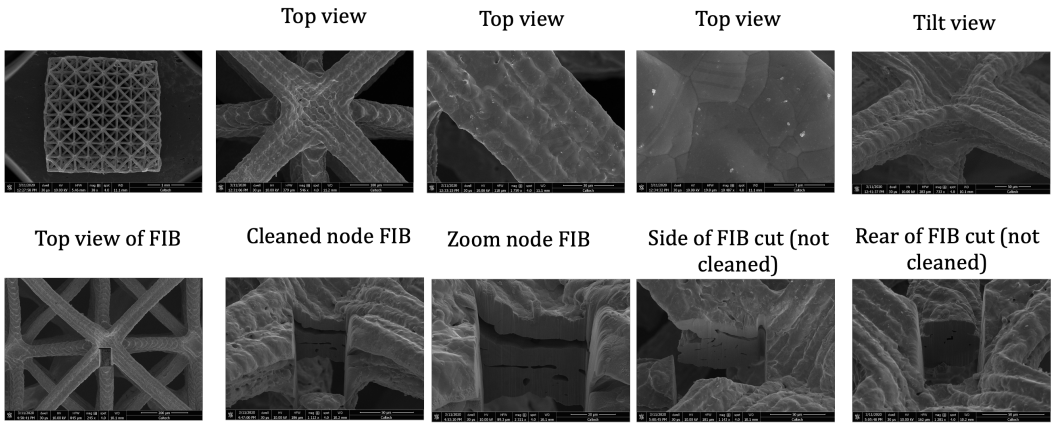

Figure 3.8: **FIB cross-sections of 250 µm BL9 copper lattice.** Reduced copper lattice swelled at 2M from 250 µm BD octet lattice series, swelled at 70 °C for 36 hr.

The reduced 250 µm sample has beams with <100 µm diameter, and is much denser within the nodes, with only a few small pores. Interestingly, there is a large horizontal pore that could be a result of the collapse of the top surface of the node.

3.3.2 Norrish type II initiation resins

A second iteration of resins were designed that relied on Norrish type II initiation. Omnirad 379, Michler's ketone and Sudan I were selected because of their photoactivity at the 405 nm wavelength of the DLP laser and because they are comprised of only carbon, nitrogen, and oxygen atoms. These molecules are converted to CO_2 and

N_2 or NO_x gases during calcination, in contrast to commonly used phosphine oxide photoinitiators which can form phosphorous oxide impurities during calcination.

We designed the photoresin to consist of equal volume fractions of PEGda binder, and DMF solvent. We found this composition to be optimal in terms of the mechanical stability of the as-printed part and the amount of free volume within the structure to allow substantial infiltration of metal salts.

The ultimate composition of the blank resin (lovingly known as 'BL50'–our blank resin with 50% solvent) is shown in Table 3.3. The component amounts shown here are scaled to create ~70 mL resin, the minimum amount needed to print on the Autodesk Ember 3D printer.

Component	**Purpose**	**Amount**
N,N-dimethylformamide (DMF)	Diluent	35 mL
Poly(ethylene glycol) diacrylate Mn~= 575 (PEGda)	Binder	35 mL
2-dimethylamino-2-(4-methyl-benzyl)-1-(4-morpholin-4-yl-phenyl)-butan-1-one (Irgacure 379)	Photoinitiator	347 mg
bis[4-(dimethylamino)phenyl]methanone (Michler's Ketone)	Sensitizer	229 mg
1-(phenyldiazenyl)naphthalen-2-ol (Sudan I)	UV blocker	10.3 mg

Table 3.3: Organogel blank resin BL50 components.

3.3.2.1 Resin preparation

28 mL N,N-dimethylformamide (DMF; Sigma Aldrich, >99.9%) was mixed with 35 mL poly(ethylene glycol diacrylate) Mn = 575 (PEGda; Sigma-Aldrich). Separately, 347 mg 2-dimethylamino-2-(4-methyl-benzyl)-1-(4-morpholin-4-yl-phenyl)-butan-1-one (Irgacure 379; iGM Resins), 229 mg bis[4-(dimethylamino)phenyl]methanone (Michler's ketone; Sigma-Aldrich) and 10.3 mg 1-(phenyldiazenyl)naphthalen-2-ol (Sudan I; Sigma-Aldrich) was stirred into 7mL of DMF. This solution was then added to the DMF/PEGda mixture and swirled until completely homogenous.

3.3.3 3D printing and post-processing

The resin was formed into 3D organogel structures using a commercial 405 nm wavelength DLP 3D printer (Autodesk Ember). Lattice structures were designed consisting of octet lattices with 200 μm beam diameter and 1.5 mm unit cell size (see Figure 3.4). The specific octet lattice geometry was chosen because these

lattices are known to be stiff, with deformation arising from stretching-dominated mechanisms [136]. This allows the printed gel structures to retain their shape during printing better than for bending-dominated structures, which is helpful for printing soft organogel structures. Additionally, at the edges of the structure, the octet unit cell is terminated halfway through the unit cell to remove the presence of sharp features at the part corners, which are easily damaged during post-processing.

3.3.3.1 Printing

Parameter	Setting
UV wavelength	405 nm
Layer thickness	50 µm
Exposure time	6.5s – 7.5s*
Tray rotation speed	0.5 – 1.5 rpm#

Table 3.4: BL50 DLP printing and post-processing parameters.
*Exposure times varied slightly based on the age of the PDMS window through which UV light is projected, and the age of the photoresin.
#0.5 rpm for first layer to ensure good build plate adhesion, 1.5 rpm for the rest of the model layers.

3.3.3.2 Washes

After printing, the organogel lattices are yellow in color due to the presence of the UV blocker Sudan I. To remove unreacted photoresin components, each 3D printed organogel structure was soaked in DMF for 1 hr on a hot plate at 70 °C. After the first DMF rinse, the DMF was decanted, and organogel was soaked again in fresh DMF for 1 hr at 70 °C. After this process, the lattice appeared clear. Subsequently, each organogel structure was soaked in deionized (DI) water for 1 hr at 70 °C, followed by a second soak in fresh DI water for 1 hr at 70 °C to convert the structures from organogel lattices to hydrogel lattices. The solvent exchange step is needed to remove residual DMF in the structure, which can lead to formation of porosity upon calcination and reduction (see Figure 3.9). The presence of DMF can also cause precipitation of the metal salt during the swelling process, leading to an inhomogeneous distribution of the metal precursors.

3.3.3.3 Infusion and post-processing

After washing, hydrogel lattices were dabbed dry (to remove water trapped in pores), but were not fully dried (water remained in the hydrogel structure). The hydrogel lattices were then infused with a 2M solution of copper nitrate for 24 hours at 70 °C.

During calcination, a slow ramp rate of 0.25 °C/min was applied up to 700 °C with a 3 hour isothermal hold, with vacuum being pulled and a 50 sccm air flow. During reduction, the ramp rate was 3 °C/min up to 900 °C with a 6 hour isothermal hold, with 150 sccm of forming gas flowing and vacuum being pulled.

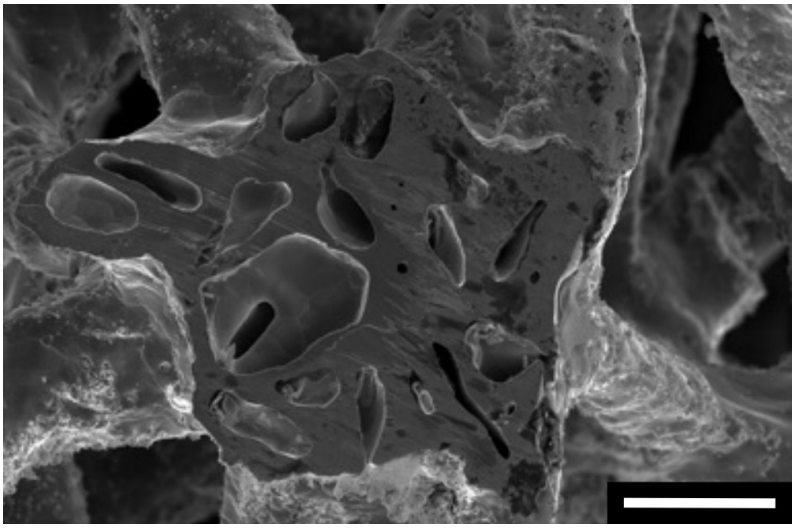

Figure 3.9: **Porosity in copper structure when H_2O solvent exchange step is omitted.** Sample was calcined at 700 °C using .5 °C/min heating rate, reduced at 900 °C with 3 °C/min heating rate. Scale bar: 50 μm.

3.4 Characterization of HIAM-derived copper

Once the HIAM process was optimized, we were able to reliably fabricate copper microlattices. This section focuses on the characterization of those copper microlattices. We sought a complete understanding of both the HIAM process and the materials it can produce via structural, chemical, morphological, microstructural, and mechanical characterization.

3.4.1 Structural characterization

The external and internal morphology of the metal microlattices were investigated by scanning electron microscopy (SEM; FEI Versa 3D DualBeam) at an accelerating voltage of 10-20 kV. Gallium focused ion beam (FIB) milling was performed in the same instrument to mill lattice cross-sections using an accelerating voltage of 30 kV and a current of 50 nA. FIB cleaning of the cross-sections was performed using an accelerating voltage of 16 kV and a current of 25 nA.

SEM imaging reveals that Cu samples maintained their octet lattice shape during thermal treatment, with beam diameters of ~40 μm. Using the FIB to mill out representative cross-sections in the lattice nodes, we observed that these materials

were dense and relatively defect-free. The Cu showed a few < 5 µm-diameter pores and a lamellar crack (Figure 3.10d).

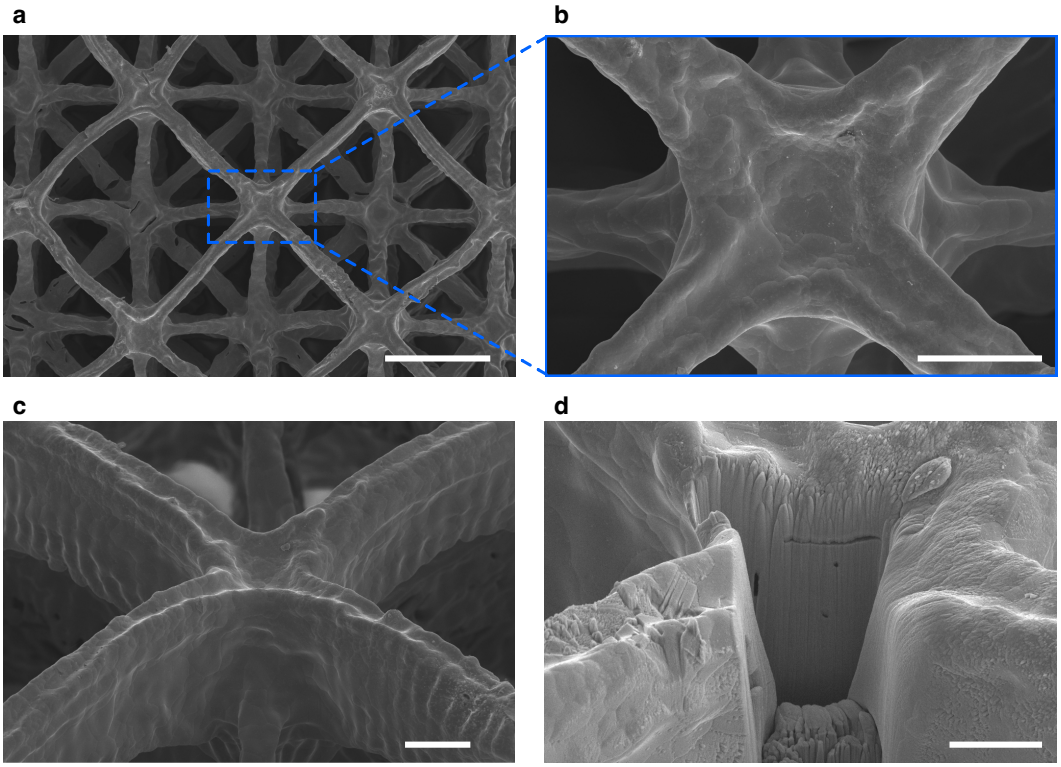

Figure 3.10: **Morphology of Cu microlattice.** SEM images of Cu lattice showing **a,** multiple unit cells (top view), **b,** a single node (top view), **c,** a single node (52 °tilt view), **d,** FIB-milled cross-section showing the internal structure of a node (52 °tilt view). Scale bars: **a,** 200 µm; **b,c,** 50 µm; **d,** 25 µm.

3.4.2 Grain size analysis

To analyze the distribution of grain sizes present in HIAM-derived copper, grain boundaries were identified visually, and traced (see Figure 3.11).

The traced grain boundaries were then analyzed in ImageJ via the following procedure:

1. Set scale based on horizontal field width (HFW).
2. Invert image to create dark background.
3. Make binary.
4. 'Analyze particles' command.

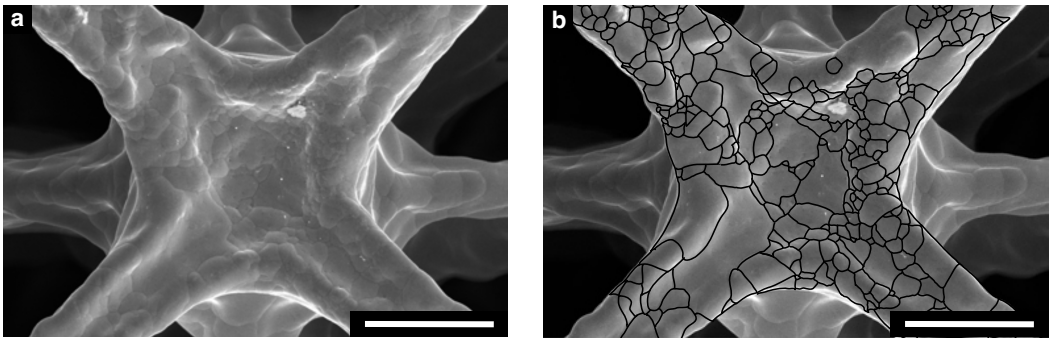

Figure 3.11: **Copper microlattice with traced grains. a,** SEM image of Cu lattice and **b,** grain boundaries identified on Cu lattice from **a**. Scale bars: **a,b,** 50 µm.

When using the Analyze Particles command in ImageJ [137], all enclosed regions were considered a grain. Grains that terminated on an edge were not considered in the analysis. Since real grains grains are not circular, grain diameter is reported as the diameter of a circle with the same area as the grain: $d = (\frac{4A}{\pi})^{1/2}$.

The grain size analysis results for copper are reported in histograms in Figure 3.12. HIAM-derived Cu has an area-weighted average grain size of 13.74 ± 8.43 µm (n = 246).

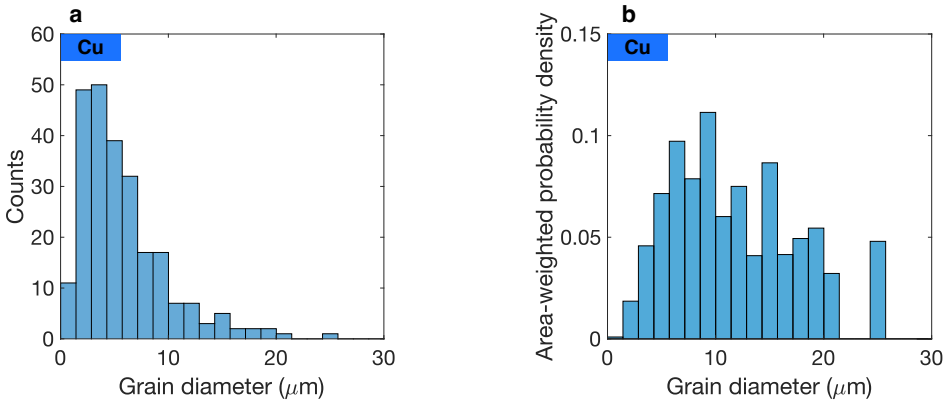

Figure 3.12: **Grain size distribution for HIAM-derived Cu. a,** Grain size distribution for Cu and **b,** area-weighted probability density for Cu grain sizes.

3.4.2.1 Electron backscatter diffraction analysis

With the z-direction and build direction aligned, metal lattice samples were loaded into an Oxford EBSD System in a Zeiss11550VP SEM and are imaged using a 120 µm aperture at 20 kV. Data analysis for the Kikuchi maps was done in AztechHKL software. All maps display the inverse pole figure in the z-direction.

3.4.3 Chemical characterization

We investigated the chemical composition of the metal microlattices using X-ray diffraction (XRD), energy dispersive X-ray spectroscopy (EDS), thermogravimetric analysis (TGA), and differential scanning calorimetry (DSC) to understand the chemical and microstructural evolution of these materials during calcination and reduction.

3.4.3.1 EDS analysis

Elemental analysis was performed in the FEI Versa 3D DualBeam SEM using energy-dispersive X-ray spectroscopy (EDS; Bruker Quantax 200, XFlash 6|60 detector), with an applied voltage of 20 kV. Energy dispersive X-ray spectroscopy (EDS) mapping showed homogenous distribution of Cu in the Cu lattice, as well as the presence of small SiO_2 particles that result from contamination from the quartz furnace tube and/or the mullite boats in which samples are calcined and reduced.

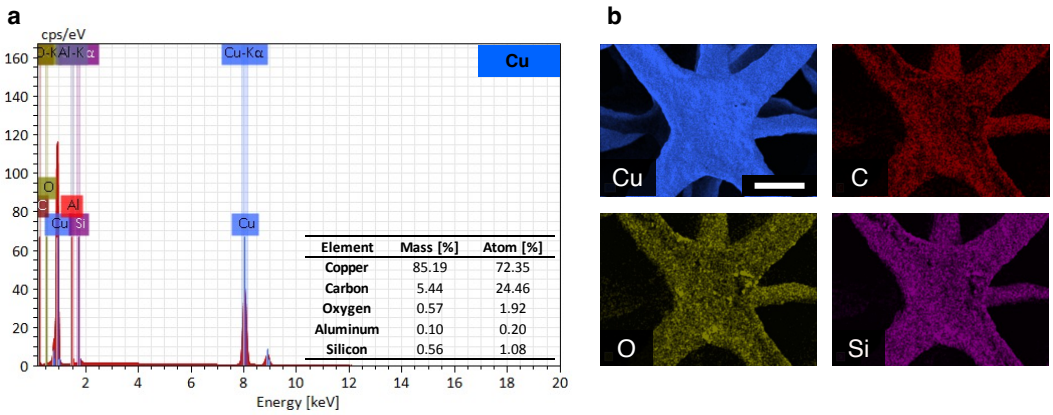

Figure 3.13: **Cu EDS analysis. a,** EDS spectrum with quantification table (inset) and **b,** EDS maps. Scale bar: **b,** 50 µm.

3.4.3.2 XRD analysis

Powder X-ray Diffraction (XRD; PANalytical X'Pert Pro) data was collected using a Cu $K_{\alpha 1}$ source at 45 kV and 40 mA. Samples were either ground into powders or flattened and attached to an amorphous zero-background sample holder using clay prior to XRD analysis.

Calcination of metal nitrate salt-containing gels in air (700 °C, 50 sccm) produces metal oxide replicas of the architectures. After calcination of a Cu precursor gel, the XRD pattern of the resulting material matches the pattern of monoclinic CuO

(Figure 3.14a). After reduction of the oxide material in forming gas (700 °C, 150 sccm), the XRD pattern of the resulting material matches the pattern of face centered cubic Cu metal. Notably, no remaining oxide phase is detected via XRD analysis, suggesting full conversion of CuO to Cu during the reduction step. We observe peak splitting attributed to $K_{\alpha 1/2}$ splitting in the reflection at 2Θ = 74°, which characteristically becomes exacerbated at high diffraction angles.

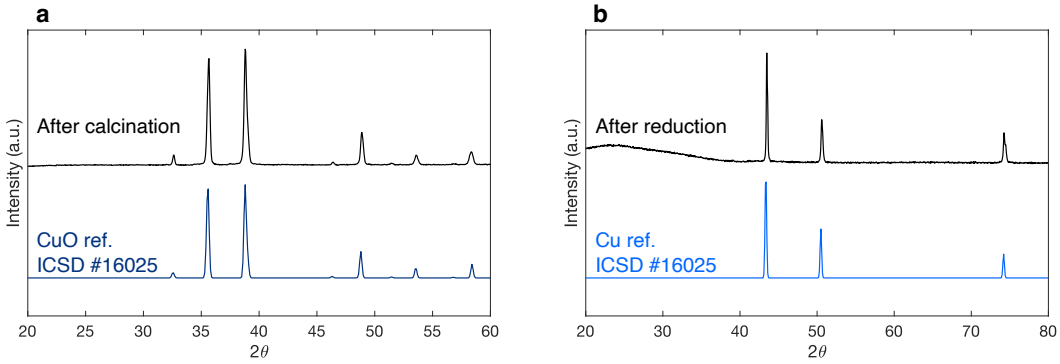

Figure 3.14: **Cu XRD analysis.** XRD patterns for **a,** calcined Cu gel showing presence of CuO, and **b,** reduced sample showing conversion of CuO to Cu.

3.4.3.3 Thermal analysis: TGA & DSC

Thermogravimetric analysis (TGA; TA Instruments TGA 550A) was performed by heating samples to 700 °C at a rate of 1 °C/min in an air flow of 25 mL/min while the mass of the sample was continuously measured. Differential scanning calorimetry (DSC; TA Instruments DSC 25) was performed by heating samples to 700 °C at a rate of 1 °C/min in an air flow of 25 mL/min while heat flow to the sample was continuously measured.

The results of these expermiments are shown in Figure 3.15. The Cu and precursor gel retains 12.7% of the original mass, reaching completion between 370 °C and 380 °C, indicated by mass stabilization at full conversion. The derivative of sample weight with respect to temperature, dW/dT, shows the region of highest mass loss rate of 1 wt.%/°C that occurs at 353 °C. Figure 3.15b contains the DSC profile of a Cu precursor gel heated in air at 1 °C/min. An exothermic event begins at 235 °C, reaching a maximum heat flow of -1.5 W/g at 308 °C.

3.4.3.4 Measuring carbon content via EDS and TEM

Quantifying trace amounts of carbon in metals is difficult. Notably, EDS struggles to quantify light elements, and often requires high accelerating voltages (a rule of

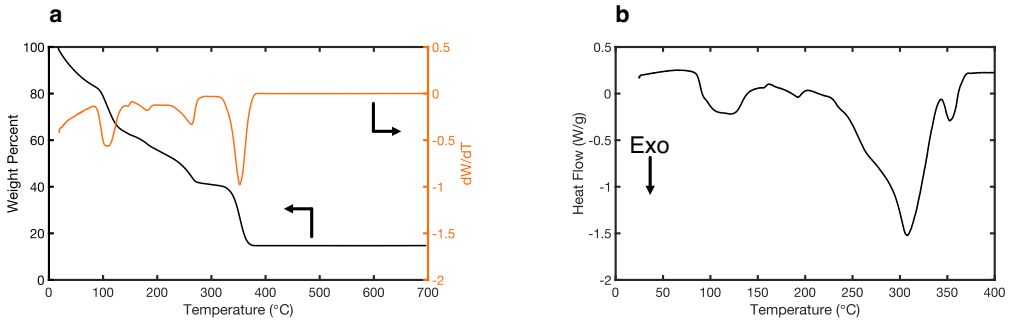

Figure 3.15: **Cu thermal analysis. a,** TGA data for calcination of Cu gel at 1 °C/min in air to 700 °C. **b,** DSC data showing heat transfer from Cu gel during calcination at 1 °C/min in air, showing a significant exothermic event around 300 °C.

thumb is 2x the energy of the probed transition). With the understanding that a quantitative analysis on C content via EDS will never be exact due to 1) the presence of adventitious carbon and 2) the inability for EDS to quantify light elements well, we aimed to investigate whether any carbon remained from un-combusted PEGda. To do so, we combined results from SEM EDS at high and low accelerating voltages, as well as TEM EDS.

We compared the EDS spectra of HI-derived $Cu_{50}Ni_{50}$ using accelerating voltages of both 20 kV and 5 kV (see Figure A.5). The comparison shows that high accelerating voltage is needed to excite Kα X-rays in Cu and Ni (and achieve accurate quantification of Cu and Ni), but that at high voltage, the C peaks are obscured in the spectrum, leading to difficulty in quantifying C. At lower accelerating voltage, quantification shows 1.69 wt% C, which may be due to adventitious carbon. Ultimately, higher resolution techniques were needed to fully investigate the presence of carbon in these materials. We performed TEM analysis, including EDS, on HI-derived Cu (see Figures 3.17 and 3.18). The TEM analysis does not show any obvious amorphous regions indicative of remaining carbon, and EDS mapping at high resolution shows that the largest source of carbon is also the aluminosilicate inclusions, a result of contamination from the furnace tube.

3.4.4 Microstructural and mechanical characterization

For the processing conditions reported here, HI-derived copper is microcrystalline, with randomly oriented micro-grains that are densely populated by annealing twins which generally form as the result of crystalline defects during grain growth or grain boundary motion [138]. The presence of micron-scale twinned regions in Cu is seen clearly in Ga^+ ion-channeling images (Figure 3.16a, yellow arrows point to twins) and electron backscatter diffraction (EBSD) maps (Figure 3.16b). The presence

and quantity of annealing twins has implications for the mechanical behavior of HI-derived metals during nanoindentation, discussed further in Section 3.4.4.3.

3.4.4.1 Microstructural characterization

HI-derived materials have high crystallographic twin densities [139], defined as the length of twin boundary per cross-sectional area. Cu has a twin density of ~1.7x10^6 m^{-1} with each grain containing on average 4.8 twin boundaries, and 88% of all grains containing at least one twin boundary. Additional twinning statistics as measured by EBSD are reported in Table A.3.

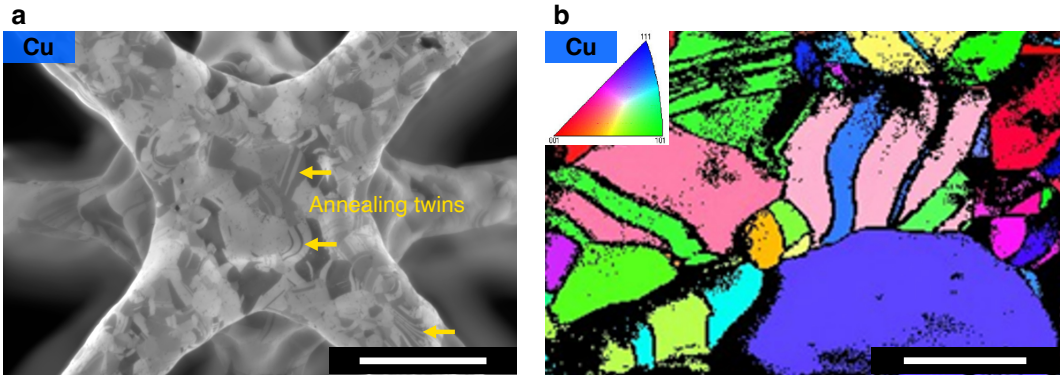

Figure 3.16: **Cu microstructural characterization. a,** Ga+ ion-channeling image and **b,** EBSD maps of Cu show high densities of annealing twins. Cu has a complex micro-grained structure and multiple twinned regions within grains denoted by yellow arrows. Scale bars: **a,** 50 µm; **b,** 20 µm;

3.4.4.2 TEM analysis

Lamellae with thicknesses of <100 nm were prepared for transmission electron microscopy (TEM) using a liftout procedure in an SEM (FEI Versa 3D DualBeam) by Rebecca Gallivan. The top surface of the liftout region was protected with a ~100 nm-thick layer of platinum (Pt) deposited via a gas injection system (GIS), followed by a ~400 nm-thick layer of Ga^+ FIB-deposited Pt in the same chamber. Next, a Ga^+ ion beam was used to carve out trenches into the substrate forming a U-cut to free the ~1 µm-wide metal lamella base from the rest of the substrate. A tungsten needle (EZlift program) was attached to the lamella with FIB-deposited Pt before being cut free of the sample and transferred to a copper halfmoon grid. The lamella was attached to the Cu grid with FIB-deposited Pt and the tungsten needle was cut away to free the sample. After detaching the tungsten needle, a series of FIB cuts with a decreasing Ga^+ voltage/current (30 kV/100 pA; 30 kV/10 pA; 16 kV/23 pA) were used to progressively thin the cross-section of the lamella structure to <100

nm. TEM imaging was performed in a Jeol JEM-2800 TEM with a 200 kV beam with Mingjie Xu at the UC Irvine Materials Research Institute.

TEM analysis of HI-derived Cu (Figure 3.17) shows twins in more detail. We observe that grain boundaries and twin boundaries are well-formed, with no voids at triple junctions, and no observable secondary phases (i.e., unreduced CuO or amorphous carbon) besides the presence of aluminosilicate inclusions (see Figure 3.18 for TEM EDS) that result from contamination from the furnace tube. The inset of Figure 3.17 shows the diffraction pattern corresponding to FCC Cu, along the [311] zone axis.

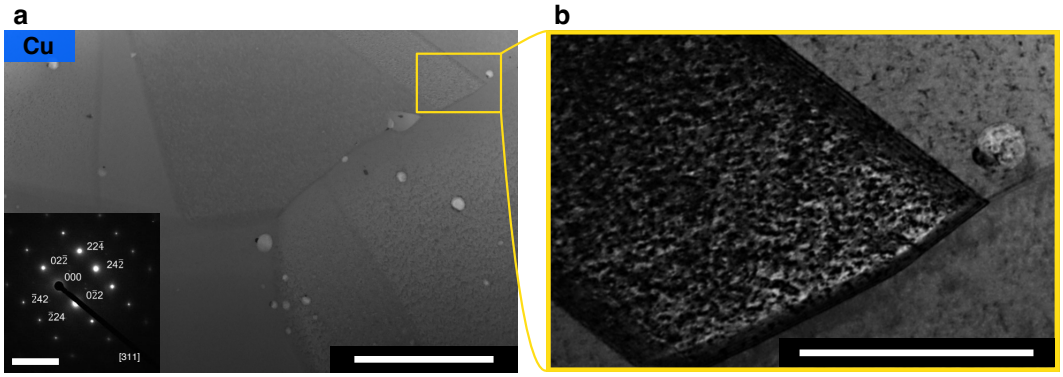

Figure 3.17: **Cu TEM characterization.** **a,** TEM images of HI-derived Cu show well-formed grain boundaries, and some aluminosilicate inclusions. FCC copper is observed from the diffraction pattern in the inset of **a**. **b,** TEM image of a twin boundary and aluminosilicate inclusion. Scale bars: **a,** 2 µm, inset 10 nm^{-1}; **b,** 500 nm.

3.4.4.3 Nanoindentation

Samples were prepared for nanoindentation by mounting them in acrylic (Beuhler SamplKwik) and curing for 12 hours in silicone molds. The samples were polished first with 300 grit until the metal structure was exposed. The samples then were polished with 600 grit, followed by 1200 grit and subsequently a 0.25 µm grit suspension (Beuhler MetaDi Polycrystalline Diamond Slurry). Indentation was performed on an Agilent G200 Nano Indenter with XP module using a Berkovich tip with an area function given by $A = 24.5h^2 + 688h$. Samples were indented at 10^{-3} strain rate to a maximum depth of 1 µm, followed by a 2 second hold and subsequent unloading. Grain sizes were determined via SEM image analysis that consisted of tracing grains on the surface of the sample and using ImageJ to analyze the resulting shapes. These values were corroborated by EBSD mapping analysis of grain size.

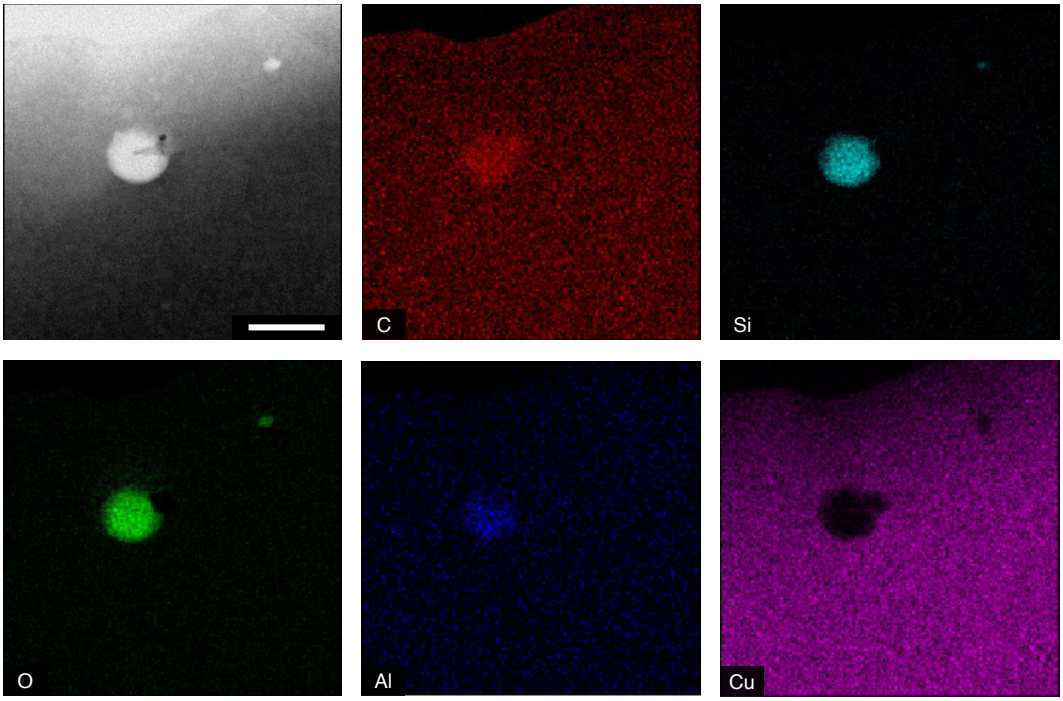

Figure 3.18: **Cu TEM EDS characterization.** TEM EDS analysis shows a 200 nm diameter aluminosilicate inclusion. Scale bar: 250 nm.

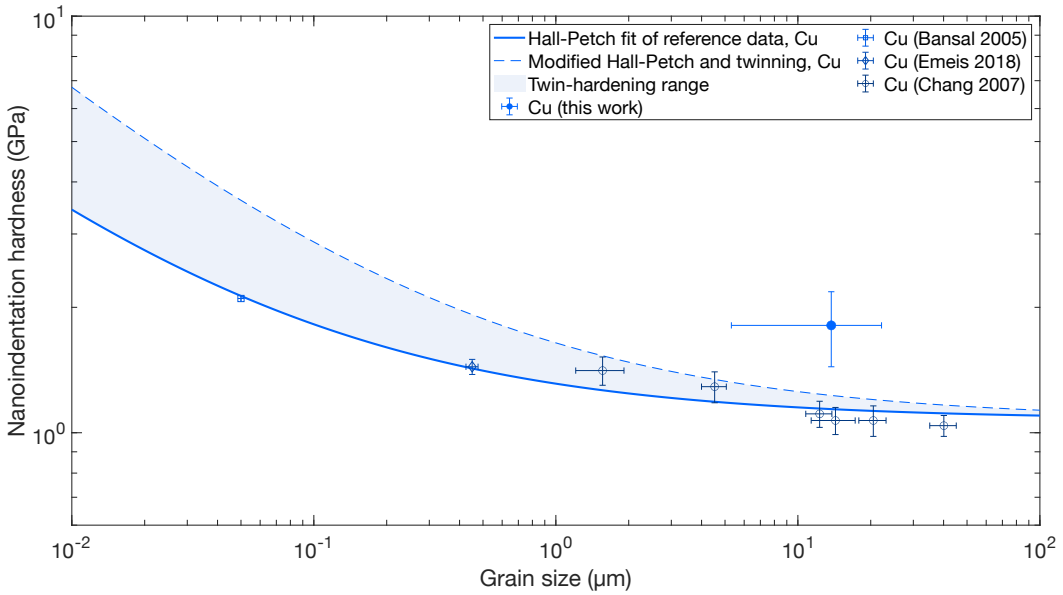

Figure 3.19: **Cu nanoindentation analysis.** Nanoindentation hardness of HI-derived Cu is higher than reference nanoindentation data [140–142] and extrapolated Hall-Petch grain size scaling (dashed lines show correction for effect of twin-induced hardening). Error bars show standard deviations of grain size and nanoindentation hardness, where available. Sample size: Cu hardness, n = 22; Cu grain size, n = 246.

3.5 Hydrogel infusion additive manufacturing summary and outlook

In this chapter, discussed the development of the HIAM technique, and showed how it can be applied to fabricate copper microlattices with high resolution. In the next chapter, we extend our investigation of HIAM to other material systems, and explore alloys and other esoteric materials.

Chapter 4

VERSATILE AM: ADDITIONAL MATERIALS

Chapter Abstract

In the previous chapter, the development of the HIAM process and its optimization for copper metal was described. Here, we show that this method can easily be expanded to make other materials, including other metals, oxides, and alloys.

This chapter has been adapted from:

1. Saccone, M. A.[*†]; Gallivan, R. A.[*]; Narita, K.; Yee, D. W.[†]; Greer, J. R.[†] Microscale fabrication of 3D multicomponent metals via hydrogel infusion. *In review* **2022**. Preprint DOI: 10.21203/rs.3.rs-1108933/v1.

Contributions: M.A.S. conceived and designed the experiments, designed the photoresin, fabricated samples, performed material characterization, and wrote the manuscript.

4.1 Introduction: Hydrogel infusion, beyond copper

Compared to existing techniques which include precursors in the resin or introduce precursors through chemically directed swelling, HIAM enables facile traversing of a much larger compositional space, and significantly reduces the burden on resin design and/or developing conjugation chemistry, which may differ depending on the desired precursor. To demonstrate the versatility of HIAM compared to previous gel-based VP AM techniques [30, 34, 135], we fabricated a variety of materials in addition to copper, including common metals nickel, silver, and alloys thereof (Section 4.2), as well as more esoteric materials such as a CuNiCoFe high entropy alloy and the refractory alloy W-Ni. We also fabricated metallic multimaterials, described in Section 4.6. Additional development was required for these materials; fabrication and characterization of the CuNiCoFe high entropy alloy is described in Section 4.3 and the W-Ni alloy is described in Section 4.4. Multimaterials including Cu/Co and Cu/CuNi multimaterials, are described in Section 4.6. HIAM is also distinguished by its ability to be parallelized, discussed in Section 4.5. Several organogels can be printed simultaneously, swelled in separate solutions, and then calcined/reduced together. This parallelization is impossible with any other form of metal AM and is a direct consequence of the temporal separation of part shaping and material choice.

4.2 More materials: Cu, Ni, Ag, and binary alloys

We fabricated a variety of materials in addition to copper, including common metals nickel, silver, and alloys thereof, all from a single photoresin, using the same processing conditions described in HIAM for Cu in Chapter 3. The branching nature of the fabrication possibilities is shown in Figure 4.1. Additionally, some of the data from the pure copper system will be recapitulated in this section in order to compare the behavior of a pure metal to the behavior of a prototypical alloy (CuNi).

4.2.1 Structural characterization of Cu/Ni/Ag metals

The external and internal morphology of the metal microlattices were investigated by scanning electron microscopy (SEM) and a Ga^+-source focused ion beam (FIB). SEM imaging reveals that all samples maintained their octet lattice shape during thermal treatment (Figures 4.2a-c). Using the FIB to mill out representative cross-sections in the lattice nodes, we observed that two of the pure metals, Ni and Cu, were dense and relatively defect-free, with a few < 5μm-diameter pores and lamellar cracks highlighted by yellow arrows in Figure 4.2d (i, iii). The morphology of the

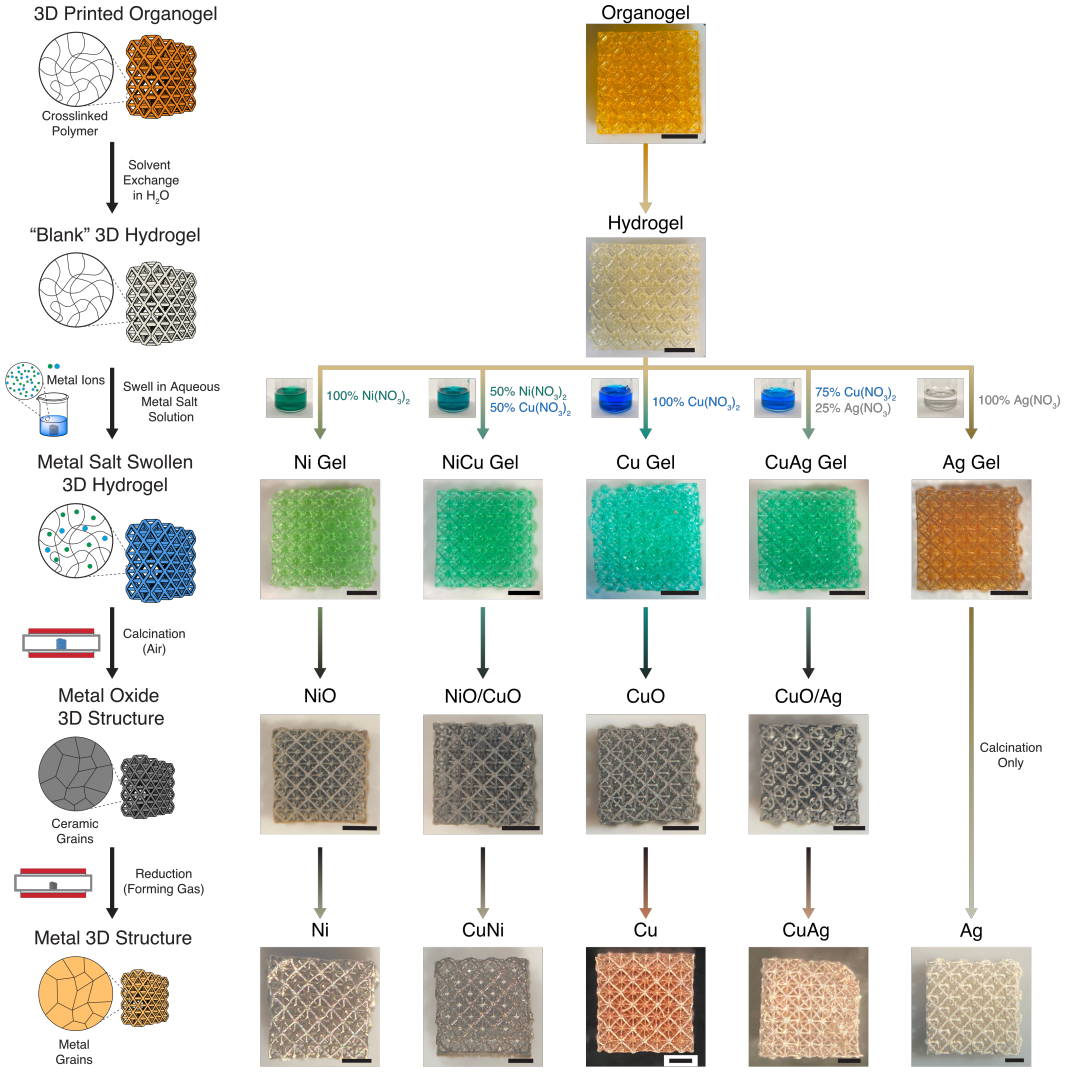

Figure 4.1: **HIAM process for Ni, Cu, Ag, and alloys demonstrates versatility for printing common metals.** **a**, A PEGda-/DMF-based 3D printed organogel structure (chemical components pictured) is converted to a **b**, hydrogel replica after leaching out photoactive compounds and exchanging solvents in water. **c**, Metal salt swollen 3D hydrogels obtained after swelling in 2M salt solutions, indicated by respective arrows, for 24 hours at 70 °C. d, Metal oxide structures formed following the calcination of the metal salt swollen hydrogel structures at 700 °C in air. e, Metal and alloy 3D structures formed by reduction of the CuO, CuO/NiO, and NiO structures at 900 °C and the CuO/Ag structures at 700 °C in forming gas, or directly by calcination for the pure Ag structure. Scale bars: **a-c**, 2 mm; **d**, 1 mm; **e**, 500 µm.

CuNi alloy (Figure 4.2d (ii)) appeared to be dense and contains similar μm-sized spherical pores as pure Cu, with no observed lamellar cracks. The CuAg lattices appeared to be fully dense and phase-segregated into Cu- and Ag-rich domains that can be distinguished by ~5 μm regions of differing contrast in Figure 4.2d (iv) (see elemental maps in Figure 4.10); Ag lattices were porous and contain ~10 μm sized sintered grains adjoined by 1-10 μm-sized voids.

The Cu and CuNi samples contain fewer defects and pores compared with pure Ni and Ag. The presence of defects and pores is correlated with higher maximum dW/dT, quantified by TGA (see Table A.5). During calcination, samples undergo ~60-70% linear shrinkage and ~65-90% mass loss (see Table A.6), which drives kinetic competition between part shrinkage and internal pore formation. These findings indicate that rapid thermal decomposition inhibits global, isotropic part shrinkage and causes the formation of internal voids and pores; controlling and minimizing the rate of mass loss during thermal treatment steps is important for fabricating high quality parts via the HIAM method, consistent with other debinding processes. In practice, this necessitated slow ramping at 0.25 °C/min during calcination, and calcining at low pressure (~6 Torr).

4.2.2 Chemical characterization of Cu/Ni/Ag metals

Additional chemical characterization was performed for the materials pictured in Figure 4.1, discussed in the following sections.

4.2.2.1 EDS analysis

EDS analyses in Figure 4.3 of Cu and CuNi microlattices show that these materials contain, by weight, 93% and 86% of the target materials, respectively. The balance is made up of carbon, which is difficult to accurately quantify and likely includes some adventitious carbon and aluminosilicate contamination from the furnace tubes.

This analysis shows that the atomic ratio of Cu:Ni in our CuNi material is 1.21:1, or a stoichiometric composition of $Cu_{55}Ni_{45}$. The deviation of alloy composition from swelling solution composition is likely due to different affinities of PEGda with the metal ions[143]. However, by adjusting the swelling solutions to account for preferential incorporation of certain ions, target compositions can be achieved with precision. For example, to target a $Cu_{50}Ni_{50}$ alloy, we swelled a hydrogel precursor in a 1:1.21 molar ratio of $Cu(NO_3)_2$:$Ni(NO_3)_2$ at a total metal cation concentration of 2M. After calcination and reduction, EDS analysis (Figure 4.4) showed that the

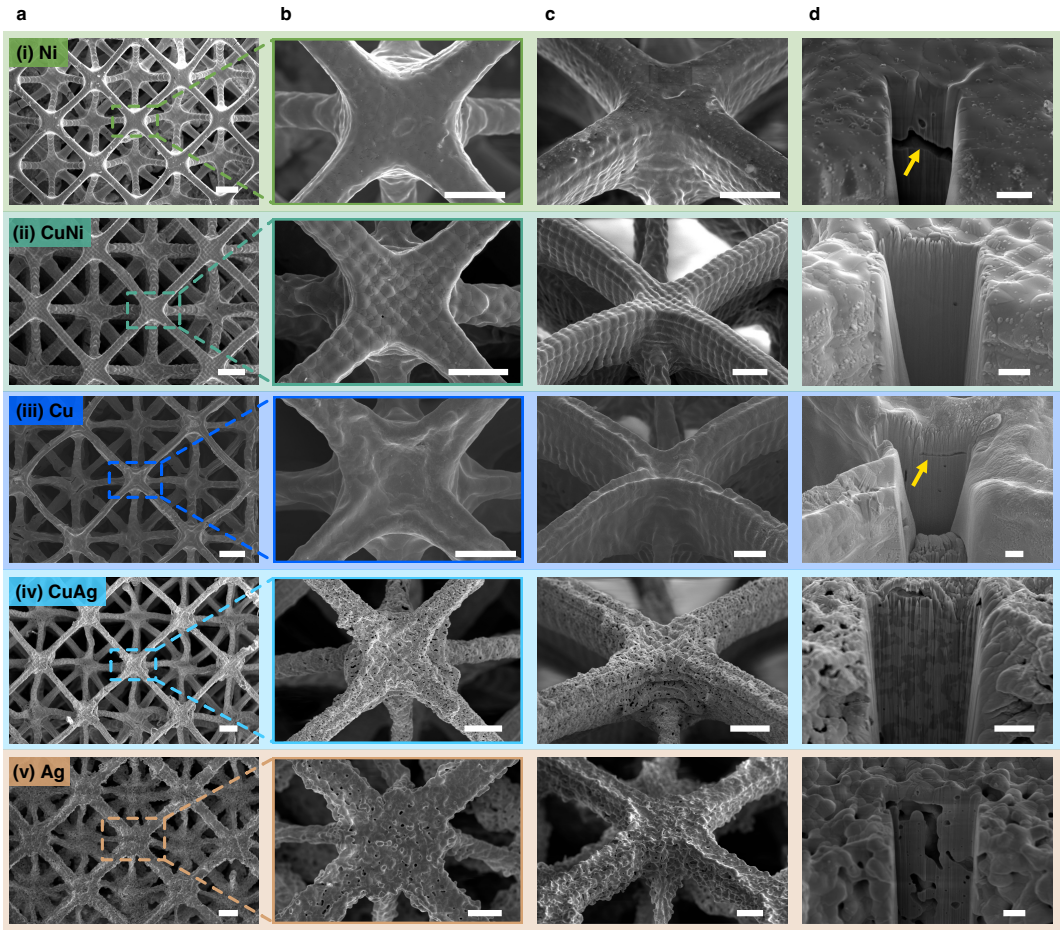

Figure 4.2: **Structural characterization of additional HIAM metal lattices. a-c,** SEM images of metal or alloy octet lattices. Panel a shows multiple unit cells from the top. Panel **b** shows a single node of the octet lattice from the top. Panel **c** shows a single node of the octet lattice from 52°tilt. Panel **d** shows a FIB/SEM cross section of internal node structure from 52°tilt. Yellow arrows point to lamellar pores parallel to surface of node. Scale bars: **a,** 100 µm; **b, c,** 50 µm; **d,** 25 µm.

stoichiometry of this cupronickel alloy (referred to hereafter as $Cu_{50}Ni_{50}$) was within 1% of the target composition, at $Cu_{50.5}Ni_{49.5}$.

4.2.2.2 XRD analysis

The XRD patterns shown in Figure 4.5a (see Figure 4.7 for additional materials' XRD patterns) show that the calcined Cu precursor gel, which contained $Cu(NO_3)_2$, and the CuNi precursor gel, which contained $Cu(NO_3)_2$/$Ni(NO_3)_2$, were fully converted to CuO and CuO/NiO, respectively. Notably, the CuO/NiO XRD pattern shows the presence of the individual NiO and CuO phases in the calcined material. Reduction of these metal oxides in forming gas (900 °C, 150 sccm) converts the CuO and CuO/NiO lattices to Cu and a homogenous CuNi alloy, respectively (Figure 4.5b). While both CuNi and Cu have face centered cubic crystal (FCC) structures, the

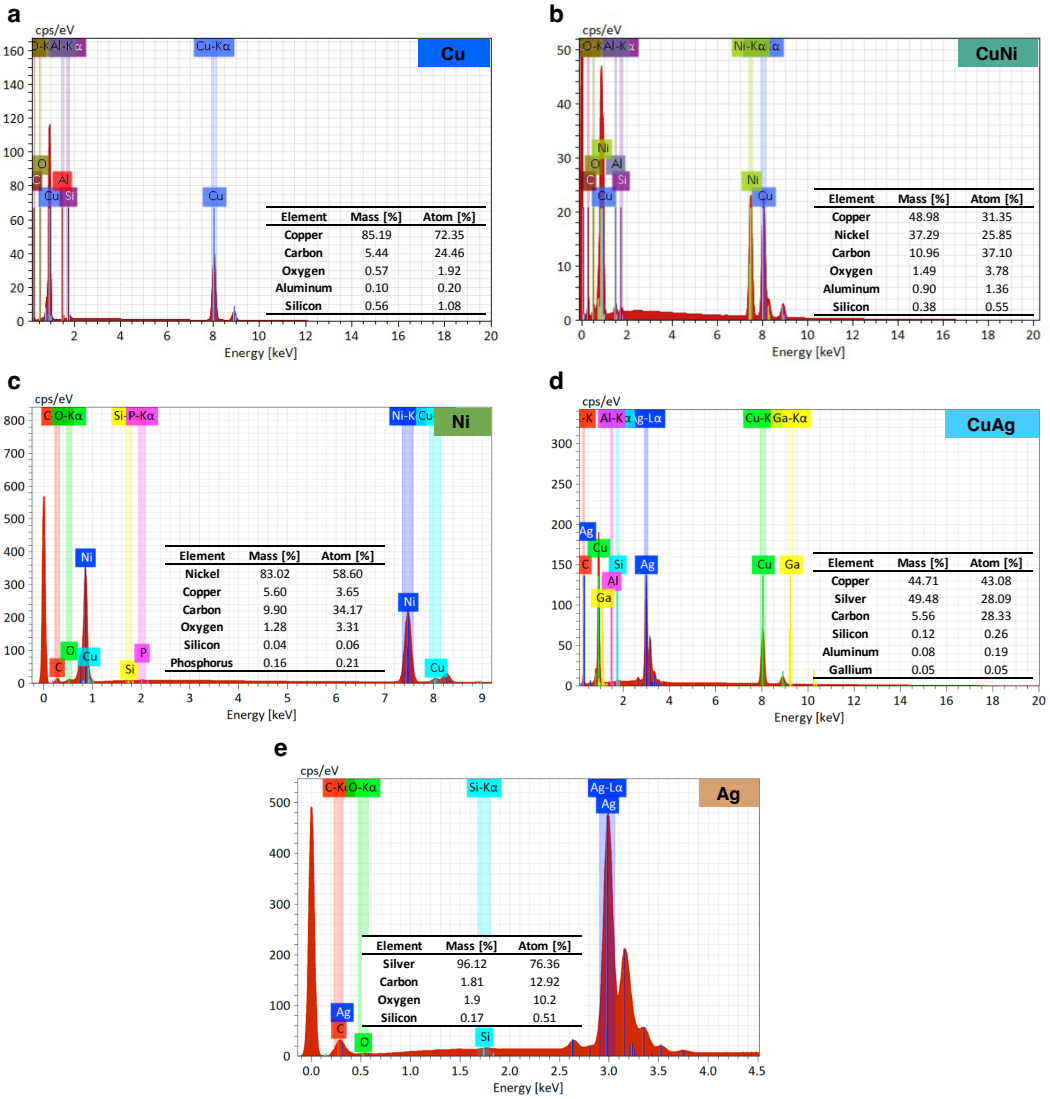

Figure 4.3: **EDS data for Cu/Ni/Ag and alloys.** EDS spectra for the metal microlattices shown in Figure 4.1: **a,** Cu, **b,** CuNi, **c,** Ni, **d,** CuAg, and **e,** Ag. All EDS spectra were collected at the surface of a microlattice, except the CuAg spectrum, which was collected from a Ga^+ ion FIB-milled cross-section, leading to a small Ga signal.

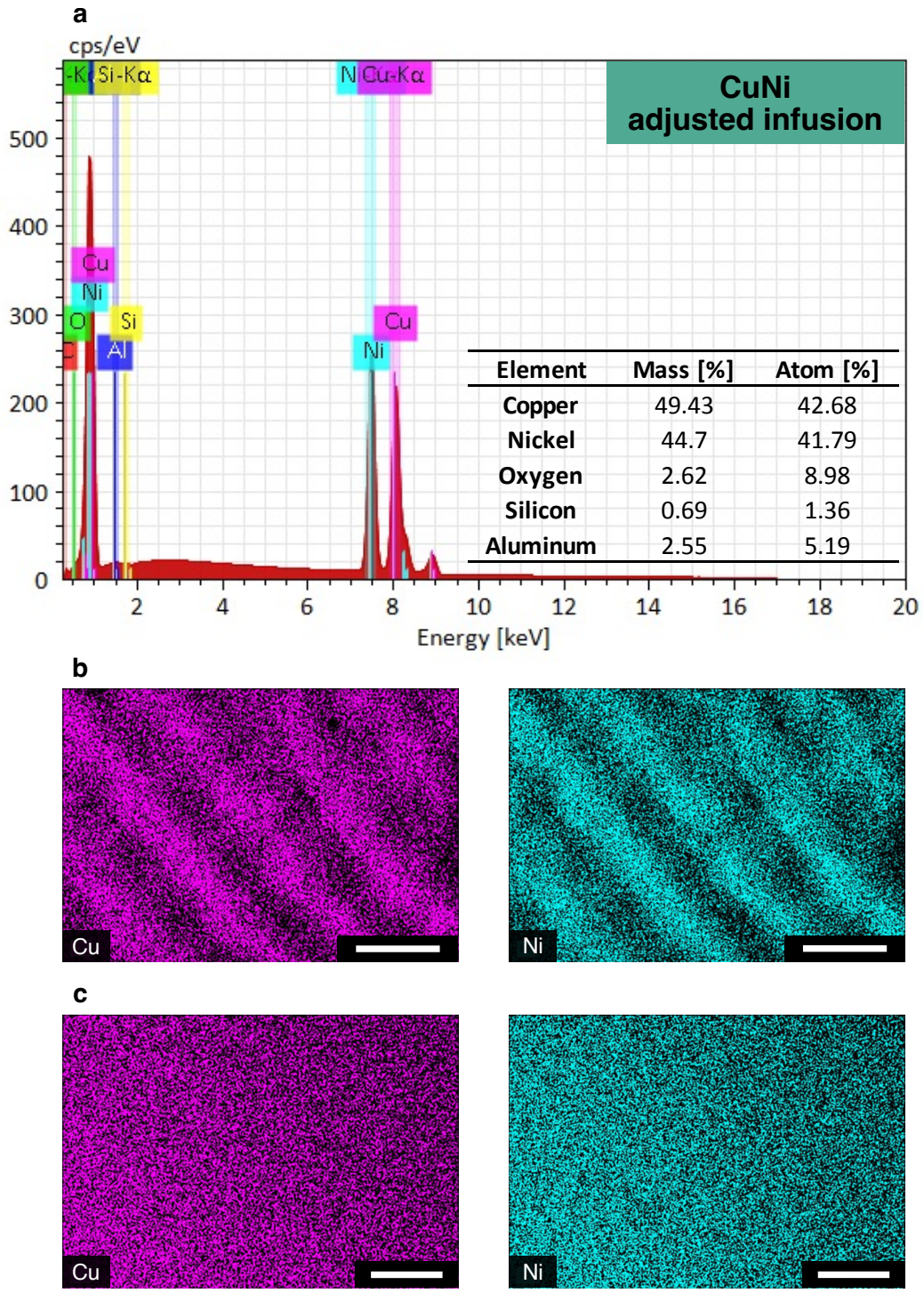

Figure 4.4: **EDS data for $Cu_{50}Ni_{50}$.** After adjusting the infusion step for CuNi, **a,** EDS analysis shows that a CuNi alloy with composition $Cu_{50.5}Ni_{49.5}$ was produced. EDS maps at **b,** 2.9kx magnification and **c,** 50kx magnification show that there is no observable inhomogeneity at any scale in the distribution of Cu and Ni. The variations in intensity in the EDS maps at lower magnification in b are a result of surface morphology. Scale bars: **b,** 10 µm; **c,** 500 nm.

single set of FCC reflections in the CuNi pattern shift to higher diffraction angles, a result of decreased lattice spacing due to the incorporation of the smaller Ni atom into the structure.

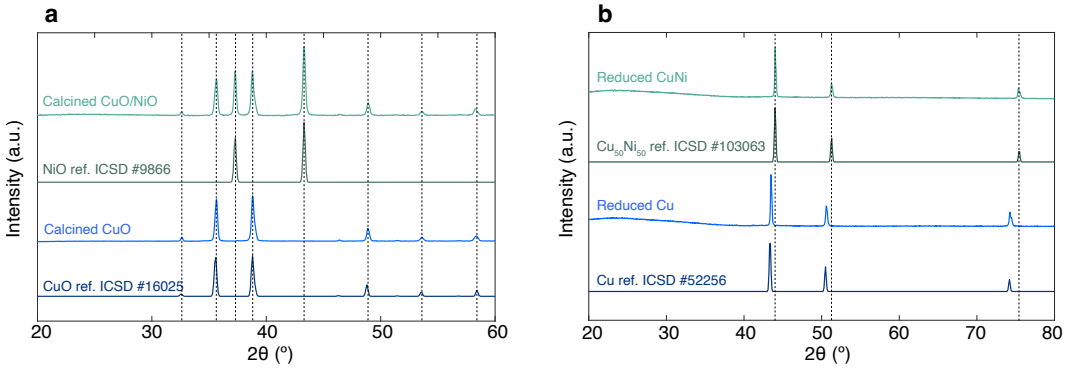

Figure 4.5: **XRD analysis of Cu and CuNi. a,** XRD patterns of calcined gels: $Cu(NO_3)_2$ gel is converted to CuO and $Cu(NO_3)_2/Ni(NO_3)_2$ gel is converted to CuO/NiO. **b,** XRD patterns of oxides reduced to parent metals: CuO is converted to Cu, and CuO/NiO is converted to a homogenous CuNi alloy, as evidenced by the single set of FCC reflections.

XRD patterns for the Ni, Ag, and CuAg systems support the conclusions drawn from the Cu and CuNi systems–that calcination converts the metal-nitrate-swollen precursor gel to a metal oxide, and subsequent treatment with forming gas reduces the metal oxide to the parent metal(s). Notable differences occur in the Ag and CuAg systems. In both systems containg Ag, elemental silver is formed during calcination, an unsurprising result given that silver nitrate is known to decompose to metallic silver under these conditions [144]. Additionally, the CuAg system is phase separated into Cu- and Ag-rich domains after reduction in forming gas, evidenced by the presence of reflections corresponding to pure Ag and pure Cu in the XRD patterns of 4.7d and the EDS maps in Figure 4.10. This is a result of Cu and Ag being immiscible, evidenced by the phase diagram [145] (see Figure 4.6).

4.2.2.3 TGA and DSC analysis

Figure 4.8 contains TGA and DSC data for Cu and CuNi gels heated in air at 1 °C/min; equivalent data for Ni, CuAg, and Ag is provided in Figure 4.9. The Cu and CuNi precursor gels, respectively, exhibit a similar mass loss profile to 12.7% and 15.8% of the original mass, reaching completion between 370 °C and 380 °C, indicated by mass stabilization at full conversion. The derivative of sample weight with respect to temperature, dW/dT, shows the regions of highest mass loss rate of ~1 wt.%/°C that occur at 353 °C for Cu and at 331 °C for CuNi. Guides are placed at 110 °C, where initial dW/dT peaks occur for both Cu and CuNi, and 265

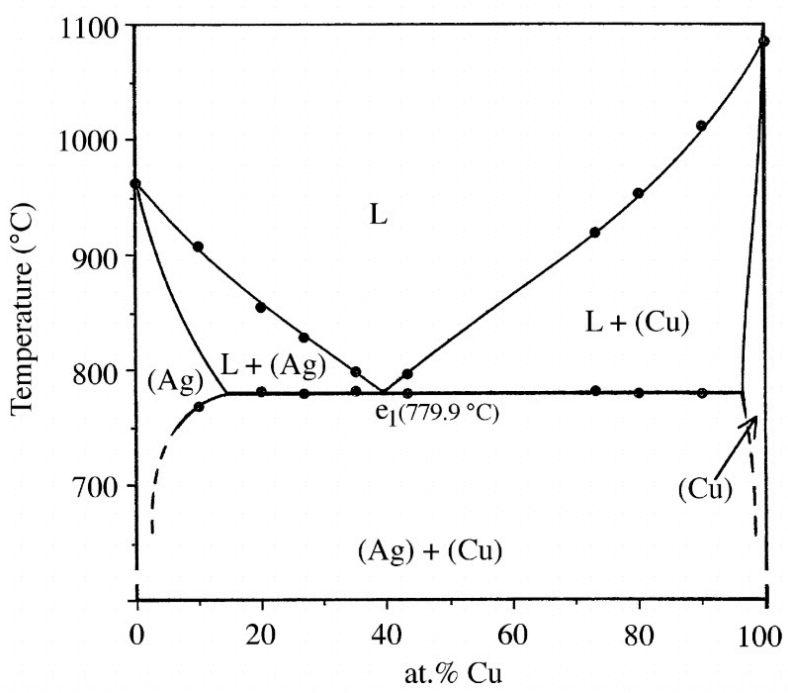

Figure 4.6: **Ag-Cu phase diagram.** The phase diagram shows that at 700 °C, the annealing temperature at which the CuAg samples are held, Cu and Ag are not miscible. Reproduced with permission from reference [145]. Copyright Elsevier Science & Technology Journals 2009.

°C, where a subsequent dW/dT peak occurs for only Cu. Figure 4.8b contains DSC profiles of Cu and CuNi precursor gels heated in air at 1 °C/min. Both gels exhibit similar normalized heat flow profiles; exothermic peaks begin at ~235 °C for both and reach a maximum heat flow of ~1.5 W/g at 308 °C for Cu, and -2.6 W/g at 304 °C for CuNi.

TGA and DSC analyses of Cu and CuNi calcination reveal that the water initially bound to the hydrogel polymer network evaporates below ~100 °C, indicated by the endothermic heat flow of ~ 0.25 W/g present in the DSC profiles of both materials below 100 °C [146]. Multiple thermally induced processes occur simultaneously upon further heating. For example, between 100 °C and 400°C, the Cu sample undergoes 1) dehydration of $Cu(NO_3)_2 \cdot xH_2O$ to anhydrous $Cu(NO_3)_2$, 2) thermal decomposition of anhydrous $Cu(NO_3)_2$, 3) an exothermic combustion reaction [147] in which the nitrate salt acts as an oxidizer of the PEGda ($C_{26}H_{46}O_{13}$) polymer network through the reaction $Cu(NO_3)_2 + \eta(C_{26}H_{46}O_{13}) + (31\eta\text{-}2.5)\ O_2 \longrightarrow CuO + 23\eta\ H_2O + 26\eta\ CO_2 + N_2$, where η is the molar ratio of PEGda to nitrate salt, and 4) thermal decomposition of PEGda.

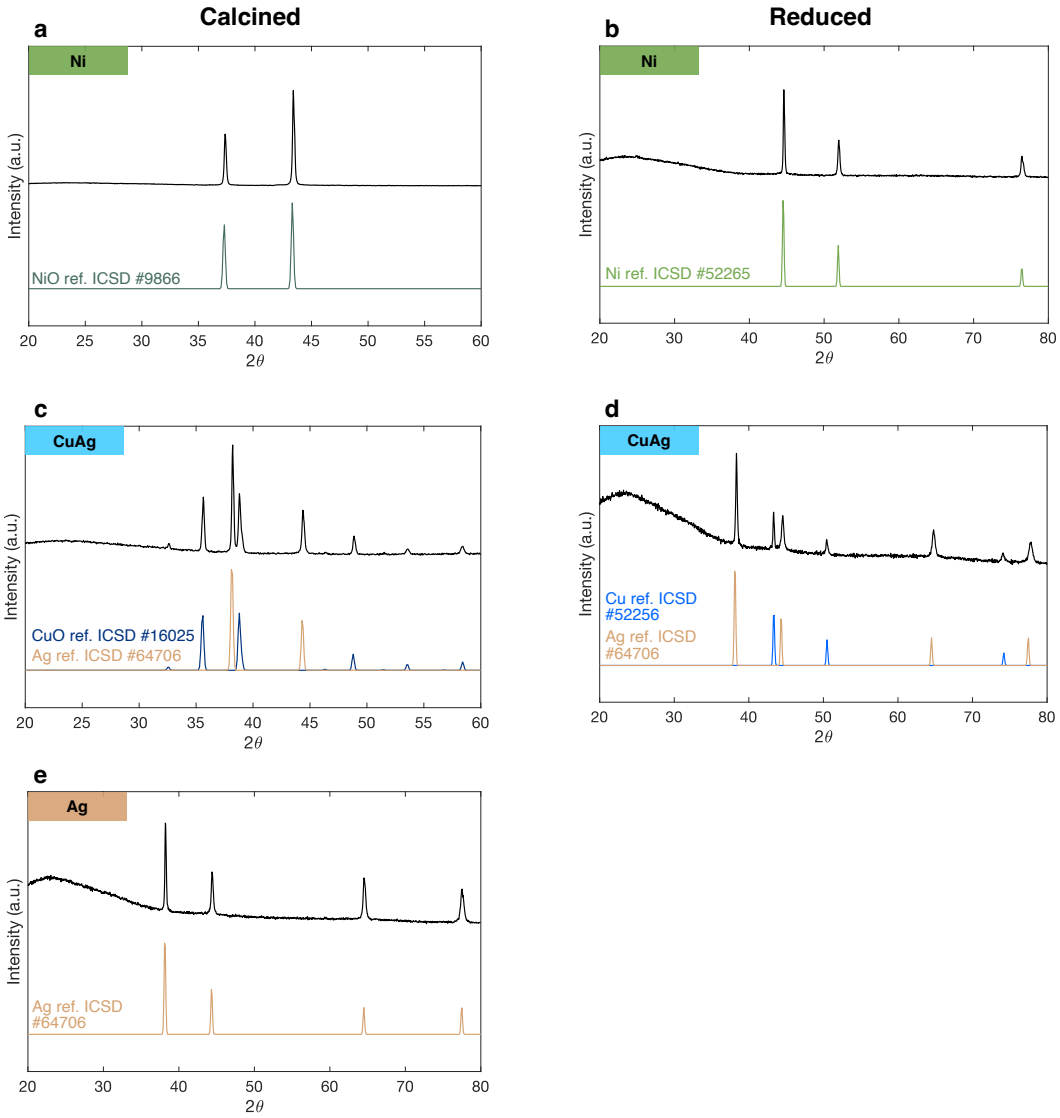

Figure 4.7: **XRD analysis of additional Cu/Ni/Ag metals and alloys.** X-ray diffraction patterns after calcination of **a,** Ni gel, showing conversion to NiO, **c,** CuAg gel, showing conversion to a mixture of CuO and metallic Ag, and **e,** Ag gel, showing conversion to metallic Ag. XRD patterns after reduction of **b,** NiO, showing conversion to metallic Ni, and **d,** CuO/Ag, showing conversion to phase separated Cu and Ag.

TGA and DSC profiles of the CuNi samples suggest a similar process occurs as in the pure Cu sample, with a distinction being that the copper nitrate and nickel nitrate salts simultaneously decompose and act as oxidizers for polymer combustion.

Both Cu and CuNi precursor gels exhibit a strongly exothermic peak around 300 °C that is attributed to the combustion of the PEGda polymer scaffold. The rates and temperatures of maximum heat flow are -1.5 W/g at 308 °C for Cu, and -2.6 W/g at 304 °C for CuNi (Figure 4.8b) and indicate that, during calcination, the CuNi gel releases heat more rapidly. This finding is consistent with our observation that the rate of maximum heat flow in the Ni gel is even higher, at -3.97 W/g at 333 °C (Figure 4.9b). The onset of this exothermic event is similar for Cu and CuNi, (~235 °C), while the onset of the corresponding event in pure Ni occurs at a significantly higher temperature of ~295 °C. This trend suggests that the heat released from the exothermic combustion of the copper nitrate salt in CuNi is sufficient to quickly increase the local temperature in the gel to the point where the nickel nitrate salt also contributes to the oxidation reaction at an apparently lower temperature, as is common in combustion synthesis [148].

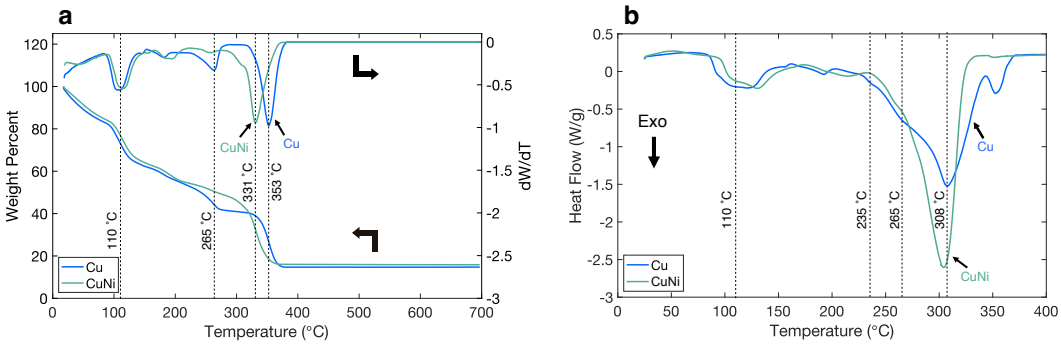

Figure 4.8: **TGA/DSC analysis of Cu and CuNi. a,** TGA profiles of metal ion-infused gels heated to 700 °C in air at 1 °C/min reveal rapid mass loss events reaching maxima at 353 °C for Cu and 331 °C for CuNi. **b,** DSC profiles of metal ion-infused gels heated to 400 °C in air at 1 °C/min reveal exothermic events with maximum heat flow at 308 °C for Cu and at 304 °C for CuNi.

4.2.3 Mechanical characterization of Cu and CuNi

Nanoindentation experiments performed on HI-derived Cu and CuNi revealed the hardness of Cu to be 1.81 ± 0.37 GPa and that of CuNi to be 2.15 ± 0.22 GPa. To contextualize these results, Figure 4.11 contains a plot of nanoindentation hardness vs. grain size for the HIAM-produced Cu and CuNi in this work compared to data from literature for the same metals produced via traditional processing techniques (see Table A.4 for tabulated data). The plot also contains the expected hardness based on the Hall-Petch relation $H = H_0 + kd^{-1/2}$, which relates nanoindentation

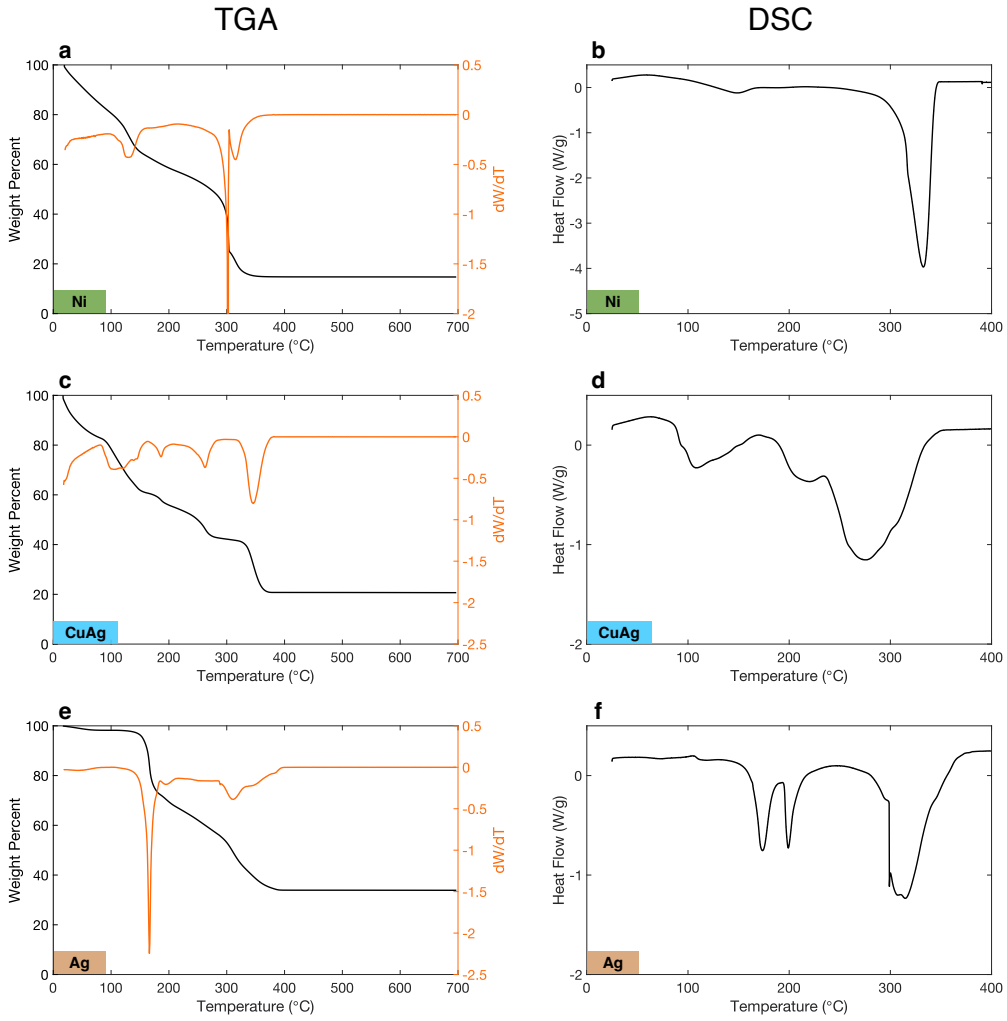

Figure 4.9: **TGA/DSC data for additional metals.** TGA data for **a,** Ni **c,** CuAg, and **e,** Ag. DSC data for **b,** Ni **d,** CuAg, and **f,** Ag.

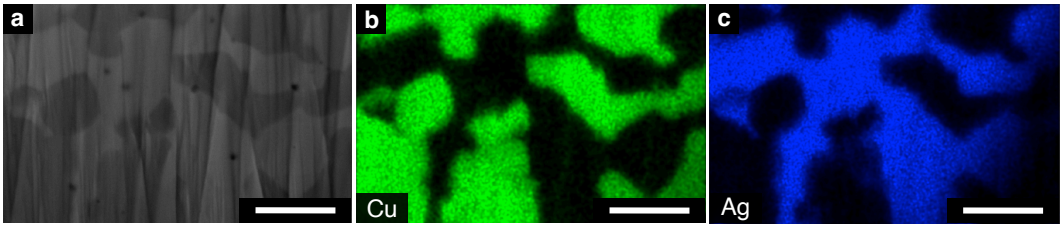

Figure 4.10: **EDS mapping for CuAg showing heterogeneous alloying.** The CuAg material forms a dense, heterogeneous alloy, with separate ~5 µm Cu- and Ag-rich phases. This phase separation is predicted by the Cu-Ag phase diagram [145], and can be seen by **a,** regions of differing contrast in secondary a electron SEM image, as well as in EDS maps of a FIB-milled cross section showing **b,** Cu-, and **c,** Ag-containing regions. Scale bars: **a-c,** 2 µm.

hardness H to grain size d for ductile metals, where H_0 is an intrinsic hardness for a single crystalline material and k is a scaling factor related to grain boundary-induced hardening [149, 150].

Twin boundaries are known to act as barriers to dislocation motion during deformation [139, 151] and thus effectively increase measured hardness. To account for this effect, we introduced a modified Hall-Petch relation to account for the high twin boundary density [152]. The relative strength of the twin boundary in resisting deformation changes for various metals and alloys; to set an upper bound on twin-induced hardening, the twin boundaries are effectively treated as grain boundaries and the grain size d becomes $d_{eff} = \frac{D}{N+1}$, where N is the number of twin boundaries per grain (see Section A.2.1 for derivation of this expression). Since CuNi is far more sensitive to boundary impact on hardening than Cu (as evident by the 3.8 times larger k value in CuNi), there is a stronger effect of the twin boundaries even though there are ~25% less twins than Cu.

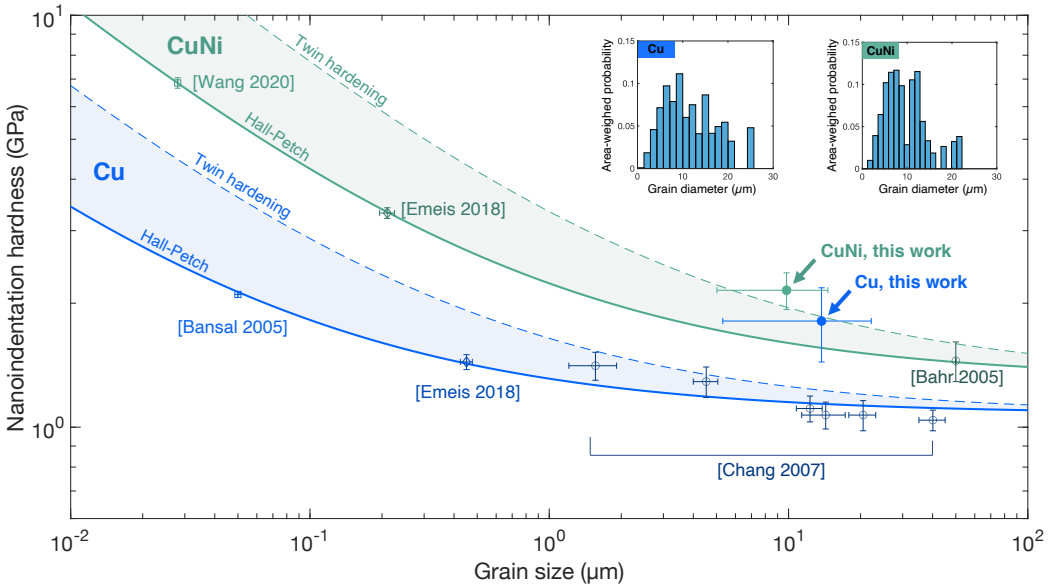

Figure 4.11: **HI-derived Cu and CuNi nanoindentation hardness.** Nanoindentation hardnesses of HI-derived Cu and CuNi samples are higher than reference nanoindentation data [140–142, 153, 154] and extrapolated Hall-Petch grain size scaling (dashed lines show correction for effect of twin-induced hardening). Error bars show standard deviations of grain size and nanoindentation hardness, where available. Insets: area-weighted grain size distribution for Cu and CuNi. Sample sizes: Cu hardness, n = 22; CuNi hardness, n = 44; Cu grain size, n = 246; CuNi grain size, n = 309.

HIAM-derived metals contain a high density of annealing twins, formed without the ordinarily requisite melting and recrystallization [155], due to the complex interplay between kinetic processes (i.e., solid-state diffusion and grain nucleation) and thermodynamic grain coalescence during high-temperature calcination and reduction.

Both Cu and CuNi exhibit higher hardness than the Hall-Petch predicted values even when corrected for twin boundary presence, by 47% and 15%, respectively. While the spread in measured hardness can be attributed to variance in the locally probed microstructure (i.e., close proximity to twin boundaries and grain boundaries increasing hardness and the presence of micro-porosity reducing it), the greater average hardness is indicative of a global complexity in the material not explained by a simple microstructural mechanism, opening a new avenue for engineering and investigating complex material behavior.

4.3 High entropy alloys

We fabricated multicomponent alloys to demonstrate compositional flexibility of the HIAM process. In particular, we were motivated to explore high entropy alloys (HEAs), or alloys with 4+ components in (often) equimolar ratios, because these alloys are known to have desirable properties such as high strength and good corrosion resistance. Additionally, the compositional space represented by HEAs is enormous. Even restricting to equimolar compositions, Figure 4.12 shows that the number of alloys exponentially grows as more principal elements are considered [156]. If we additionally consider off-stoichiometric compositions, there are countless more compositions to explore. This compositional space is too large to explore via AM methods in which new compositions require new resins or new fabrication parameters. HIAM is an attractive technique to fabricate HEAs because of the simple ability to tune compositions, to add or remove elements as desired, and to parallelize fabrication, opening a path towards high-throughput experimentation.

4.3.1 Motivation for fabricating CuNiCoFe

We chose to target the CuNiCoFe system because nitrate precursors for each metal in this quaternary alloy are readily available, and the CuNiCoFe alloy has been well characterized. Equimolar CuNiCoFe (i.e., $Cu_{25}Ni_{25}Co_{25}Fe_{25}$) is expected to exist as a single phase with face centered cubic crystal structure [156].

4.3.2 Tuning the swelling solution to account for preferential incorporation

Based on the results of CuNi alloy experiments, we observed that certain precursors preferentially incorporate into the hydrogel network, and that this effect could be accounted for to achieve target alloy composition with precision by adjusting the swelling compositions after an initial experiment in which the degree of preferential incorporation for each component was measured.

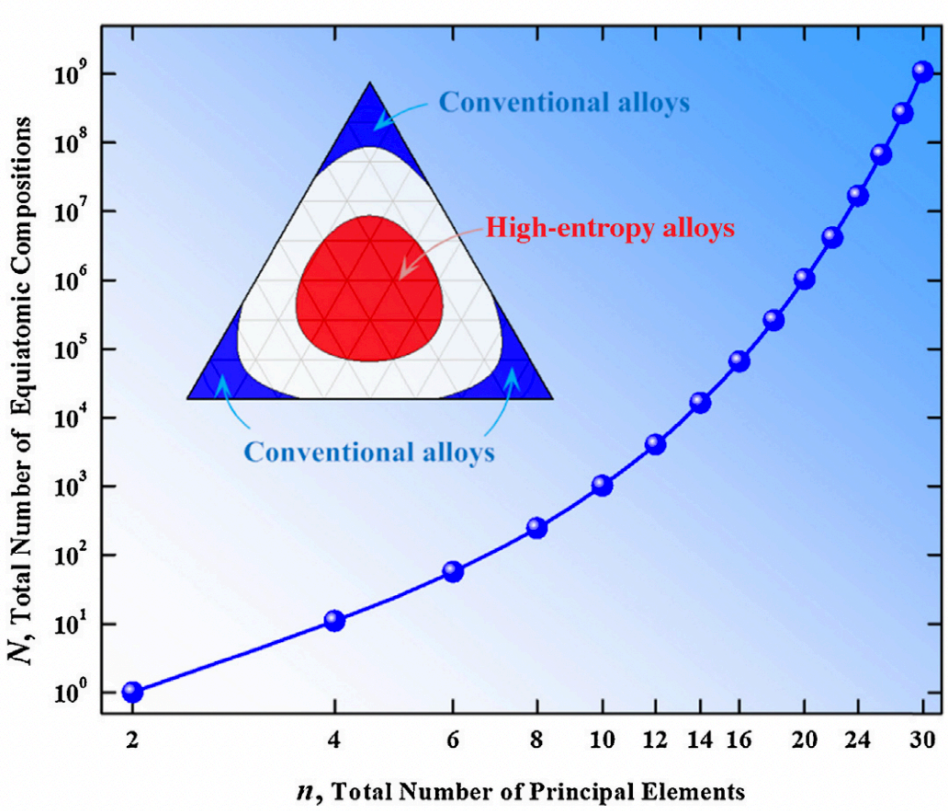

Figure 4.12: **High entropy alloy compositional space.** The total number of equiatomic compositions increases exponentially with the number of principal elements. Reproduced with permission from reference [156]. Copyright Elsevier Science & Technology Journals.

We hypothesized that we could tune the alloy composition by following the algorithm (as we did for the CuNi alloy), which implements a linear adjustment of the swelling solution to account for observed preferential incorporation:

1. Swell a hydrogel in a mixture of N precursors with molar ratios $x_1, x_2, \ldots, x_N$ such that $\sum_i x_i = 1$.

2. Use EDS analysis to measure the stoichiometry of the alloy formed from step 1, with molar ratios of the N elements $y_1, y_2, \ldots, y_N$ such that $\sum_i y_i = 1$.

3. Define an incorporation ratio for each component: $\phi_i = y_i / x_i$.

4. Swell a 2nd hydrogel in a mixture of the same N precursors such that $x_{i,new} = y_{i,Target} / \phi_i$.

5. Finally, normalize: $x_{i,new,Norm} = \frac{x_{i,new}}{\sum_i x_{i,new}}$ such that $\sum_i x_{i,new,Norm} = 1$.

We applied this procedure to the fabrication of the CuNiCoFe alloy. First, we swelled a hydrogel in an equiatomic solution of $Cu(NO_3)_2$, $Ni(NO_3)_2$, $Co(NO_3)_2$, and $Fe(NO_3)_3$ such that $x_{Cu} = x_{Ni} = x_{Co} = x_{Fe} = 0.25$ and the total concentration of metal cations was 2M. After calcination, EDS revealed that the molar ratios of the metals were $y_{Cu} = 0.16$, $y_{Ni} = 0.18$, $y_{Co} = 0.19$, $y_{Fe} = 0.47$. We note that iron is by far preferentially incorporated compared to copper, nickel, and cobalt. This is a result of iron being the only trivalent metal, causing stronger interactions with the PEGda polymer backbone.

After applying the algorithm described above, we formed an alloy with the composition $Cu_{23}Ni_{28}Co_{31}Fe_{18}$, quantified by EDS analysis in Figure 4.13. Hereafter this composition is referred to as CuNiCoFe. Compared to the CuNi system, where there are only two components, and the incorporation ratios are similar, the CuNiCoFe system contains more interactions between different elements, and has a wider range of incorporation ratios due to the presence of both divalent and trivalent cations. Apparently, the linear adjustment works best when the components have similar interaction strengths, and the adjustment to swelling concentrations is small (as with CuNi), but nevertheless is a first step towards adjusting more complex systems.

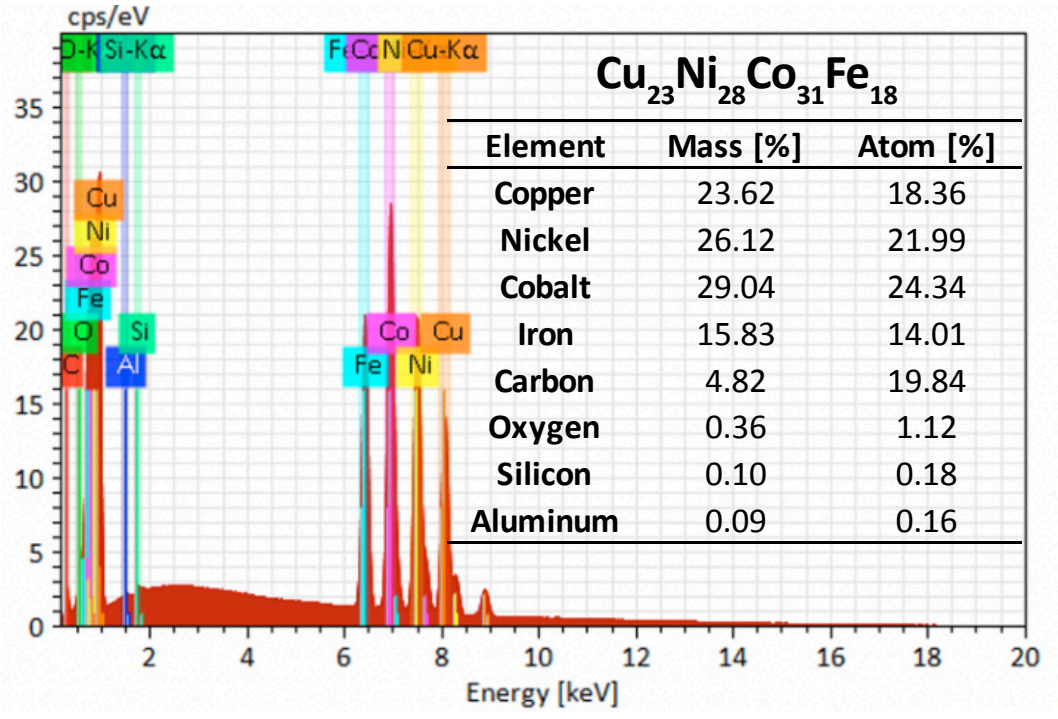

$Cu_{23}Ni_{28}Co_{31}Fe_{18}$

Element	Mass [%]	Atom [%]
Copper	23.62	18.36
Nickel	26.12	21.99
Cobalt	29.04	24.34
Iron	15.83	14.01
Carbon	4.82	19.84
Oxygen	0.36	1.12
Silicon	0.10	0.18
Aluminum	0.09	0.16

Figure 4.13: **CuNiCoFe EDS spectrum and quantification.** EDS spectrum quantifying the alloy composition as $Cu_{23}Ni_{28}Co_{31}Fe_{18}$.

4.3.3 CuNiCoFe fabrication

Like other materials fabricated, the CuNiCoFe structures were swelled for 24 hr at 70 °C in a solution containing a mixture of nitrate salts as described above. The structures were then calcined at 700 °C in air, and reduced at 900 °C in forming gas, following the same procedures as described in the Methods section. Supplementary Figure 4.14a-d shows the steps in the fabrication of the CuNiCoFe alloy, from infused gel to metal alloy.

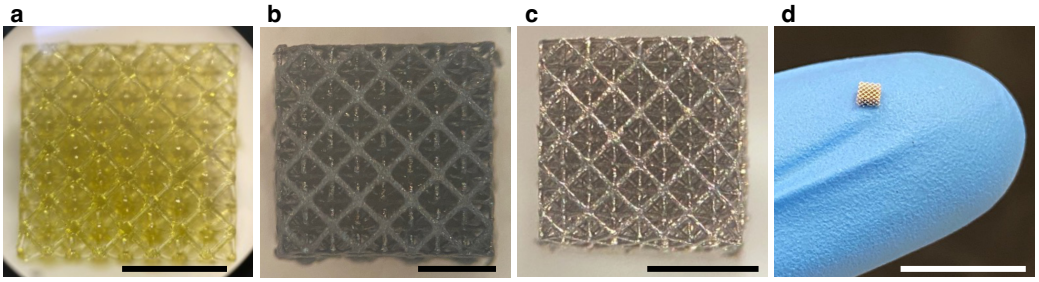

Figure 4.14: **CuNiCoFe high entropy alloy fabrication.** **a**, CuNiCoFe infused hydrogel is converted to **b**, CuNiCoFe oxide after calcination and **c,d,** CuNiCoFe alloy after reduction. Scale bars: **a**, 3 mm; **b,c,** 1 mm; **d,** 1 cm.

4.3.4 Phase separation in CuNiCoFe alloy

4.3.4.1 EDS analysis of CuNiCoFe

Like other HIAM metals, CuNiCoFe is microcrystalline (Fig 4.15a). Unlike CuNi, which formed a homogenous alloy, we observed phase separation into at least two phases in the reduced CuNiCoFe alloy, evidenced by Cu-rich and Cu-poor regions in the EDS mapping of this material (Fig 4.15b).

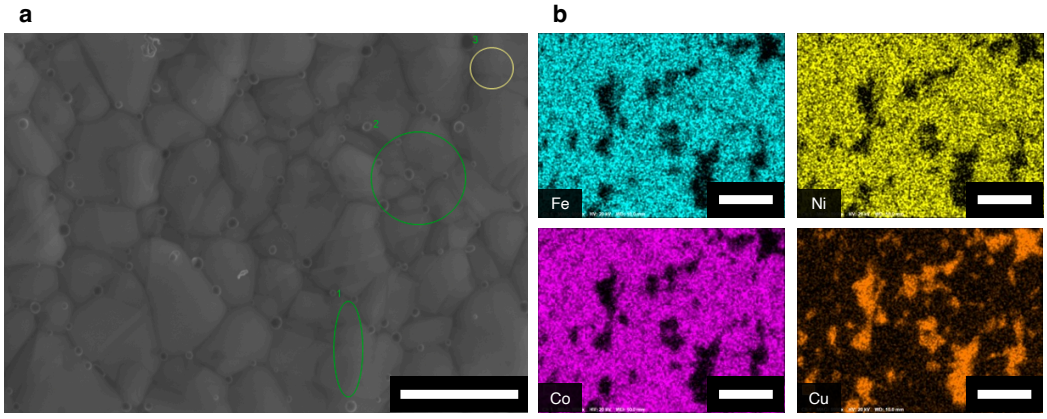

Figure 4.15: **CuNiCoFe EDS map.** **a**, SEM image shows a micro-grained microstructure, and **b**, EDS mapping shows that there are Cu-rich and Cu-poor regions throughout. Scale bars: **a,b,** 3 µm.

Overlaying the Cu EDS map with the SEM image gives a sense of the relationship between chemical content and observable grain and twin boundaries (4.16). It is clear that the high Cu-content regions correspond to some observable grain boundaries. Quantification of these EDS maps in the sub-regions denoted 1, 2, and 3, in (Fig 4.16a) shows that the Cu-rich regions (1 and 3) have >50 at% copper, while the Cu-poor region (2) has 12% copper (See Figure A.6 for detailed sub-region element quantification).

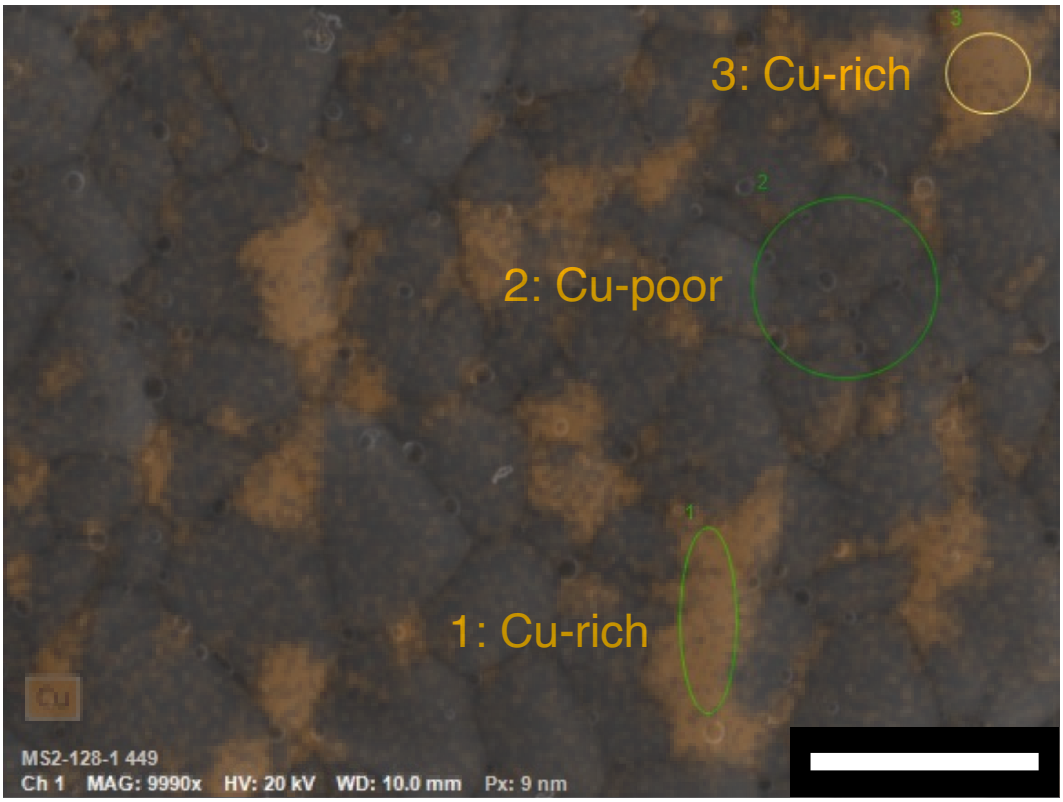

Figure 4.16: **CuNiCoFe SEM image overlayed with Cu EDS map.** EDS analysis shows that the CuNiCoFe HEA has regions of high copper content (>50 at%, Cu-rich) and low copper content (~12 at%, Cu-poor). Scale bar: 3 µm.

4.3.4.2 XRD analysis of CuNiCoFe

After calcination, we observed two phases via XRD (Figure 4.17a), with one set of reflections corresponding to a monoclinic CuO-type structure, and another corresponding to a cubic NaCl-type (NiO-like) structure. After reduction of this mixed-phase oxide material, we observed two phases via XRD (Figure 4.17b), with two sets of reflections, each corresponding to face-centered cubic (FCC) structures with different lattice parameters. This is expected given the phase separation we observe in the EDS mapping, and the fact that CuNiCoFe alloys are predicted to form FCC

structures. The difference in composition between the Cu-rich and the Cu-poor alloy phases is enough to shift the Cu-rich phase reflections to slightly lower diffraction angles, a result of slightly larger lattice spacing due to the incorporation of the larger Cu atom. Like the CuNi alloy, the CuNiCoFe alloy forms several oxide phases after calcination. However, in the CuNi system, these phases diffuse to form a single FCC CuNi phase, with no evidence of compositional gradients. In the CuNiCoFe system, the amount of annealing during the reduction step may not be sufficient, leading to compositional gradients in the final structure.

4.3.5 Structural characterization of CuNiCoFe

We additionally performed FIB/SEM analysis of the CuNiCoFe alloy, shown in Figure 4.18. As with other metals, the designed octet lattice structure is well-maintained throughout the process (Figure 4.18a). SEM images of a FIB-milled cross-section of a node (Figure 4.18d,f) reveal some ~10 μm-thick lamellar pores.

4.4 Tungsten-containing materials

Tungsten, a refractory metal, is both very useful and hard to shape due to its high melting point of ~ 3400 °C. Additive manufacturing of tungsten and tungsten composites remains a challenge in the field. Existing examples of tungsten AM include selective laser beam melting [157] as well as direct ink writing and subsequent H_2-reduction of WO_3-containing inks [158].

4.4.1 Fabrication of W-Ni

So far, we have shown that HIAM is compatible with metals that have metal nitrate salt precursors; tungsten has no equivalent water-soluble precursors. As such, we investigated a new class of HIAM precursors to fabricate tungsten, in which the target material exists not as a cation, but as part of an anion complex. We chose ammonium metatungstate hydrate (AMT, $(NH_4)_6H_2W_{12}O_{40} \cdot xH_2O$, Sigma Aldrich) as a precursor due to its solubility and stability in water. AMT has also been shown to decompose to WO_3 under calcination [159], and has even been used as a precursor in an AM process [160]. Based on the findings of Dunand and coworkers [158], we added a small amount of $Ni(NO_3)_2$ to the swelling solution to act as a sintering aid during the reduction of WO_3-Ni to W-Ni. Hydrogels were swelled in a mixture of 98.5% 2M AMT (W atom basis) and 1.5% 2M $Ni(NO_3)_2$ at 70 °C for 2 weeks. The samples then underwent calcination at 0.25 °C/min to 500 °C, then 1 °C/min to 700 °C, and a 3-hour isothermal hold. The samples were

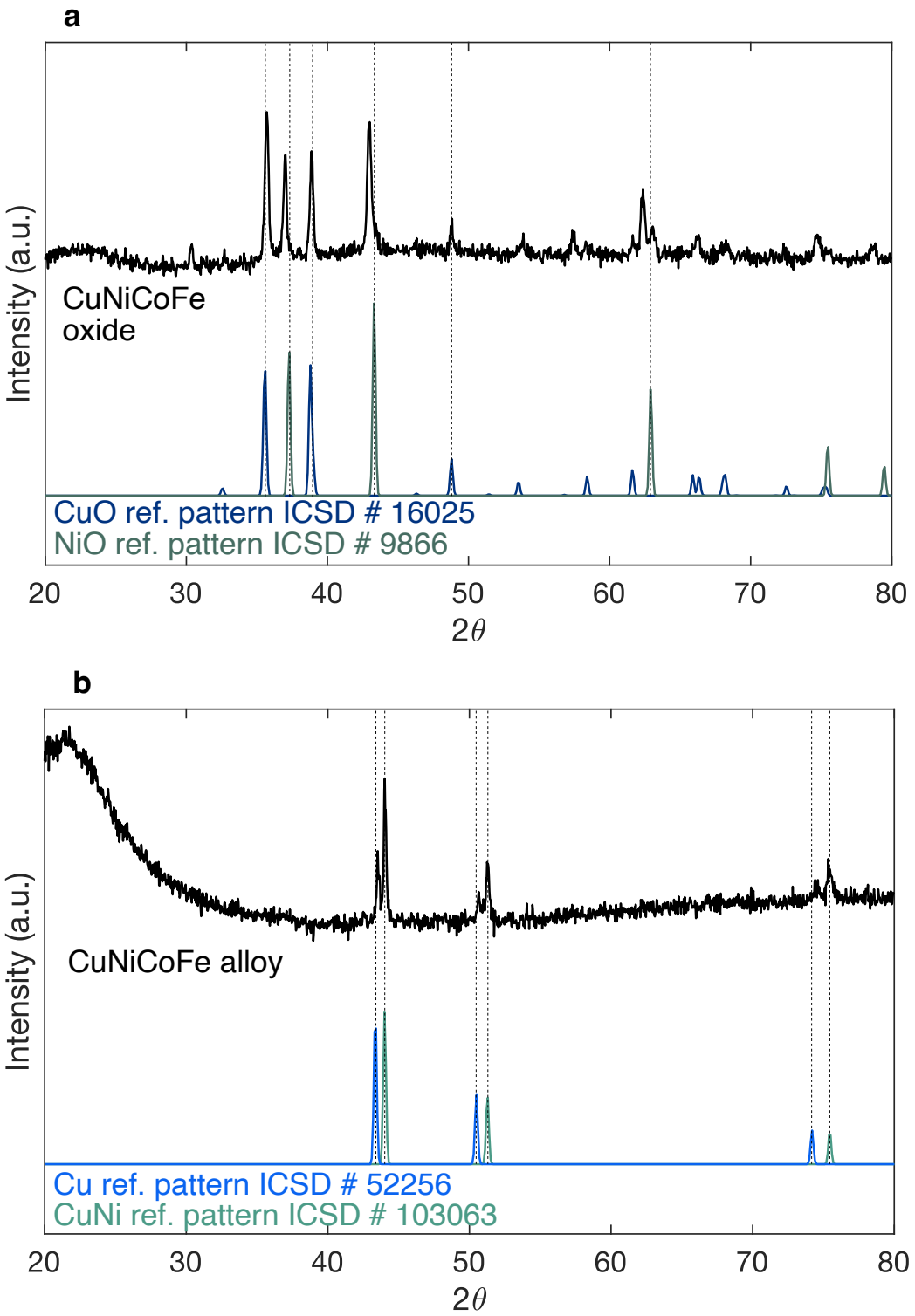

Figure 4.17: **CuNiCoFe XRD analysis. a,** XRD pattern of calcined CuNiCoFe gel shows two phases: 1) a CuO-like phase (monoclinic CuO-type structure) and 2) a NiO-like phase (cubic NaCl-type structure). **b,** XRD pattern of reduced CuNiCoFe alloy shows two face-centered cubic phases with different lattice parameters (Cu and CuNi patterns for reference).

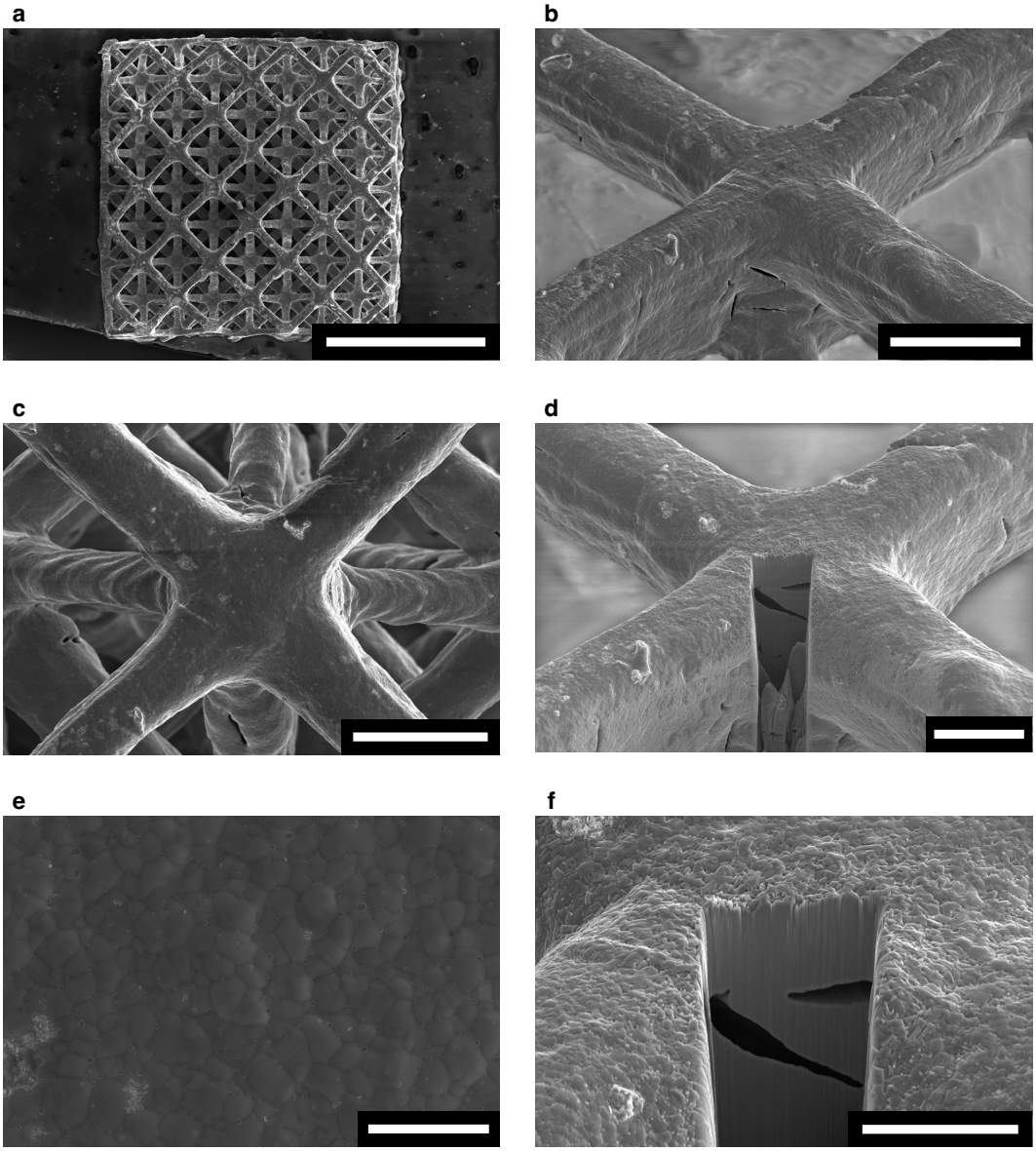

Figure 4.18: **CuNiCoFe FIB/SEM analysis.** SEM images of the CuNiCoFe lattice showing **a,** an overview (top view), **b,** a single node (52 °tilt view), **c,** a single node (top view), **d,** a FIB-milled cross-section at the node (52 °tilt view), **e,** microcrystalline grain structure, **f,** zoomed-in view of the FIB-milled cross-section. Scale bars: **a,** 1 mm; **b,c,** 100 µm; **d,** 50 µm; **e,** 10 µm; **f,** 30 µm.

reduced following a thermal profile of 3 °C/min to 1200 °C and a 1-hour isothermal hold, under forming gas at a flow rate of 500 sccm at atmospheric pressure (through a gas bubbler). Figure 4.19 shows the steps in the fabrication process, from oxide to metal. Like other HIAM processes with metal nitrate salts, the HIAM process with AMT as a W precursor yields microlattices with beam diameters of ~50 µm. EDS analysis of W-Ni structures in Figure 4.20 shows that HIAM can produce W-Ni lattices with >90 wt% tungsten.

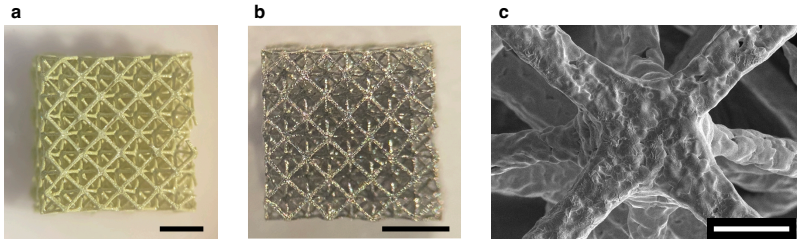

Figure 4.19: **W-Ni fabrication steps.** **a**, A WO_3-Ni microlattice is converted to **b,c,** a W-Ni microlattice after reduction. Scale bars: **a,b,** 1 mm; **c,** 100 µm.

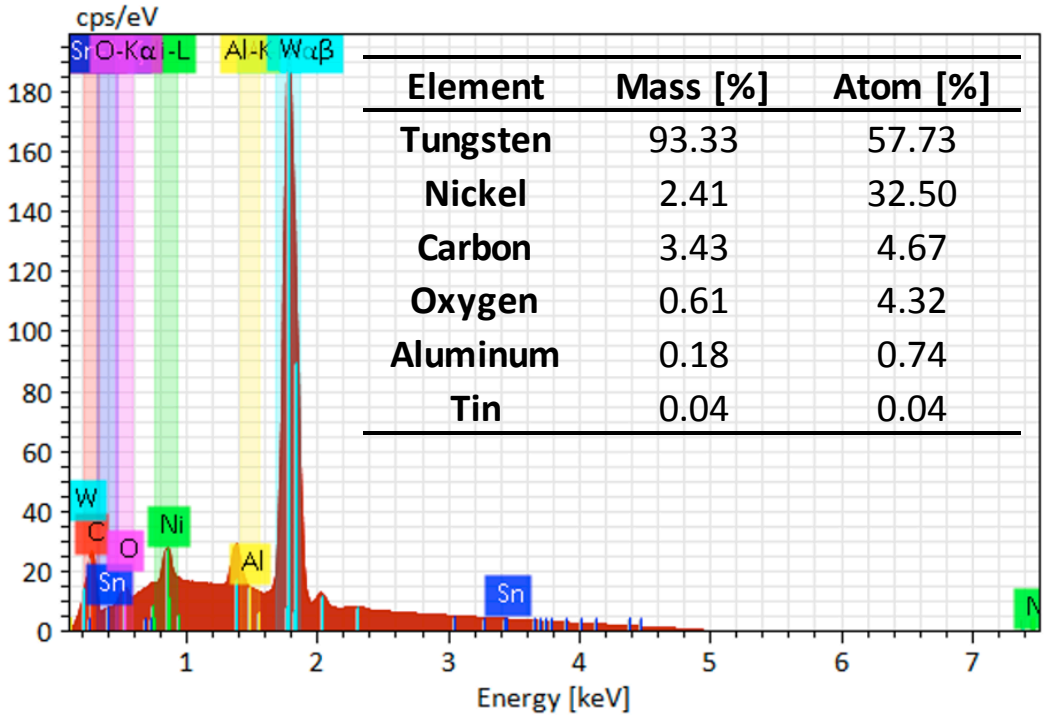

Element	Mass [%]	Atom [%]
Tungsten	93.33	57.73
Nickel	2.41	32.50
Carbon	3.43	4.67
Oxygen	0.61	4.32
Aluminum	0.18	0.74
Tin	0.04	0.04

Figure 4.20: **W-Ni EDS analysis.** EDS analysis at 5kV accelerating voltage shows that the lattice is over 90% tungsten by mass.

4.5 Parallelization of HIAM

HIAM stands out amongst other functional material AM methods for its ability to be parallelized. Because part shaping and material selection are both temporally and

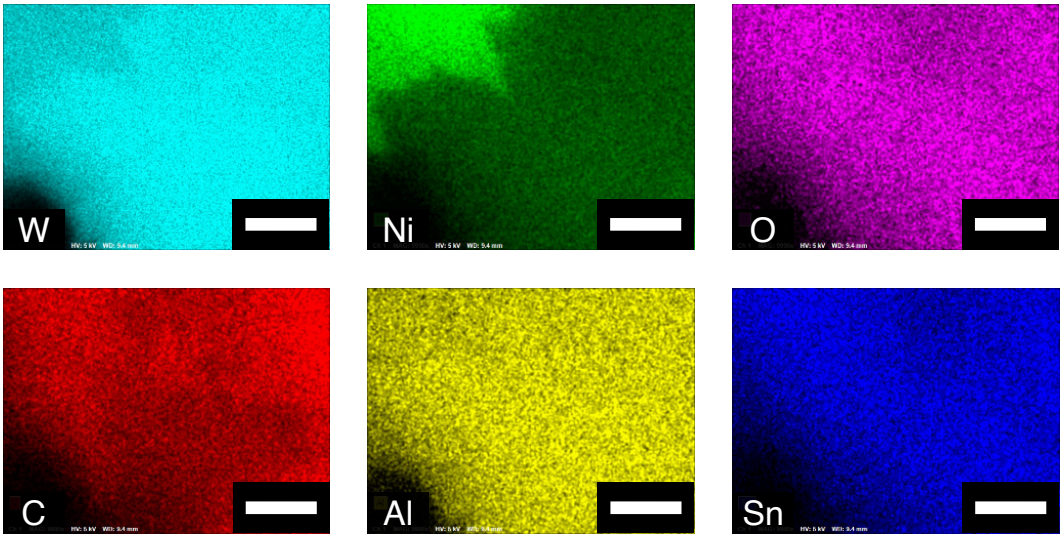

Figure 4.21: **W-Ni EDS mapping.** EDS maps show some separation of Ni to grain boundaries. Scale bars: 3 µm.

spatially separated, many gels can be printed simultaneously, infused simultaneously in different precursor solutions, and then heat-treated simultaneously. Figure 4.22 shows 8 hydrogel lattices (precursors of Cu, CuNi, CuNiCoFe, and CuNiCoFeCr) being simultaneously calcined to form oxides.

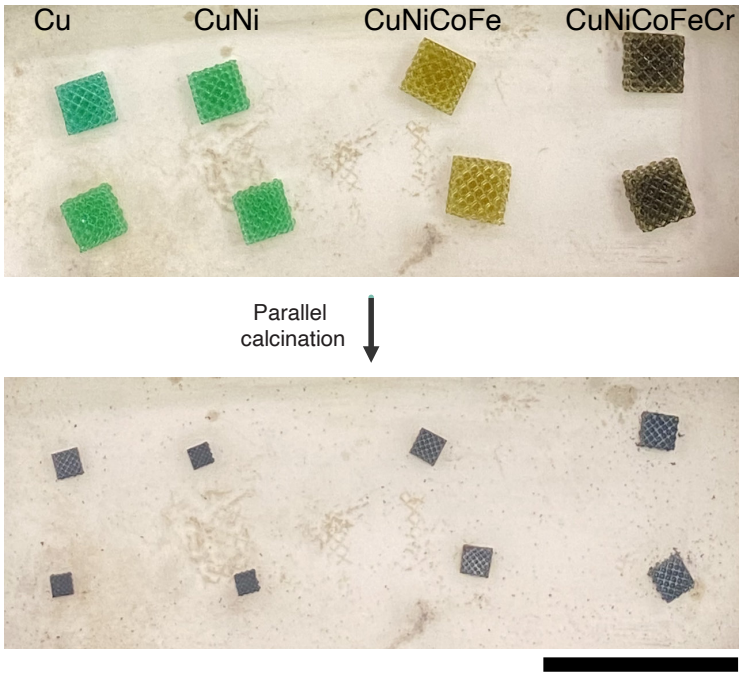

Figure 4.22: **Parallel calcination of 8 infused gels.** 8 infused gels (top) containing precursors for Cu, CuNi, CuNiCoFe, and CuNiCoFeCr were calcined simultaneously to form oxides (bottom). Scale bar: 2 cm.

4.6 Multi-materials

In alloys, multiple components combine to give these materials properties different than the principle components. In homogenous alloys such as HIAM-derived CuNi, the components Cu and Ni are mixed at the atomic level, forming a single phase material. Alternatively, in heterogeneous alloys such as HIAM-derived CuAg and CuNiCoFe, multiple phases are present, leading to multiple phases which mix at the micron scale. However, because we generally interact with materials at the mm to cm scale or larger, even these heterogeneous alloys can be thought of as alloys because the variation occurs on a scale many orders of magnitude smaller. Depending on the application, the distinction between a heterogenous alloy and multiple materials may vary, but for the sake of argument, let us make use of a definition in which a material appears homogenous to a human, i.e., a human could not, without the use of a microscope or other characterization tools, identify the multiple components.

Increasing the scale at which multicomponent materials have their principle components separated brings us to the realm of multi-materials, in which the component domains reach a distinguishable size. Multi-material additive manufacturing (MM-AM) is a particularly useful approach to AM, in which not only can the overall shape of the fabricated part be arbitrarily designed, but the material selection at each point in the structure can also be chosen [161].

4.6.1 Multimaterial AM methods

Multimaterial fabrication has been demonstrated for a variety of AM techniques. Extrusion techniques such as FDM and DIW perhaps offer the most straightforward implementation of multimaterial printing, as the feedstock material can be changed in the middle of printing. For example Lewis and coworkers demonstrated multimaterial DIW with a multinozzle printer [162].

Because other VP techniques for AM of functional materials rely on resins that contain precursors of the final material, creating multimaterials requires switching out the resin bath for each new material layer, or using a dual-wavelength system in which two different components are cured with different wavelengths of light [163].

4.6.2 Multimaterials fabricated via HIAM

HIAM enables a more streamlined approach to multimaterials, where the material deposition can be defined based on directed infusion of active material precursors. To demonstrate this capability, octet lattices with beam diameters of 400 µm were printed, and then infused from either end with a different precursor solution to form a Cu/Co multimaterial, shown in Figure 4.23.

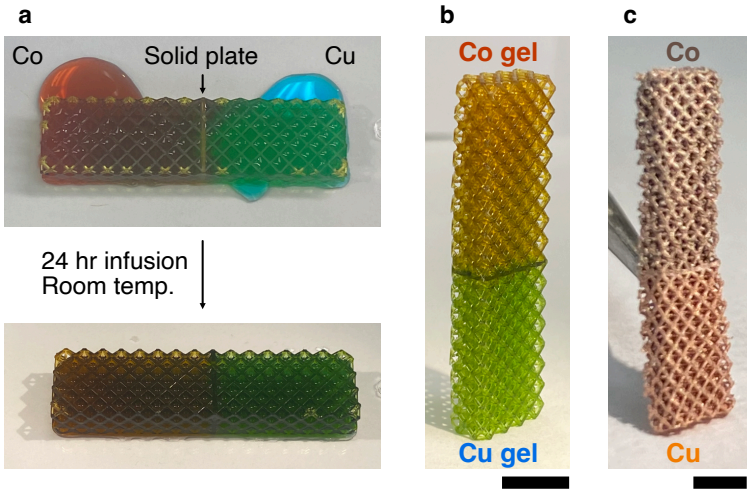

Figure 4.23: **Cu/Co multimaterial. a,** An octet lattice structure divided by a solid internal plate was swelled horizontally with $Cu(NO_3)_2$ from one end and $Co(NO_3)_2$ from the other end for 24 hours at room temperature. After infusion and drying, the result was a **b,** Cu/Co precursor gel. After calcination and reduction, a **c,** Cu/Co multimaterial was formed. Scale bars: **b,** 1 cm; **c,** 2 mm.

The ability to form multimaterials via HIAM represents a clear point of departure from all previous VP methods that can fabricate functional materials, which require switching out multiple precursor-containing resin baths or using a dual-cure multi-wavelength setup.

The fabrication of the Cu/Co multimaterial via HIAM was a proof of concept for using directed swelling to create multimaterials, but results in several important takeaways. It is possible to fabricate multimaterials, evidenced by the clear distinction in color both in the precursor gel state and in the reduced metal state. However, several key challenges presented that need to be solved to effectively implement multimaterial HIAM. Some of these challenges are engineering problems, and some have broader implications for the viability of this method, or impose some design restrictions.

An obvious challenge is how to localize swelling solutions to particular regions of the gel precursor. In this proof of concept, the boundary between the two materials

is a plane, which is the simplest case to implement experimentally. The solid plate dividing the lattice (see Figure 4.23a) was needed to prevent the solutions on each side of the lattice from mixing, but it did not work perfectly; the surface tension of the liquids allowed some to cross the barrier. The ability for HIAM to create multimaterials is fundamentally limited by how swelling solutions can be introduced to different regions of a printed part. In some cases, such as printing intertwined tubes, this could be done easily. In other cases, it can be more challenging to prevent swelling solutions from mixing. However, recent work from Duoss and coworkers has beautifully shown the promise of using 3D architected cellular solids as devices to direct fluid flow [164]. In the future, combining cellular fluidics with hydrogel infusion additive manufacturing could open up a new and powerful realm of multi-material vat photopolymerization AM.

Another important step for future work of multimaterials fabricated via HIAM is to understand what the joint regions look like. It is well known that interfaces between materials can act as hotspots for defects and weaknesses, so there are likely material constraints on what types of materials can be joined via HIAM.

Finally, the shape changes associated with the HIAM process must be taken into account to prevent undue warping of the materials. For instance, materials should have similar amounts of linear shrinkage to prevent stress from building up at interfaces. Even with the Cu/Co example, differential shrinkage between the Cu segment and the Co segment led to noticeable warping of the final part. An ideal candidate for a multimaterial would be Cu and CuNi, which both exhibit similar amounts of linear shrinkage, and also have similar decomposition temperatures for their precursor gels.

4.7 Hydrogel infusion additive manufacturing outlook

4.7.1 Material selection after part shaping

In nearly every AM process to date, the final material is decided prior part shaping, i.e., the AM material feedstock is often the desired material itself or contains precursors that can be subsequently converted into the desired material after part-shaping. The composition of the fabricated 3D structure is thus either that of the feedstock or of some clear derivative of it. To fabricate the same structure out of a different material necessarily requires the use of a different resin or feedstock formulation. In the context of ceramic and metal VP, this means that regardless of the slurry or inorganic-organic hybrid approach, the fabrication of each inorganic material

requires an involved process of photoresin design and formulation, in addition to print parameter optimization.

HIAM is fundamentally different from the state of the art in that the material is selected after part shaping. We have shown that a blank organogel structure fabricated from a single resin formulation can be transformed into a vast number of different compositions. Because the inorganic precursors are infused only after part shaping, HIAM is unlike traditional slurry or inorganic-organic hybrid resin approaches in that only a single photoresin composition needs to be designed and optimized for VP, which significantly simplifies the material development process. We have shown that this ability allows HIAM to fabricate geometrically and compositionally complex 3D materials such as refractory metals and high entropy alloys, as well as multimaterial structures, a previously impossible task for VP.

4.7.2 Beyond DLP printing

HIAM is not limited to DLP printing; this methodology is generalizable to other polymer AM processes which can produce gels such as stereolithography, direct ink writing, or could be adapted to higher resolution VP via two photon lithography processes.

4.7.3 HIAM materials horizons and applications

We developed an AM process to create microscale metal 3D structures using a facile and versatile VP approach. The conversion of metal salts within polymer scaffolds to metal oxides and their subsequent reduction to metals and alloys is a general process, requiring only that the target material has water-soluble precursors and that the intermediate oxide formed after calcination can be reduced by hydrogen gas. The ability to fabricate metallic materials using this accessible and high-resolution process provides new opportunities for fabrication of energy materials, micro-electromechanical systems, and biomedical devices. Hydrogel infusion represents a paradigm shift in AM, where the material is selected only after the part is shaped; directed infusion can create metallic multimaterials, and unprecedented compositional flexibility enables the fabrication of multicomponent alloys such as high entropy alloys and refractory alloys, known to have intermetallic phases which lead to superior high temperature behavior, and enhanced yield strength [165]. HIAM has direct implications for industrial use, as it provides a practical and powerful capability to integrate into the burgeoning and commercially advanced VP printing ecosystem.

Chapter 5

THESIS SUMMARY AND OUTLOOK

So take that laminate out of your wallet and read it
And recommit yourself to the healing of the world
And to the welfare of all creatures upon it
Pursue of practice that will strengthen your heart

John K. Samson, *Postdoc Blues*

5.1 Thesis summary

In this thesis, I reported two new methodologies for fabricating functional materials via vat photopolymerization, and showed how each can be useful. The first, *emulsion stereolithography*, is a novel way for introducing functional material precursors into a photopolymer resin, making use of aqueous precursors emulsified in an organic photopolymer resin. I showed that sulfate salts can be carbothermally reduced to sulfides and the polymer backbone pyrolyzed to carbon *in situ* after part shaping, leading to sulfide-carbon composites which can be used as cathode materials in sulfur-based batteries. These cathode materials were thoroughly characterized chemically and electrochemically, and some interesting implications for materials design, such as the ability to tune pore size through the emulsion surfact loading were discovered. We detoured briefly into the nanomechanical realm to study the mechanical behavior of lithium sulfide powders, measuring for the first time when powder agglomerates will fracture under a compressive load, and compared these results to literature *in situ* stress evolution data in composite sulfur cathodes, which suggested that fracture of lithium sulfide powders or agglomerates may not be a dominant form of mechanical degradation in the lithium-sulfur cathode.

The second new method for fabricating functional materials, hydrogel infusion additive manufacturing (HIAM), is a simple and powerful method for fabricating a wide range of materials from a single resin system. We use a paradigm wherein printed organogels are subsequently infused with precursors, and then undergo chemical reactions to convert those precursors to desired functional materials. Using this versatile method, we fabricated a variety of materials including pure metals (Cu, Ni, Ag), homogenous alloys (CuNi), heterogenous alloys (CuAg), high entropy

alloys (CuNiCoFe), and refractory alloys (W-Ni). We additionally characterized these materials both structurally and chemically to understand how the energetic chemical reactions such as combustion inherent to the HIAM process affect the microstructures of produced parts. We reported how HIAM was optimized for the copper system, and how the principles from that system are generally applicable to many other materials, especially those with nitrate salt precursors. We investigated the unusual microstructural features, such as high annealing twin densities, that are typical of HIAM-derived metals, and the implications of these features on mechanical properties measured by nanoindentation. Ultimately, we showed that HIAM-derived Cu and CuNi are harder than predicted by the Hall-Petch relation, even when accounting for the presence of twin boundaries.

5.2 Thesis outlook

In the field of additive manufacturing, there are still many unsolved problems, but I believe they fall broadly into the following categories:

1. **Increasing resolution**: can we make it smaller?
2. **Increasing throughput**: can we make it faster/larger without sacrificing feature size?
3. **Developing new materials**: can we make useful new functional materials?
4. **Understanding and quantifying defects**: how can we be sure all AM materials behave as designed?
5. **Applications**: how can we use 3D-architected materials to improve performance in real-world situations?

5.2.1 3D batteries outlook

The field of 3D batteries is nascent, and doubtless many exciting advances will occur within the next several years. In our recently published perspective, Kai, Yuchun, Julia, and I reflected on what we have learned working on 3D batteries for the past several years [166]. As a field, I believe we have done a good job answering some of the specific technical challenges relating to fabricating 3D battery materials, and identifying some niche applications such as spacecraft which may benefit from multifunctional structural batteries that could be created via additive manufacturing. However, we have yet to see a commercially viable 3D printed battery, and the reality

of the situation is that battery manufacturing has become such a large-scale and established part of modern society that practical innovation will require simplifying or integrating with existing manufacturing processes. I doubt that conventional additive manufacturing, especially of the complex and deeply interesting structures that many of us are fond of, will ever find a place in the real-world manufacturing of batteries. This work still has value; the deterministic and predictable structures achievable via AM are useful tools for investigating fundamental questions about battery architecture: *if we could shape batteries arbitrarily, how should we?* I believe the most impactful research on 3D batteries will focus on using these systems as tools to understand broader questions about battery design, and to learn lessons that will be useful for commercial battery manufacturing. A potential example of this is the recent trend towards laser ablation of electrode materials [167], which seeks to implement a simpler and more scalable approach to large-area patterning, and recognizes the advantages of nonplanar battery geometry.

5.2.2 Hydrogel infusion additive manufacturing outlook

As described throughout this thesis, additive manufacturing of metals has a wide variety of applications, and has historically been a technically challenging endeavor. Commercial metal AM has been mainly limited to costly systems which use heat to define part shape. In contrast, hydrogel infusion additive manufacturing (HIAM) represents a much more accessible and versatile platform for creating 3D metals. I hope that other researchers will use the tools we have developed to 3D print new materials and follow their own paths of discovery and innovation. Developing and demonstrating this technique has been, without a doubt, the most enjoyable and engaging scientific project I have worked on. And it has been gratifying to see other members of the Greer group adopt HIAM as a tool in their journeys to make biomedical materials, magnetic materials, and more.

Yet, there is more to be done, and the questions keep unfolding. The submission of a paper, or of this thesis, are transitory milestones in a larger scientific endeavor, and I am excited to see how this research will evolve. The remaining questions about HIAM that I find most interesting are:

1. Can we predict metal ion incorporation based on the binding affinity of a specific metal ion for the polymer network?
2. What do microstructures of HIAM metals look like immediately after the combustion reaction finishes, without any annealing?

3. What other new materials can be made with this technique? Carbides, sulfides, esoteric alloys?

4. Can we create a model to solve the inverse design of HIAM parts by taking into account heat transport, mass transport, and chemical reactions during calcination and reduction?

These questions will likely prove to be fertile scientific ground, and will also be necessary in order for HIAM to be implemented at a commercial scale.

5.3 Thank you

Finally, dear reader, thank you for coming along on this journey with me, and thank you for your interest in this work. I hope you found in this thesis what you were looking for. A final message: within and beyond additive manufacturing, each of us has tools we can use to make the world a better place.
What are your tools, and what will you make?

REFERENCES

(1) Hummel, R. E., *Understanding Materials Science*; Springer New York: New York, NY, 1998, DOI: 10.1007/978-1-4757-2972-6.

(2) Katzir, S.; Lehner, C.; Renn, J., *Traditions and Transformations in the History of Quantum Physics*, 2010.

(3) Feldman, D. Polymer History. *Designed Monomers and Polymers* **2008**, *11*, 1–15, DOI: 10.1163/156855508X292383.

(4) Campbell-Kelly, M.; Aspray, W., *Computer: a history of the information machine*. 2nd ed; Sloan technology series; Westview Press: 2004.

(5) Ngo, T. D.; Kashani, A.; Imbalzano, G.; Nguyen, K. T.; Hui, D. Additive manufacturing (3D printing): A review of materials, methods, applications and challenges. *Composites Part B: Engineering* **2018**, *143*, 172–196, DOI: 10.1016/j.compositesb.2018.02.012.

(6) Ligon, S. C.; Liska, R.; Stampfl, J.; Gurr, M.; Mülhaupt, R. Polymers for 3D Printing and Customized Additive Manufacturing. *Chemical Reviews* **2017**, *117*, 10212–10290, DOI: 10.1021/acs.chemrev.7b00074.

(7) Daminabo, S. C.; Goel, S.; Grammatikos, S. A.; Nezhad, H. Y.; Thakur, V. K. Fused deposition modeling-based additive manufacturing (3D printing): techniques for polymer material systems. *Materials Today Chemistry* **2020**, *16*, 100248, DOI: 10.1016/j.mtchem.2020.100248.

(8) Lewis, J. A. Direct Ink Writing of 3D Functional Materials. *Advanced Functional Materials* **2006**, *16*, 2193–2204, DOI: 10.1002/adfm.200600434.

(9) Gülcan, O.; Günaydın, K.; Tamer, A. The state of the art of material jetting—a critical review. *Polymers* **2021**, *13*, DOI: 10.3390/polym13162829.

(10) Ziaee, M.; Crane, N. B. Binder jetting: A review of process, materials, and methods. *Additive Manufacturing* **2019**, *28*, 781–801, DOI: 10.1016/j.addma.2019.05.031.

(11) Pagac, M.; Hajnys, J.; Ma, Q. P.; Jancar, L.; Jansa, J.; Stefek, P.; Mesicek, J. A review of vat photopolymerization technology: Materials, applications, challenges, and future trends of 3d printing. *Polymers* **2021**, *13*, 1–20, DOI: 10.3390/polym13040598.

(12) Chatham, C. A.; Long, T. E.; Williams, C. B. A review of the process physics and material screening methods for polymer powder bed fusion additive manufacturing. *Progress in Polymer Science* **2019**, *93*, 68–95, DOI: 10.1016/j.progpolymsci.2019.03.003.

(13) King, W. E.; Anderson, A. T.; Ferencz, R. M.; Hodge, N. E.; Kamath, C.; Khairallah, S. A.; Rubenchik, A. M. Laser powder bed fusion additive manufacturing of metals; physics, computational, and materials challenges. *Applied Physics Reviews* **2015**, *2*, 041304, DOI: 10.1063/1.4937809.

(14) Dass, A.; Moridi, A. State of the Art in Directed Energy Deposition: From Additive Manufacturing to Materials Design. *Coatings* **2019**, *9*, 418, DOI: 10.3390/coatings9070418.

(15) Kodama, H. Automatic method for fabricating a three-dimensional plastic model with photo-hardening polymer. *Review of Scientific Instruments* **1981**, *52*, 1770–1773, DOI: 10.1063/1.1136492.

(16) Hull, C. W. Apparatus for Production of Three-Dmensonal Objects By Stereolithography. *Patent* **1984**, 16.

(17) Gibson, I.; Rosen, D.; Stucker, B., *Additive Manufacturing Technologies*; Springer New York: New York, NY, 2015, pp 63–106, DOI: 10.1007/978-1-4939-2113-3.

(18) Sun, C.; Fang, N.; Wu, D.; Zhang, X. Projection micro-stereolithography using digital micro-mirror dynamic mask. *Sensors and Actuators A: Physical* **2005**, *121*, 113–120, DOI: e.

(19) Tumbleston, J. R.; Shirvanyants, D.; Ermoshkin, N.; Janusziewicz, R.; Johnson, A. R.; Kelly, D.; Chen, K.; Pinschmidt, R.; Rolland, J. P.; Ermoshkin, A.; Samulski, E. T.; DeSimone, J. M. Continuous liquid interface production of 3D objects. *Science* **2015**, *347*, 1349–1352, DOI: 10.1126/science.aaa2397.

(20) Walker, D. A.; Hedrick, J. L.; Mirkin, C. A. Rapid, large-volume, thermally controlled 3D printing using a mobile liquid interface. *Science* **2019**, *366*, 360–364, DOI: 10.1126/science.aax1562.

(21) Lu, C.; Lipson, R. Interference lithography: a powerful tool for fabricating periodic structures. *Laser & Photonics Reviews* **2010**, *4*, 568–580, DOI: 10.1002/lpor.200810061.

(22) Kelly, B. E.; Bhattacharya, I.; Heidari, H.; Shusteff, M.; Spadaccini, C. M.; Taylor, H. K. Volumetric additive manufacturing via tomographic reconstruction. *Science* **2019**, *363*, 1075–1079, DOI: 10.1126/science.aau7114.

(23) Loterie, D.; Delrot, P.; Moser, C. High-resolution tomographic volumetric additive manufacturing. *Nature Communications* **2020**, *11*, 852, DOI: 10.1038/s41467-020-14630-4.

(24) Toombs, J. T.; Luitz, M.; Cook, C. C.; Jenne, S.; Li, C. C.; Rapp, B. E.; Kotz-Helmer, F.; Taylor, H. K. Volumetric additive manufacturing of silica glass with microscale computed axial lithography. *Science* **2022**, *376*, 308–312, DOI: 10.1126/science.abm6459.

(25) Norrish, R. G.; Bamford, C. H. Photo-decomposition of aldehydes and ketones. *Nature* **1937**, *140*, 195–196, DOI: 10.1038/140195b0.

(26) Herzberger, J.; Meenakshisundaram, V.; Williams, C. B.; Long, T. E. 3D Printing All-Aromatic Polyimides Using Stereolithographic 3D Printing of Polyamic Acid Salts. *ACS Macro Letters* **2018**, *7*, 493–497, DOI: 10.1021/acsmacrolett.8b00126.

(27) Zhang, B.; Li, S.; Hingorani, H.; Serjouei, A.; Larush, L.; Pawar, A. A.; Goh, W. H.; Sakhaei, A. H.; Hashimoto, M.; Kowsari, K.; Magdassi, S.; Ge, Q. Highly stretchable hydrogels for UV curing based high-resolution multimaterial 3D printing. *Journal of Materials Chemistry B* **2018**, *6*, 3246–3253, DOI: 10.1039/C8TB00673C.

(28) Zhang, D.; Liu, X.; Qiu, J. 3D printing of glass by additive manufacturing techniques: a review. *Frontiers of Optoelectronics* **2021**, *14*, 263–277, DOI: 10.1007/s12200-020-1009-z.

(29) Chen, Z.; Li, Z.; Li, J.; Liu, C.; Lao, C.; Fu, Y.; Liu, C.; Li, Y.; Wang, P.; He, Y. 3D printing of ceramics: A review. *Journal of the European Ceramic Society* **2019**, *39*, 661–687, DOI: 10.1016/j.jeurceramsoc.2018.11.013.

(30) Yee, D. W.; Greer, J. R. Three-dimensional chemical reactors: in situ materials synthesis to advance vat photopolymerization. *Polymer International* **2021**, *70*, 964–976, DOI: 10.1002/pi.6165.

(31) Corbel, S.; Dufaud, O.; Roques-Carmes, T., *Stereolithography*; Bártolo, P. J., Ed.; Springer US: Boston, MA, 2011, pp 141–159, DOI: 10.1007/978-0-387-92904-0.

(32) Nguyen, H. X.; Suen, H.; Poudel, B.; Kwon, P.; Chung, H. Development of an innovative, high speed, large-scaled, and affordable metal additive manufacturing process. *CIRP Annals* **2020**, *69*, 177–180, DOI: 10.1016/j.cirp.2020.04.069.

(33) Vyatskikh, A.; Delalande, S.; Kudo, A.; Zhang, X.; Portela, C. M.; Greer, J. R. Additive manufacturing of 3D nano-architected metals. *Nature Communications* **2018**, *9*, 593, DOI: 10.1038/s41467-018-03071-9.

(34) Oran, D.; Rodriques, S. G.; Gao, R.; Asano, S.; Skylar-Scott, M. A.; Chen, F.; Tillberg, P. W.; Marblestone, A. H.; Boyden, E. S. 3D nanofabrication by volumetric deposition and controlled shrinkage of patterned scaffolds. *Science* **2018**, *362*, 1281–1285, DOI: 10.1126/science.aau5119.

(35) Long, T. E.; Williams, C. B. Printing nanomaterials in shrinking gels. *Science* **2018**, *362*, 1244–1245, DOI: 10.1126/science.aav5712.

(36) Ambrosi, A.; Pumera, M. 3D-printing technologies for electrochemical applications. *Chemical Society Reviews* **2016**, *45*, 2740–2755, DOI: 10.1039/C5CS00714C.

(37) Pang, Y.; Cao, Y.; Chu, Y.; Liu, M.; Snyder, K.; MacKenzie, D.; Cao, C. Additive Manufacturing of Batteries. *Advanced Functional Materials* **2020**, *30*, 1906244, DOI: 10.1002/adfm.201906244.

(38) Chang, P.; Mei, H.; Zhou, S.; Dassios, K. G.; Cheng, L. 3D printed electrochemical energy storage devices. *Journal of Materials Chemistry A* **2019**, *7*, 4230–4258, DOI: 10.1039/c8ta11860d.

(39) Sun, K.; Wei, T. S.; Ahn, B. Y.; Seo, J. Y.; Dillon, S. J.; Lewis, J. A. 3D printing of interdigitated Li-ion microbattery architectures. *Advanced Materials* **2013**, *25*, 4539–4543, DOI: 10.1002/adma.201301036.

(40) Fu, K.; Wang, Y.; Yan, C.; Yao, Y.; Chen, Y.; Dai, J.; Lacey, S.; Wang, Y.; Wan, J.; Li, T.; Wang, Z.; Xu, Y.; Hu, L. Graphene Oxide-Based Electrode Inks for 3D-Printed Lithium-Ion Batteries. *Advanced Materials* **2016**, *28*, 2587–2594, DOI: 10.1002/adma.201505391.

(41) Ding, J.; Shen, K.; Du, Z.; Li, B.; Yang, S. 3D-Printed Hierarchical Porous Frameworks for Sodium Storage. *ACS Applied Materials and Interfaces* **2017**, *9*, 41871–41877, DOI: 10.1021/acsami.7b12892.

(42) Li, J.; Liang, X.; Liou, F.; Park, J. Macro-/Micro-Controlled 3D Lithium-Ion Batteries via Additive Manufacturing and Electric Field Processing. *Scientific Reports* **2018**, *8*, 1846, DOI: 10.1038/s41598-018-20329-w.

(43) Liu, J. et al. Pathways for practical high-energy long-cycling lithium metal batteries. *Nature Energy* **2019**, *4*, 180–186, DOI: 10.1038/s41560-019-0338-x.

(44) Shen, K.; Ding, J.; Yang, S. 3D Printing Quasi-Solid-State Asymmetric Micro-Supercapacitors with Ultrahigh Areal Energy Density. *Advanced Energy Materials* **2018**, 1800408, DOI: 10.1002/aenm.201800408.

(45) Gao, X.; Sun, Q.; Yang, X.; Liang, J.; Koo, A.; Li, W.; Liang, J.; Wang, J.; Li, R.; Holness, F. B.; Price, A. D.; Yang, S.; Sham, T.-K.; Sun, X. Toward a remarkable Li-S battery via 3D printing. *Nano Energy* **2019**, *56*, 595–603, DOI: 10.1016/j.nanoen.2018.12.001.

(46) Chen, C.; Jiang, J.; He, W.; Lei, W.; Hao, Q.; Zhang, X. 3D Printed High-Loading Lithium-Sulfur Battery Toward Wearable Energy Storage. *Advanced Functional Materials* **2020**, *30*, 1909469, DOI: 10.1002/adfm.201909469.

(47) Wei, T. S.; Ahn, B. Y.; Grotto, J.; Lewis, J. A. 3D Printing of Customized Li-Ion Batteries with Thick Electrodes. *Advanced Materials* **2018**, *30*, 1–7, DOI: 10.1002/adma.201703027.

(48) Shen, K.; Cao, Z.; Shi, Y.; Zhang, Y.; Li, B.; Yang, S. 3D Printing Lithium Salt towards Dendrite-free Lithium Anodes. *Energy Storage Materials* **2021**, *35*, 108–113, DOI: 10.1016/j.ensm.2020.11.022.

(49) Moser, S.; Kenel, C.; Wehner, L.; Spolenak, R.; Dunand, D. 3D ink-printed, sintered porous silicon scaffolds for battery applications. *Journal of Power Sources* **2021**, *507*, 230298, DOI: 10.1016/j.jpowsour.2021.230298.

(50) Ragones, H.; Menkin, S.; Kamir, Y.; Gladkikh, A.; Mukra, T.; Kosa, G.; Golodnitsky, D. Towards smart free form-factor 3D printable batteries. *Sustainable Energy and Fuels* **2018**, *2*, 1542–1549, DOI: 10.1039/c8se00122g.

(51) Maurel, A.; Grugeon, S.; Fleutot, B.; Courty, M.; Prashantha, K.; Tortajada, H.; Armand, M.; Panier, S.; Dupont, L. Three-Dimensional Printing of a LiFePO4/Graphite Battery Cell via Fused Deposition Modeling. *Scientific Reports* **2019**, *9*, 1–14, DOI: 10.1038/s41598-019-54518-y.

(52) Ragones, H.; Vinegrad, A.; Ardel, G.; Goor, M.; Kamir, Y.; Dorfman, M. M.; Gladkikh, A.; Golodnitsky, D. On the Road to a Multi-Coaxial-Cable Battery: Development of a Novel 3D-Printed Composite Solid Electrolyte. *Journal of The Electrochemical Society* **2020**, *167*, 070503, DOI: 10.1149/2.0032007jes.

(53) Reyes, C.; Somogyi, R.; Niu, S.; Cruz, M. A.; Yang, F.; Catenacci, M. J.; Rhodes, C. P.; Wiley, B. J. Three-Dimensional Printing of a Complete Lithium Ion Battery with Fused Filament Fabrication. *ACS Applied Energy Materials* **2018**, *1*, 5268–5279, DOI: 10.1021/acsaem.8b00885.

(54) Valera-Jiménez, J. F.; Pérez-Flores, J. C.; Castro-García, M.; Canales-Vázquez, J. Development of full ceramic electrodes for lithium-ion batteries via desktop-fused filament fabrication and further sintering. *Applied Materials Today* **2021**, *25*, DOI: 10.1016/j.apmt.2021.101243.

(55) Saccone, M. A.; Greer, J. R. Understanding and mitigating mechanical degradation in lithium–sulfur batteries: additive manufacturing of Li2S composites and nanomechanical particle compressions. *Journal of Materials Research* **2021**, *36*, 3656–3666, DOI: 10.1557/s43578-021-00182-w.

(56) Narita, K.; Citrin, M. A.; Yang, H.; Xia, X.; Greer, J. R. 3D Architected Carbon Electrodes for Energy Storage. *Advanced Energy Materials* **2021**, *11*, 1–13, DOI: 10.1002/aenm.202002637.

(57) Chen, Q.; Xu, R.; He, Z.; Zhao, K.; Pan, L. Printing 3D gel polymer electrolyte in lithium-ion microbattery using stereolithography. *Journal of the Electrochemical Society* **2017**, *164*, A1852–A1857, DOI: 10.1149/2.0651709jes.

(58) Acord, K. A.; Dupuy, A. D.; Scipioni Bertoli, U.; Zheng, B.; West, W. C.; Chen, Q. N.; Shapiro, A. A.; Schoenung, J. M. Morphology, microstructure, and phase states in selective laser sintered lithium ion battery cathodes. *Journal of Materials Processing Technology* **2021**, *288*, 116827, DOI: 10.1016/j.jmatprotec.2020.116827.

(59) Maurel, A.; Haukka, M.; MacDonald, E.; Kivijärvi, L.; Lahtinen, E.; Kim, H.; Armand, M.; Cayla, A.; Jamali, A.; Grugeon, S.; Dupont, L.; Panier, S. Considering lithium-ion battery 3D-printing via thermoplastic material extrusion and polymer powder bed fusion. *Additive Manufacturing* **2021**, *37*, DOI: 10.1016/j.addma.2020.101651.

(60) Shen, K.; Mei, H.; Li, B.; Ding, J.; Yang, S. 3D Printing Sulfur Copolymer-Graphene Architectures for Li-S Batteries. *Advanced Energy Materials* **2018**, *8*, 1701527, DOI: 10.1002/aenm.201701527.

(61) Gratson, G. M.; Lewis, J. A. Phase Behavior and Rheological Properties of Polyelectrolyte Inks for Direct-Write Assembly. **2005**, 457–464.

(62) Maurel, A.; Grugeon, S.; Armand, M.; Fleutot, B.; Courty, M.; Prashantha, K.; Davoisne, C.; Tortajada, H.; Panier, S.; Dupont, L. Overview on Lithium-Ion Battery 3D-Printing By Means of Material Extrusion. *ECS Meeting Abstracts* **2020**, *MA2020-02*, 3690–3690, DOI: 10.1149/MA2020-02693690mtgabs.

(63) Sha, J.; Li, Y.; Villegas Salvatierra, R.; Wang, T.; Dong, P.; Ji, Y.; Lee, S. K.; Zhang, C.; Zhang, J.; Smith, R. H.; Ajayan, P. M.; Lou, J.; Zhao, N.; Tour, J. M. Three-Dimensional Printed Graphene Foams. *ACS Nano* **2017**, *11*, 6860–6867, DOI: 10.1021/acsnano.7b01987.

(64) Maurel, A.; Martinez, A. C.; Grugeon, S.; Panier, S.; Dupont, L.; Cortes, P.; Sherrard, C. G.; Small, I.; Sreenivasan, S. T.; MacDonald, E. Toward High Resolution 3D Printing of Shape-Conformable Batteries via Vat Photopolymerization: Review and Perspective. *IEEE Access* **2021**, *9*, 140654–140666, DOI: 10.1109/ACCESS.2021.3119533.

(65) Yee, D. W.; Citrin, M. A.; Taylor, Z. W.; Saccone, M. A.; Tovmasyan, V. L.; Greer, J. R. Hydrogel-Based Additive Manufacturing of Lithium Cobalt Oxide. *Advanced Materials Technologies* **2021**, *6*, 2000791, DOI: 10.1002/admt.202000791.

(66) Cohen, E.; Menkin, S.; Lifshits, M.; Kamir, Y.; Gladkich, A.; Kosa, G.; Golodnitsky, D. Novel rechargeable 3D-Microbatteries on 3D-printed-polymer substrates: Feasibility study. *Electrochimica Acta* **2018**, *265*, 690–701, DOI: 10.1016/j.electacta.2018.01.197.

(67) Xia, X.; Afshar, A.; Yang, H.; Portela, C. M.; Kochmann, D. M.; Di Leo, C. V.; Greer, J. R. Electrochemically reconfigurable architected materials. *Nature* **2019**, *573*, 205–213, DOI: 10.1038/s41586-019-1538-z.

(68) Huggins, R. A., *Advanced Batteries*; Springer US: Boston, MA, 2009, pp 1–474, DOI: 10.1007/978-0-387-76424-5.

(69) Fan, F. Y.; Pan, M. S.; Lau, K. C.; Assary, R. S.; Woodford, W. H.; Curtiss, L. A.; Carter, W. C.; Chiang, Y.-M. Solvent Effects on Polysulfide Redox Kinetics and Ionic Conductivity in Lithium-Sulfur Batteries. *Journal of The*

Electrochemical Society **2016**, *163*, A3111–A3116, DOI: 10.1149/2.1181614jes.

(70) Wu, H.-L.; Huff, L. A.; Gewirth, A. A. In Situ Raman Spectroscopy of Sulfur Speciation in Lithium–Sulfur Batteries. *ACS Applied Materials & Interfaces* **2015**, *7*, 1709–1719, DOI: 10.1021/am5072942.

(71) Han, F.; Yue, J.; Fan, X.; Gao, T.; Luo, C.; Ma, Z.; Suo, L.; Wang, C. High-Performance All-Solid-State Lithium–Sulfur Battery Enabled by a Mixed-Conductive Li 2 S Nanocomposite. *Nano Letters* **2016**, *16*, 4521–4527, DOI: 10.1021/acs.nanolett.6b01754.

(72) Lee, C.-W.; Pang, Q.; Ha, S.; Cheng, L.; Han, S.-D.; Zavadil, K. R.; Gallagher, K. G.; Nazar, L. F.; Balasubramanian, M. Directing the Lithium–Sulfur Reaction Pathway via Sparingly Solvating Electrolytes for High Energy Density Batteries. *ACS Central Science* **2017**, *3*, 605–613, DOI: 10.1021/acscentsci.7b00123.

(73) Pang, Q.; Shyamsunder, A.; Narayanan, B.; Kwok, C. Y.; Curtiss, L. A.; Nazar, L. F. Tuning the electrolyte network structure to invoke quasi-solid state sulfur conversion and suppress lithium dendrite formation in Li–S batteries. *Nature Energy* **2018**, *3*, 783–791, DOI: 10.1038/s41560-018-0214-0.

(74) Dunn, B.; Kamath, H.; Tarascon, J. M. Electrical energy storage for the grid: A battery of choices. *Science* **2011**, *334*, 928–935, DOI: 10.1126/science.1212741.

(75) Bills, A.; Sripad, S.; Fredericks, W. L.; Singh, M.; Viswanathan, V. Performance Metrics Required of Next-Generation Batteries to Electrify Commercial Aircraft. *ACS Energy Letters* **2020**, *5*, 663–668, DOI: 10.1021/acsenergylett.9b02574.

(76) Cano, Z. P.; Banham, D.; Ye, S.; Hintennach, A.; Lu, J.; Fowler, M.; Chen, Z. Batteries and fuel cells for emerging electric vehicle markets. *Nature Energy* **2018**, *3*, 279–289, DOI: 10.1038/s41560-018-0108-1.

(77) Manthiram, A.; Fu, Y.; Chung, S. H.; Zu, C.; Su, Y. S. Rechargeable lithium-sulfur batteries, 2014, DOI: 10.1021/cr500062v.

(78) Mikhaylik, Y. V.; Akridge, J. R. Polysulfide Shuttle Study in the Li/S Battery System. *Journal of The Electrochemical Society* **2004**, *151*, A1969, DOI: 10.1149/1.1806394.

(79) Zhang, S. S. Liquid electrolyte lithium/sulfur battery: Fundamental chemistry, problems, and solutions. *Journal of Power Sources* **2013**, *231*, 153–162, DOI: 10.1016/j.jpowsour.2012.12.102.

(80) Bai, P.; Li, J.; Brushett, F. R.; Bazant, M. Z. Transition of lithium growth mechanisms in liquid electrolytes. *Energy and Environmental Science* **2016**, *9*, 3221–3229, DOI: 10.1039/c6ee01674j.

(81) Waluś, S.; Offer, G.; Hunt, I.; Patel, Y.; Stockley, T.; Williams, J.; Purkayastha, R. Volumetric expansion of Lithium-Sulfur cell during operation – Fundamental insight into applicable characteristics. *Energy Storage Materials* **2018**, *10*, 233–245, DOI: 10.1016/j.ensm.2017.05.017.

(82) Wild, M.; O'neill, L.; Zhang, T.; Purkayastha, R.; Minton, G.; Marinescu, M.; Offer, G. J. Lithium sulfur batteries, a mechanistic review. *Energy Environ. Sci* **2015**, *8*, 3477, DOI: 10.1039/c5ee01388g.

(83) Xu, R.; Lu, J.; Amine, K. Progress in Mechanistic Understanding and Characterization Techniques of Li-S Batteries. *Advanced Energy Materials* **2015**, *5*, 1500408, DOI: 10.1002/aenm.201500408.

(84) McDowell, M. T.; Xia, S.; Zhu, T. The mechanics of large-volume-change transformations in high-capacity battery materials. *Extreme Mechanics Letters* **2016**, *9*, 480–494, DOI: 10.1016/j.eml.2016.03.004.

(85) Zhang, Y.; Fincher, C.; McProuty, S.; Pharr, M. In-operando imaging of polysulfide catholytes for Li–S batteries and implications for kinetics and mechanical stability. *Journal of Power Sources* **2019**, *434*, 226727, DOI: 10.1016/J.JPOWSOUR.2019.226727.

(86) Zhang, Y.; Luo, Y.; Fincher, C.; McProuty, S.; Swenson, G.; Banerjee, S.; Pharr, M. In-situ measurements of stress evolution in composite sulfur cathodes. *Energy Storage Materials* **2019**, *16*, 491–497, DOI: 10.1016/j.ensm.2018.10.001.

(87) Li, W.; Zhang, Q.; Zheng, G.; Seh, Z. W.; Yao, H.; Cui, Y. Understanding the Role of Different Conductive Polymers in Improving the Nanostructured Sulfur Cathode Performance. *Nano Letters* **2013**, 2–4, DOI: 10.1021/nl403130h.

(88) Son, Y.; Lee, J.-S.; Son, Y.; Jang, J.-H.; Cho, J. Recent Advances in Lithium Sulfide Cathode Materials and Their Use in Lithium Sulfur Batteries. *Advanced Energy Materials* **2015**, *5*, 1500110, DOI: 10.1002/aenm.201500110.

(89) Shaibani, M.; Mirshekarloo, M. S.; Singh, R.; Easton, C. D.; Dilusha Cooray, M. C.; Eshraghi, N.; Abendroth, T.; Dörfler, S.; Althues, H.; Kaskel, S.; Hollenkamp, A. F.; Hill, M. R.; Majumder, M. Expansion-tolerant architectures for stable cycling of ultrahigh-loading sulfur cathodes in lithium-sulfur batteries. *Science Advances* **2020**, *6*, DOI: 10.1126/sciadv.aay2757.

(90) Izumi, A.; Sanada, M.; Furuichi, K.; Teraki, K.; Matsuda, T.; Hiramatsu, K.; Munakata, H.; Kanamura, K. Development of high capacity lithium-ion battery applying three-dimensionally patterned electrode. *Electrochimica Acta* **2012**, *79*, 218–222, DOI: 10.1016/j.electacta.2012.07.001.

(91) Cooperstein, I.; Layani, M.; Magdassi, S. 3D printing of porous structures by UV-curable O/W emulsion for fabrication of conductive objects. *Journal of Materials Chemistry C* **2015**, *3*, 2040–2044, DOI: 10.1039/C4TC02215G.

(92) Ying, G. L.; Jiang, N.; Maharjan, S.; Yin, Y. X.; Chai, R. R.; Cao, X.; Yang, J. Z.; Miri, A. K.; Hassan, S.; Zhang, Y. S. Aqueous Two-Phase Emulsion Bioink-Enabled 3D Bioprinting of Porous Hydrogels. *Advanced Materials* **2018**, *30*, 1805460, DOI: 10.1002/adma.201805460.

(93) Wang, D.-W.; Zeng, Q.; Zhou, G.; Yin, L.; Li, F.; Cheng, H.-M.; Gentle, I. R.; Lu, G. Q. M. Carbon–sulfur composites for Li–S batteries: status and prospects. *Journal of Materials Chemistry A* **2013**, *1*, 9382, DOI: 10.1039/c3ta11045a.

(94) Ye, F.; Noh, H.; Lee, J.; Lee, H.; Kim, H. T. Li2S/carbon nanocomposite strips from a lowerature conversion of Li2SO4as high-performance lithium-sulfur cathodes. *Journal of Materials Chemistry A* **2018**, *6*, 6617–6624, DOI: 10.1039/c8ta00515j.

(95) Lifshitz, I. M.; Slyozov, V. V. The kinetics of precipitation from supersaturated solid solutions. *Journal of Physics and Chemistry of Solids* **1961**, *19*, 35–50, DOI: 10.1016/0022-3697(61)90054-3.

(96) Park, H.; Koh, H. S.; Siegel, D. J. First-Principles Study of Redox End Members in Lithium–Sulfur Batteries. *The Journal of Physical Chemistry C* **2015**, *119*, 4675–4683, DOI: 10.1021/jp513023v.

(97) Li, W.; Yao, H.; Yan, K.; Zheng, G.; Liang, Z.; Chiang, Y.-M.; Cui, Y. The synergetic effect of lithium polysulfide and lithium nitrate to prevent lithium dendrite growth. *Nature Communications* **2015**, *6*, 7436, DOI: 10.1038/ncomms8436.

(98) Zhang, G.; Zhang, Z.-W.; Peng, H.-J.; Huang, J.-Q.; Zhang, Q. A Toolbox for Lithium-Sulfur Battery Research: Methods and Protocols. *Small Methods* **2017**, *1*, 1700134, DOI: 10.1002/smtd.201700134.

(99) Vizintin, A.; Chabanne, L.; Tchernychova, E.; Arčon, I.; Stievano, L.; Aquilanti, G.; Antonietti, M.; Fellinger, T.-P.; Dominko, R. The mechanism of Li2S activation in lithium-sulfur batteries: Can we avoid the polysulfide formation? *Journal of Power Sources* **2017**, *344*, 208–217, DOI: 10.1016/j.jpowsour.2017.01.112.

(100) Jiang, J.; Fan, Q.; Chou, S.; Guo, Z.; Konstantinov, K.; Liu, H.; Wang, J. Li2S-Based Li-Ion Sulfur Batteries: Progress and Prospects. *Small* **2019**, *1903934*, 1–24, DOI: 10.1002/smll.201903934.

(101) Paul, J.; Romeis, S.; Tomas, J.; Peukert, W. A review of models for single particle compression and their application to silica microspheres. *Advanced Powder Technology* **2014**, *25*, 136–153, DOI: 10.1016/j.apt.2013.09.009.

(102) Popov, V. L. In *Contact Mechanics and Friction*; Springer Berlin Heidelberg: Berlin, Heidelberg, 2010, pp 133–154, DOI: 10.1007/978-3-642-10803-7{_}10.

(103) De Jong, M.; Chen, W.; Angsten, T.; Jain, A.; Notestine, R.; Gamst, A.; Sluiter, M.; Ande, C. K.; Van Der Zwaag, S.; Plata, J. J.; Toher, C.; Curtarolo, S.; Ceder, G.; Persson, K. A.; Asta, M. Charting the complete elastic properties of inorganic crystalline compounds. *Scientific Data* **2015**, *2*, DOI: 10.1038/sdata.2015.9.

(104) Li, Z.; Zhou, Y.; Wang, Y.; Lu, Y. C. Solvent-Mediated Li2S Electrodeposition: A Critical Manipulator in Lithium–Sulfur Batteries. *Advanced Energy Materials* **2019**, *9*, 1802207, DOI: 10.1002/aenm.201802207.

(105) Sakuda, A.; Hayashi, A.; Tatsumisago, M. Sulfide solid electrolyte with favorable mechanical property for all-solid-state lithium battery. *Scientific Reports* **2013**, *3*, 2261, DOI: 10.1038/srep02261.

(106) Saccone, M. A.; Gallivan, R. A.; Narita, K.; Yee, D. W.; Greer, J. R. Microscale fabrication of 3D multicomponent metals via hydrogel infusion. *in review* **2022**.

(107) Vafadar, A.; Guzzomi, F.; Rassau, A.; Hayward, K. Advances in Metal Additive Manufacturing: A Review of Common Processes, Industrial Applications, and Current Challenges. *Applied Sciences* **2021**, *11*, 1213, DOI: 10.3390/app11031213.

(108) Sames, W. J.; List, F. A.; Pannala, S.; Dehoff, R. R.; Babu, S. S. The metallurgy and processing science of metal additive manufacturing. *International Materials Reviews* **2016**, *61*, 315–360, DOI: 10.1080/09506608.2015.1116649.

(109) Gisario, A.; Kazarian, M.; Martina, F.; Mehrpouya, M. Metal additive manufacturing in the commercial aviation industry: A review. *Journal of Manufacturing Systems* **2019**, *53*, 124–149, DOI: 10.1016/j.jmsy.2019.08.005.

(110) Mohd Yusuf, S.; Cutler, S.; Gao, N. Review: The Impact of Metal Additive Manufacturing on the Aerospace Industry. *Metals* **2019**, *9*, 1286, DOI: 10.3390/met9121286.

(111) Leal, R.; Barreiros, F. M.; Alves, L.; Romeiro, F.; Vasco, J. C.; Santos, M.; Marto, C. Additive manufacturing tooling for the automotive industry. *The International Journal of Advanced Manufacturing Technology* **2017**, *92*, 1671–1676, DOI: 10.1007/s00170-017-0239-8.

(112) Mantovani, S.; Barbieri, S.; Giacopini, M.; Croce, A.; Sola, A.; Bassoli, E. Synergy between topology optimization and additive manufacturing in the automotive field. *Proceedings of the Institution of Mechanical Engineers, Part B: Journal of Engineering Manufacture* **2021**, *235*, 555–567, DOI: 10.1177/0954405420949209.

(113) Wu, S.-H.; Li, Y.; Zhang, Y.-Q.; Li, X.-K.; Yuan, C.-F.; Hao, Y.-L.; Zhang, Z.-Y.; Guo, Z. Porous Titanium-6 Aluminum-4 Vanadium Cage Has Better Osseointegration and Less Micromotion Than a Poly-Ether-Ether-Ketone

Cage in Sheep Vertebral Fusion: Porous Ti Cage has Better Osseointegration than PEEK. *Artificial Organs* **2013**, *37*, E191–E201, DOI: 10.1111/aor.12153.

(114) Ahangar, P.; Cooke, M. E.; Weber, M. H.; Rosenzweig, D. H. Current Biomedical Applications of 3D Printing and Additive Manufacturing. *Applied Sciences* **2019**, *9*, 1713, DOI: 10.3390/app9081713.

(115) Attaran, M. The rise of 3-D printing: The advantages of additive manufacturing over traditional manufacturing. *Business Horizons* **2017**, *60*, 677–688, DOI: 10.1016/j.bushor.2017.05.011.

(116) Laureijs, R. E.; Roca, J. B.; Narra, S. P.; Montgomery, C.; Beuth, J. L.; Fuchs, E. R. H. Metal Additive Manufacturing: Cost Competitive Beyond Low Volumes. *Journal of Manufacturing Science and Engineering* **2017**, *139*, 81010, DOI: 10.1115/1.4035420.

(117) Plocher, J.; Panesar, A. Review on design and structural optimisation in additive manufacturing: Towards next-generation lightweight structures. *Materials & Design* **2019**, *183*, 108164, DOI: 10.1016/j.matdes.2019.108164.

(118) Floreano, D.; Wood, R. J. Science, technology and the future of small autonomous drones. *Nature* **2015**, *521*, 460–466, DOI: 10.1038/nature14542.

(119) Middlemiss, R. P.; Samarelli, A.; Paul, D. J.; Hough, J.; Rowan, S.; Hammond, G. D. Measurement of the Earth tides with a MEMS gravimeter. *Nature* **2016**, *531*, 614–617, DOI: 10.1038/nature17397.

(120) Aboulkhair, N. T.; Simonelli, M.; Parry, L.; Ashcroft, I.; Tuck, C.; Hague, R. 3D printing of Aluminium alloys: Additive Manufacturing of Aluminium alloys using selective laser melting. *Progress in Materials Science* **2019**, *106*, 100578, DOI: 10.1016/j.pmatsci.2019.100578.

(121) Liu, Z.; He, B.; Lyu, T.; Zou, Y. A Review on Additive Manufacturing of Titanium Alloys for Aerospace Applications: Directed Energy Deposition and Beyond Ti-6Al-4V. *JOM* **2021**, *73*, 1804–1818, DOI: 10.1007/s11837-021-04670-6.

(122) Martin, J. H.; Yahata, B. D.; Hundley, J. M.; Mayer, J. A.; Schaedler, T. A.; Pollock, T. M. 3D printing of high-strength aluminium alloys. *Nature* **2017**, *549*, 365–369, DOI: 10.1038/nature23894.

(123) Svetlizky, D.; Das, M.; Zheng, B.; Vyatskikh, A. L.; Bose, S.; Bandyopadhyay, A.; Schoenung, J. M.; Lavernia, E. J.; Eliaz, N. Directed energy deposition (DED) additive manufacturing: Physical characteristics, defects, challenges and applications. *Materials Today* **2021**, S1369702121001139, DOI: 10.1016/j.mattod.2021.03.020.

(124) Bartlett, J. L.; Li, X. An overview of residual stresses in metal powder bed fusion. *Additive Manufacturing* **2019**, *27*, 131–149, DOI: 10.1016/j.addma.2019.02.020.

(125) Sanchez, S.; Smith, P.; Xu, Z.; Gaspard, G.; Hyde, C. J.; Wits, W. W.; Ashcroft, I. A.; Chen, H.; Clare, A. T. Powder Bed Fusion of nickel-based superalloys: A review. *International Journal of Machine Tools and Manufacture* **2021**, *165*, 103729, DOI: 10.1016/j.ijmachtools.2021.103729.

(126) Bajaj, P.; Hariharan, A.; Kini, A.; Kürnsteiner, P.; Raabe, D.; Jägle, E. A. Steels in additive manufacturing: A review of their microstructure and properties. *Materials Science and Engineering: A* **2020**, *772*, 138633, DOI: 10.1016/j.msea.2019.138633.

(127) Jadhav, S. D.; Dhekne, P. P.; Dadbakhsh, S.; Kruth, J.-P.; Van Humbeeck, J.; Vanmeensel, K. Surface Modified Copper Alloy Powder for Reliable Laser-based Additive Manufacturing. *Additive Manufacturing* **2020**, *35*, 101418, DOI: 10.1016/j.addma.2020.101418.

(128) Robinson, J.; Stanford, M.; Arjunan, A. Stable formation of powder bed laser fused 99.9% silver. *Materials Today Communications* **2020**, *24*, 101195, DOI: 10.1016/j.mtcomm.2020.101195.

(129) Kajtaz, M.; Subic, A.; Brandt, M.; Leary, M. In *Materials in Sports Equipment*; Elsevier: 2019, pp 161–198.

(130) Unkovskiy, A.; Schmidt, F.; Beuer, F.; Li, P.; Spintzyk, S.; Kraemer Fernandez, P. Stereolithography vs. Direct Light Processing for Rapid Manufacturing of Complete Denture Bases: An In Vitro Accuracy Analysis. *Journal of Clinical Medicine* **2021**, *10*, 1070, DOI: 10.3390/jcm10051070.

(131) Manoj, A.; Bhuyan, M.; Raj Banik, S.; Ravi Sankar, M. 3D printing of nasopharyngeal swabs for COVID-19 diagnose: Past and current trends. *Materials Today: Proceedings* **2021**, *44*, 1361–1368, DOI: 10.1016/j.matpr.2020.11.505.

(132) Mooraj, S.; Welborn, S. S.; Jiang, S.; Peng, S.; Fu, J.; Baker, S.; Duoss, E. B.; Zhu, C.; Detsi, E.; Chen, W. Three-dimensional hierarchical nanoporous copper via direct ink writing and dealloying. *Scripta Materialia* **2020**, *177*, 146–150, DOI: 10.1016/j.scriptamat.2019.10.013.

(133) Miyanaji, H.; Ma, D.; Atwater, M. A.; Darling, K. A.; Hammond, V. H.; Williams, C. B. Binder jetting additive manufacturing of copper foam structures. *Additive Manufacturing* **2020**, *32*, 100960, DOI: 10.1016/j.addma.2019.100960.

(134) Zhang, K.; Meng, Q.; Cai, N.; Qu, Z.; He, R. Effects of solid loading on stereolithographic additive manufactured ZrO2 ceramic: A quantitative defect study by X-ray computed tomography. *Ceramics International* **2021**, *47*, 24353–24359, DOI: 10.1016/j.ceramint.2021.05.149.

(135) Yee, D. W.; Lifson, M. L.; Edwards, B. W.; Greer, J. R. Additive Manufacturing of 3D-Architected Multifunctional Metal Oxides. *Advanced Materials* **2019**, *31*, 1–9, DOI: 10.1002/adma.201901345.

(136) Deshpande, V.; Ashby, M.; Fleck, N. Foam topology: bending versus stretching dominated architectures. *Acta Materialia* **2001**, *49*, 1035–1040, DOI: 10.1016/S1359-6454(00)00379-7.

(137) Rasband, W. ImageJ, Bethesda, Maryland, USA.

(138) Beyerlein, I. J.; Zhang, X.; Misra, A. Growth twins and deformation twins in metals. *Annual Review of Materials Research* **2014**, *44*, DOI: 10.1146/annurev-matsci-070813-113304.

(139) Roy, B.; Das, J. Strengthening face centered cubic crystals by annealing induced nano-twins. *Scientific Reports* **2017**, *7*, 1–8, DOI: 10.1038/s41598-017-17848-3.

(140) Bansal, S.; Toimil-Molares, E.; Saxena, A.; Tummala, R. R. Nanoindentation of single crystal and polycrystalline copper nanowires. *Proceedings - Electronic Components and Technology Conference* **2005**, *1*, 71–76, DOI: 10.1109/ectc.2005.1441248.

(141) Emeis, F.; Peterlechner, M.; Divinski, S. V.; Wilde, G. Grain boundary engineering parameters for ultrafine grained microstructures: Proof of principles by a systematic composition variation in the Cu-Ni system. *Acta Materialia* **2018**, *150*, 262–272, DOI: 10.1016/j.actamat.2018.02.054.

(142) Chang, S. Y.; Chang, T. K. Grain size effect on nanomechanical properties and deformation behavior of copper under nanoindentation test. *Journal of Applied Physics* **2007**, *101*, DOI: 10.1063/1.2432873.

(143) Sari, N.; Kahraman, E.; Sari, B.; Özgün, A. Synthesis of some polymer-metal complexes and elucidation of their structures. *Journal of Macromolecular Science, Part A: Pure and Applied Chemistry* **2006**, *43*, 1227–1235, DOI: 10.1080/10601320600737484.

(144) L'vov, B. V. Kinetics and mechanism of thermal decomposition of silver oxide. *Thermochimica Acta* **1999**, *333*, 13–19, DOI: 10.1016/S0040-6031(99)00085-4.

(145) Bahari, Z.; Elgadi, M.; Rivet, J.; Dugué, J. Experimental study of the ternary Ag-Cu-In phase diagram. *Journal of Alloys and Compounds* **2009**, *477*, 152–165, DOI: 10.1016/j.jallcom.2008.10.030.

(146) Gun'ko, V. M.; Savina, I. N.; Mikhalovsky, S. V. Properties of water bound in hydrogels. *Gels* **2017**, *3*, DOI: 10.3390/gels3040037.

(147) Danks, A. E.; Hall, S. R.; Schnepp, Z. The evolution of 'sol–gel' chemistry as a technique for materials synthesis. *Materials Horizons* **2016**, *3*, 91–112, DOI: 10.1039/C5MH00260E.

(148) Moore, J. J.; Feng, H. J. Combustion synthesis of advanced materials: Part I. Reaction parameters. *Progress in Materials Science* **1995**, *39*, 243–273, DOI: 10.1016/0079-6425(94)00011-5.

(149) Hall, E. O. The deformation and ageing of mild steel: III Discussion of results. *Proceedings of the Physical Society. Section B* **1951**, *64*, 747–753, DOI: 10.1088/0370-1301/64/9/303.

(150) Cordero, Z. C.; Knight, B. E.; Schuh, C. A. Six decades of the Hall–Petch effect – a survey of grain-size strengthening studies on pure metals. *International Materials Reviews* **2016**, *61*, 495–512, DOI: 10.1080/09506608.2016.1191808.

(151) Lu, L.; Shen, Y.; Chen, X.; Qian, L.; Lu, K. Ultrahigh Strength and High Electrical Conductivity in Copper. *Science* **2004**, *304*, 422–426, DOI: 10.1126/science.1092905.

(152) Pande, C.; Rath, B.; Imam, M. Effect of annealing twins on Hall–Petch relation in polycrystalline materials. *Materials Science and Engineering: A* **2004**, *367*, 171–175, DOI: 10.1016/j.msea.2003.09.100.

(153) Wang, C.; Hossain Bhuiyan, M. E.; Moreno, S.; Minary-Jolandan, M. Direct-Write Printing Copper-Nickel (Cu/Ni) Alloy with Controlled Composition from a Single Electrolyte Using Co-Electrodeposition. *ACS Applied Materials and Interfaces* **2020**, *12*, 18683–18691, DOI: 10.1021/acsami.0c01100.

(154) Bahr, D. F.; Vasquez, G. Effect of solid solution impurities on dislocation nucleation during nanoindentation. *Journal of Materials Research* **2005**, *20*, 1947–1951, DOI: 10.1557/JMR.2005.0244.

(155) Bahl, S.; Mishra, S.; Yazar, K. U.; Kola, I. R.; Chatterjee, K.; Suwas, S. Non-equilibrium microstructure, crystallographic texture and morphological texture synergistically result in unusual mechanical properties of 3D printed 316L stainless steel. *Additive Manufacturing* **2019**, *28*, 65–77, DOI: 10.1016/j.addma.2019.04.016.

(156) Ye, Y. F.; Wang, Q.; Lu, J.; Liu, C. T.; Yang, Y. High-entropy alloy: challenges and prospects, 2016, DOI: 10.1016/j.mattod.2015.11.026.

(157) Müller, A. v.; Schlick, G.; Neu, R.; Anstätt, C.; Klimkait, T.; Lee, J.; Pascher, B.; Schmitt, M.; Seidel, C. Additive manufacturing of pure tungsten by means of selective laser beam melting with substrate preheating temperatures up to 1000 C. *Nuclear Materials and Energy* **2019**, *19*, 184–188, DOI: 10.1016/j.nme.2019.02.034.

(158) Calvo, M.; Jakus, A. E.; Shah, R. N.; Spolenak, R.; Dunand, D. C. Microstructure and Processing of 3D Printed Tungsten Microlattices and Infiltrated W-Cu Composites. *Advanced Engineering Materials* **2018**, *20*, 1800354, DOI: 10.1002/adem.201800354.

(159) Hunyadi, D.; Sajó, I.; Szilágyi, I. M. Structure and thermal decomposition of ammonium metatungstate. *Journal of Thermal Analysis and Calorimetry* **2014**, *116*, 329–337, DOI: 10.1007/s10973-013-3586-1.

(160) Wang, X.; Guo, W.; Abu-Reziq, R.; Magdassi, S. High-Complexity WO3-Based Catalyst with Multi-Catalytic Species via 3D Printing. *Catalysts* **2020**, *10*, 840, DOI: 10.3390/catal10080840.

(161) Bandyopadhyay, A.; Zhang, Y.; Bose, S. Recent developments in metal additive manufacturing. *Current Opinion in Chemical Engineering* **2020**, *28*, 96–104, DOI: 10.1016/j.coche.2020.03.001.

(162) Skylar-Scott, M. A.; Mueller, J.; Visser, C. W.; Lewis, J. A. Voxelated soft matter via multimaterial multinozzle 3D printing. *Nature* **2019**, *575*, 330–335, DOI: 10.1038/s41586-019-1736-8.

(163) Sampson, K. L.; Deore, B.; Go, A.; Nayak, M. A.; Orth, A.; Gallerneault, M.; Malenfant, P. R.; Paquet, C. Multimaterial Vat Polymerization Additive Manufacturing. *ACS Applied Polymer Materials* **2021**, *3*, 4304–4324, DOI: 10.1021/acsapm.1c00262.

(164) Dudukovic, N. A.; Fong, E. J.; Gemeda, H. B.; DeOtte, J. R.; Cerón, M. R.; Moran, B. D.; Davis, J. T.; Baker, S. E.; Duoss, E. B. Cellular fluidics. *Nature* **2021**, *595*, 58–65, DOI: 10.1038/s41586-021-03603-2.

(165) Senkov, O. N.; Miracle, D. B.; Chaput, K. J.; Couzinie, J. P. Development and exploration of refractory high entropy alloys - A review. *Journal of Materials Research* **2018**, *33*, 3092–3128, DOI: 10.1557/jmr.2018.153.

(166) Narita, K.; Saccone, M. A.; Sun, Y.; Greer, J. R. Additive manufacturing of 3D batteries: a perspective. *Journal of Materials Research* **2022**, DOI: 10.1557/s43578-022-00562-w.

(167) Lin, Z.; Shen, S.; Wang, Z.; Zhong, W. Laser ablation in air and its application in catalytic water splitting and Li-ion battery. *iScience* **2021**, *24*, 102469, DOI: 10.1016/j.isci.2021.102469.

Postdoc Blues

Appendix A

APPENDIX

A.1 Chapter 2 Appendix

Component	Amount	Purpose
Allnex Ebecryl 8210	39.776%	Oligomer: Aliphatic urethane acrylate
Sartomer SR 494 LM	39.776%	Oligomer: Lower viscosity acrylate
Rahn Genomer 1122	19.888%	Reactive diluent: Reduces viscosity
Esstech TPO+	0.400%	Photoinitiator
Mayzo OB+	0.160%	UV blocker

Table A.1: **PR-48 photopolymer resin formulation.** Amounts and purposes of the components of PR-48 photopolymer resin. All percentages are wt/wt.

Setting	Value	Explanation
Layer thickness	25 µ	Standard
First layer exposure	9 sec	High exposure adheres resin to build head
Burn in layer exposure	5.25 sec	Higher than standard
Model layer exposure	4.75 sec	Higher than standard
Z lift	750 µ	Standard
Tray rotation speed	3 rpm	Slowed to reduce shearing forces

Table A.2: **Print settings.** Print settings for Autodesk Ember SLA for use with cloudy emulsion based resins. These settings are designed to enable printing of structures with a feature size of 120 µṪhe main differences from standard settings are higher exposure times, which are needed to cure the cloudy resin, and a slower tray rotation speed, which is needed to prevent shearing off of small features

A.1.1 Lithium sulfide precursor resins

For resins made with Li_2S precursor, Li_2S was purchased from Alfa Aesar and stored in a glovebox under argon. Standard Clear PR-48 (PR-48) prototyping resin, an acrylate photopolymer resin, was purchased from Colorado Photopolymer Solutions. The components of PR-48 are described in Table A.1. Immediately prior to mixing resins, the desired amount of Li_2S was massed in the glovebox and removed from the glovebox in a sealed vial. To this sealed vial a pre-massed amount of PR-48 was added, and then the vial was quickly re-sealed, followed by vigorous mixing. The resulting solution/suspension was opaque and light yellow in color.

Resins prepared using this method resulted in a thick yellow homogeneous suspension (Fig. A.1a). Upon irradiation with ultraviolet (405 nm) light, the photopolymer resin was cured into a chip (Fig. A.1b). The resin mixing and curing process was carried out as quickly as possible in air, but there was inevitable hydrolysis where the Li_2S composite was exposed to air. After curing the composite, it was quickly cut in half and transfered to a Kapton tape XRD enclosure. The XRD spectrum (Fig. A.1c) shows the presence of crystalline Li_2S and the absence of the hydrolysis product LiOH. The peaks at 12° and 12.75° 2θ are background from the clay putty, while the broad peak around 20° 2θ is background from the Kapton tape (see Appedix Fig. A.2).

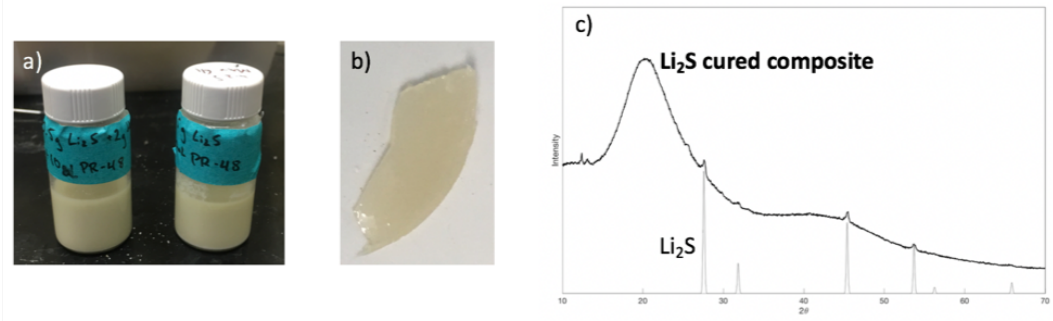

Figure A.1: **Li_2S precursor resin process.** (a) solutions of Li_2S in PR-48, (b) a UV-cured Li_2S composite chip, (c) XRD spectrum showing the presence of crystalline Li_2S (intensity units arbitrary)

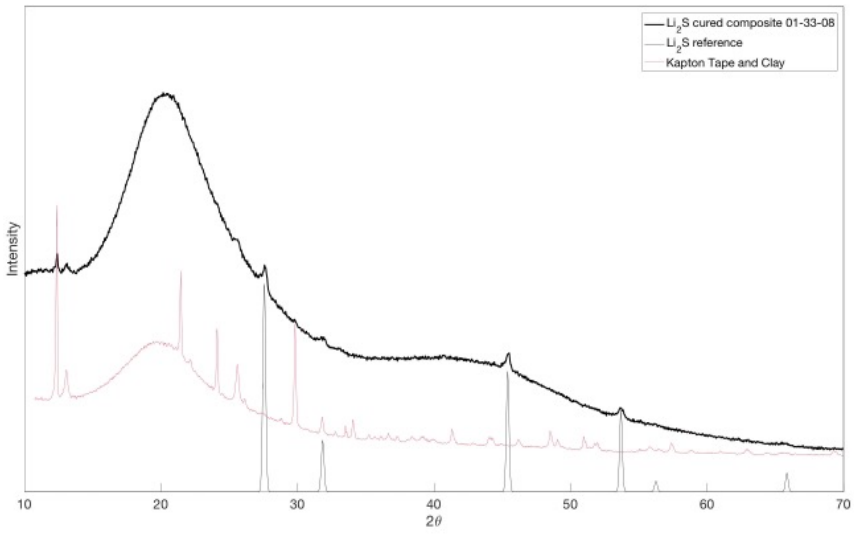

Figure A.2: **Kapton tape and clay reference XRD pattern.** XRD pattern of Kapton tape and clay matches with background peaks in curedLi_2S sample.

Fabricating Li_2S composites with Li_2S precursors has several limitations. As discussed earlier, some hydrolysis is inevitable since the process involves working with Li_2S in air. It is not possible to circumvent this problem by performing all processing and printing steps inside of a glovebox filled with an inert gas. In addition to being impractical, printing inside a glovebox would not work because the DLP 3D printing process requires the presence of O_2 to inhibit polymerization on the transparent window. Additionally, there is no way to control the size or morphology of the deposited Li_2S particles. A more ideal fabrication procedure would involve working with an air-stable compound during the resin mixing and 3D printing steps.

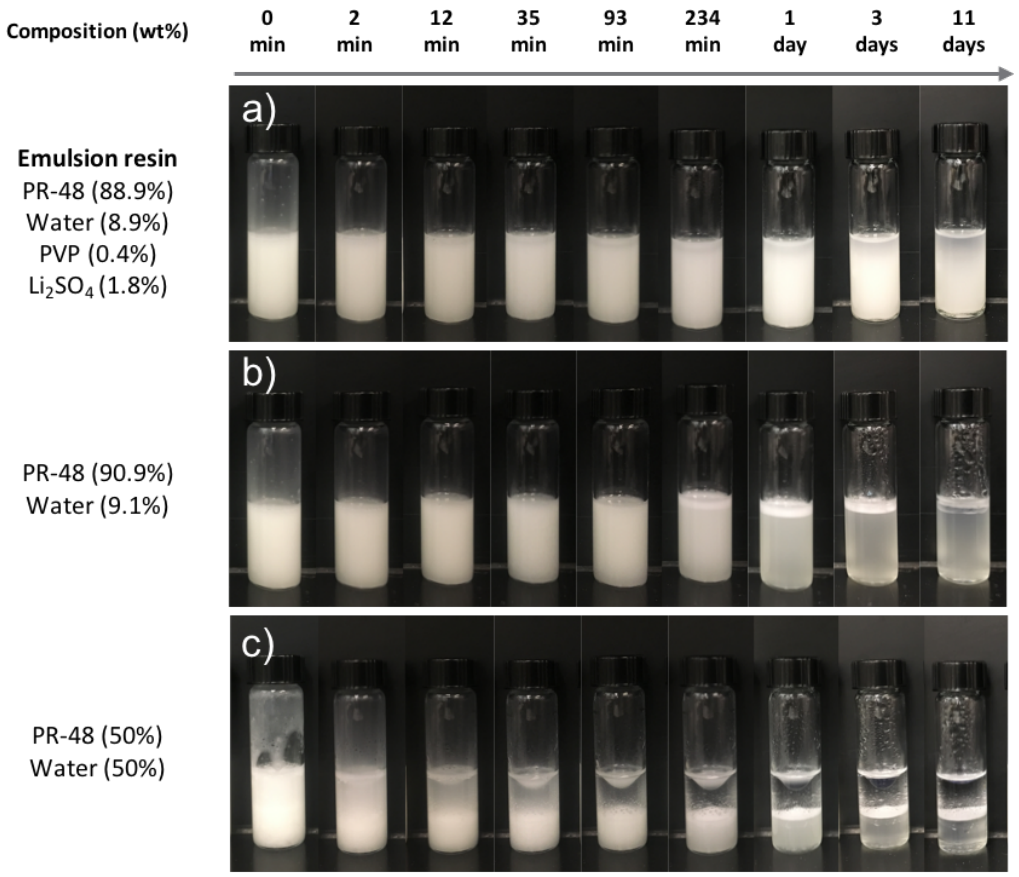

Figure A.3: **Time lapse of resin settling.** (a) Emulsion resin used in this work with photopolymer oil phase and $Li_2SO_4 \cdot H_2O$ salt solution water phase stabilized by PVP surfactant. (b) Mixture of water and photopolymer resin in a similar ratio without surfactant or salt. (c) 50/50 wt% mixture of water and photopolymer resin.

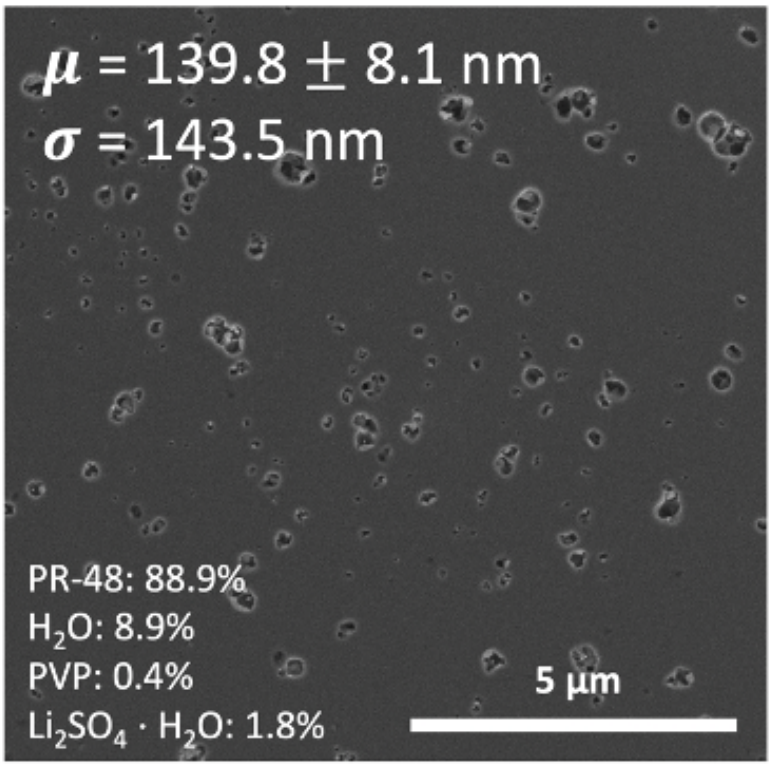

Figure A.4: **Porosity distribution from emulsion stereolithography with lower surfactant loading.** Porosity distribution for a resin variant with lower surfactant and salt loadings than the resin used in the main work. The average pore size of 139.8 ± 8.1 nm and standard deviation of 143.5 nm resulting from the low-surfactant resin are larger than the average pore size and standard deviation for the high-surfactant resin.

A.2 Chapter 3 Appendix

A.2.1 Twin boundary-induced hardening

Following a framework outlined by Pande et al. [152], we added a correction to the classical Hall-Petch relationship (which considers the effect of grain boundaries to block dislocation motion) to account for the ability of twins to act as additional dislocation barriers. We used this statistical relationship to calculate an estimated average hardness.

The Hall-Petch effect can be explained by scaling the relative length between a dislocation and boundary which impedes its ability to effect plastic deformation. Twin boundaries act as barriers to dislocation motion, though they generally contribute a lower energetic barrier compared to grain boundaries.

We account for the addition of these twin boundaries in the Hall-Petch relationship by creating an effective grain size, D_{eff}, that incorporates the reduced distance between barriers. This is done by dividing the measured grain size, D, by the number of boundaries in a grain:

$$D_{eff} = \frac{D}{1 + pN} \tag{A.1}$$

where N is the number of twin boundaries, and p is a scaling term representative of the effective strength (ability to impede dislocation motion) of a twin boundary relative to a grain boundary. The scaling term, p, allows for proportional weighting of the twin boundary's relative participation in the material's hardening. The value of p ranges from 0 to 1 with a value of 0 meaning there is no resistance to dislocation motion and a value of 1 giving equal resistance to a grain boundary. This relationship assumes that each boundary is isolated and all interactions are independent (i.e., no interaction or effects felt from other boundaries in grain). The 1 added to the $p * N$ term accounts for the standard grain boundary and can be seen when $p = 0$ as the equation reduces to $D_{eff} = D$, recovering the classic Hall-Petch relationship.

Thus, the Hall-Petch prediction of hardness for a material with twin boundaries can be written as

$$H = H_0 + kD_{eff}^{-1/2} \tag{A.2}$$

or

$$H = H_0 + k\frac{D}{1 + pN}^{-1/2}. \tag{A.3}$$

To establish a clear upper-bound for the hardness contribution of isolated twin boundaries, the twin boundaries are set to have the same resistance as a grain boundary ($p = 1$).

A.3 Chapter 4 Appendix

Material	Avg. grain size (μm)	Fraction of grains with twins	Twins per grain	Twin line length density (m^{-1} /10^6)	Twin number areal density (m^{-2} /10^{10})
Cu	4.6	88 ± 12%	4.8 ± 1.0	~1.7	0.71
CuNi	4.8	75 ± 13%	3.8 ± 0.5	~1.3	0.94

Table A.3: **Twinning statistics measured by EBSD.** Twin densities and grain sizes were measured at nodes, consistent with where nanoindentation experiments were performed. Note that avg. grain size is a number average, and corroborates the grain size data from Figure 3.12.

Reference	**Material**	**d (μm)**	**d std. dev (μm)**	**H (GPa)**	**H std. dev. (GPa)**	**Notes**
Wang 2020	$Ni_{52}Cu_{48}$	0.028	0	6.85	0.20	
Emeis 2018	NiCu	0.21	0.0151	3.31	0.1	Extracted from Fig 3. Hardness converted from HV units
Bahr 2005	NiCu	50	N/A	1.45	0.16	Extracted from Fig. 5. Interpolated between reported $Ni_{60}Cu_{40}$ and $Ni_{40}Cu_{60}$ values with 50 μm grain size
Bansal 2005	Cu	0.05	N/A	2.1	N/A	Electrodeposited, no grain size statistics
Emeis 2018	Cu	0.45	0.0259	1.44	0.06	Extracted from Fig 3. Hardness converted from HV units
Chang 2007	Cu	40.1	5.03	1.04	0.06	Bulk Cu
	Cu	20.5	2.64	1.07	0.09	Bulk Cu
	Cu	14.3	2.95	1.07	0.08	Bulk Cu
	Cu	12.3	1.52	1.11	0.08	Bulk Cu
	Cu	4.53	0.532	1.29	0.11	Electroplated Cu
	Cu	1.56	0.352	1.41	0.11	Electroplated Cu
Fit results	**Cu**	H_0 = 1.08 GPa		k = 0.236 GPa $\mu^{1/2}$		
	CuNi	H_0 = 1.31 GPa		k = 0.927 GPa $\mu^{1/2}$		

Table A.4: **Nanoindentation reference data for Cu and CuNi Hall-Petch fits.** Data from references [140–142, 153, 154].

A.3.1 Correlation of dW/dT with defect morphology

Observed defect morphology (see FIB/SEM cross-sections Figure 4.2) is correlated with observed maximum rate of mass change dW/dT from TGA experiments, but not correlated with rate of maximum heat flow (see Table A.5).

Material	Maximum mass loss rate from TGA (%/°C)	Maximum heat flow rate from DSC (W/g)	Observed morphology
Cu	-0.97 @ 352 °C	-1.5 @ 308 °C	Small <5 μm pores, spherical & lamellar
CuNi	-0.94 @ 331 °C	-2.6 @ 304 °C	Small pores
Ni	-12.73 @ 304 °C	-3.87 @ 333 °C	Large lamellar pore
CuAg	-0.80 @ 346 °C	-1.15 @ 275 °C	Dense, phase segregated
Ag	-2.24 @ 166 °C	-1.23 @ 315 °C	Large >10 μm pores

Table A.5: **Comparison of TGA/DSC data with defect morphology.**

Like the dense Cu and CuNi samples, the dense CuAg has a low maximum dW/dT of -0.80 % °C during calcination. XRD analysis of the calcined CuAg shows that elemental Ag and CuO coexist (see Figure 4.7); silver nitrate decomposes to elemental silver during calcination [144] while under the same conditions copper nitrate is converted to CuO.

Material	Linear Shrinkage (%)	Calcination Mass Loss (%)
Ni	73.10	85.27
CuNi	69.03	84.15
Cu	63.04	87.32
CuAg	63.19	79.33
Ag	57.35	66.13

Table A.6: **Mass loss and shrinkage during processing of organogel lattices.** Linear shrinkage was calculated from lattice side length from the as-printed state to the reduced metal state, measured from SEM images. Mass loss was calculated from TGA from the swelled, dried state to the calcined state.

A.3.2 Comparison of EDS analysis in $Cu_{50}Ni_{50}$ at high and low accelerating voltage

a

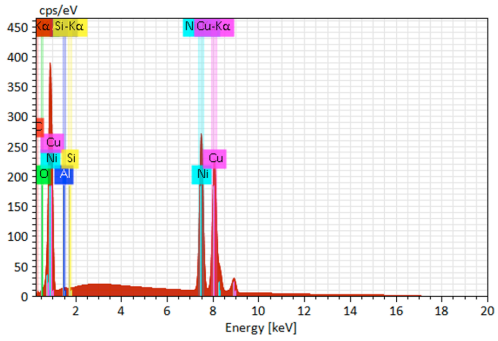

Map

Element	At. No.	Netto	Mass [%]	Mass Norm. [%]	Atom [%]	abs. error [%] (1 sigma)	rel. error [%] (1 sigma)
Copper	29	5502213	47.72	50.96	45.70	0.41	0.86
Nickel	28	6417842	42.61	45.51	44.19	0.36	0.84
Oxygen	8	209864	1.72	1.84	6.56	0.08	4.79
Aluminium	13	121969	1.31	1.40	2.96	0.06	4.59
Silicon	14	49789	0.28	0.29	0.60	0.01	4.28
Carbon	6	0	0.00	0.00	0.00	0.00	5.40
		Sum	**93.64**	**100.00**	**100.00**		

b

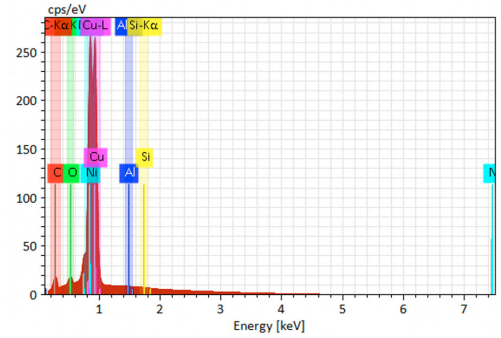

Map

Element	At. No.	Netto	Mass [%]	Mass Norm. [%]	Atom [%]	abs. error [%] (1 sigma)	rel. error [%] (1 sigma)
Copper	29	2364485	62.84	62.84	55.76	1.78	2.84
Nickel	28	2096192	34.55	34.55	33.20	0.91	2.63
Carbon	6	80455	1.69	1.69	7.95	0.06	3.80
Oxygen	8	54270	0.84	0.84	2.95	0.02	2.91
Silicon	14	2692	0.06	0.06	0.12	0.04	70.12
Aluminium	13	1130	0.01	0.01	0.03	0.00	31.86
		Sum	**100.00**	**100.00**	**100.00**		

Figure A.5: **EDS analysis for $Cu_{50}Ni_{50}$ alloy at 20 kV and 5 kV accelerating voltage. a,** EDS spectrum and element table for $Cu_{50}Ni_{50}$ with 20 kV accelerating voltage, incoming count rate of ~400 kcps. At the high accelerating voltage and count rate needed to quantify the atomic ratio of Cu and Ni, the C peak is obscured, and the EDS software cannot quantify C due to high uncertainty. **b,** EDS spectrum and element table for the same $Cu_{50}Ni_{50}$ sample, in the same location and magnification, with 5 kV accelerating voltage, incoming count rate of ~75 kcps. Note that for 5 kV accelerating voltage, Ni and Cu Kα peaks are not excited, and so Cu and Ni content must be quantified using the lower energy and overlapping Lα peaks. However, the C peak is more easily distinguished. This exemplifies the difficulty with simultaneously quantifying both light and heavy elements.

A.3.3 EDS analysis of phase separation in CuNiCoFe

1

Element	At. No.	Netto	Mass [%]	Mass Norm. [%]	Atom [%]	abs. error [%] (1 sigma)	rel. error [%] (1 sigma)
Copper	29	4495	51.85	63.64	50.13	4.17	8.03
Nickel	28	1112	10.31	12.66	10.80	0.88	8.54
Cobalt	27	1149	9.33	11.46	9.73	0.80	8.62
Iron	26	711	5.12	6.28	5.63	0.46	9.04
Carbon	6	99	4.43	5.44	22.66	0.61	13.66
Aluminium	13	55	0.40	0.49	0.90	0.11	28.88
Oxygen	8	3	0.04	0.05	0.14	0.14	386.10
Silicon	14	0	0.00	0.00	0.00	0.00	2.25
		Sum	**81.48**	**100.00**	**100.00**		

2

Element	At. No.	Netto	Mass [%]	Mass Norm. [%]	Atom [%]	abs. error [%] (1 sigma)	rel. error [%] (1 sigma)
Cobalt	27	9885	30.64	33.21	28.43	1.49	4.87
Nickel	28	7616	26.81	29.05	24.98	1.36	5.06
Iron	26	6954	16.34	17.71	16.00	0.78	4.75
Copper	29	3075	14.24	15.44	12.26	0.82	5.73
Carbon	6	239	3.80	4.11	17.29	0.38	10.03
Aluminium	13	112	0.24	0.26	0.49	0.06	24.45
Oxygen	8	28	0.12	0.13	0.41	0.09	78.71
Silicon	14	54	0.08	0.09	0.15	0.04	49.10
		Sum	**92.26**	**100.00**	**100.00**		

3

Element	At. No.	Netto	Mass [%]	Mass Norm. [%]	Atom [%]	abs. error [%] (1 sigma)	rel. error [%] (1 sigma)
Copper	29	2974	50.56	69.47	55.44	4.84	9.57
Nickel	28	637	8.47	11.64	10.06	0.87	10.32
Cobalt	27	589	6.59	9.05	7.79	0.69	10.51
Carbon	6	60	3.90	5.36	22.65	0.66	16.89
Iron	26	333	3.25	4.47	4.06	0.38	11.54
Aluminium	13	0	0.00	0.00	0.01	0.03	999.00
Oxygen	8	0	0.00	0.00	0.00	0.00	4.82
Silicon	14	0	0.00	0.00	0.00	0.00	2.25
		Sum	**72.78**	**100.00**	**100.00**		

Figure A.6: **CuNiCoFe EDS element quantification of Cu-rich and Cu-poor regions.** EDS spectra collected at an accelerating voltage of 20 kV, ICR ~ 60 kcps.